UNIVERSITÉ DU LUXEMBOURG

PhD-FSTM-2023-137
The Faculty of Science, Technology and Medicine

DISSERTATION

Defence held on 16/11/2023 in Esch-sur-Alzette

to obtain the degree of

DOCTEUR DE L'UNIVERSITÉ DU LUXEMBOURG

EN BIOLOGIE

by

Lara HAASE

Born on the 26th of April 1995 in Mulhouse, (France)

THE ROLE OF IRG1 IN ATHEROSCLEROSIS

Dissertation defence committee

Dr Johannes Meiser, dissertation supervisor
Director, Department of Cancer Research, Luxembourg Institute of Health

Dr Jan Van den Bossche
Associate professor, Amsterdam University Medical Centers

Dr Michel Mittelbronn, Chairman
Professor, Université du Luxembourg

Dr Emiel Van der Vorst
Group leader, RWTH Aachen University

Dr Dirk Brenner, Vice Chairman
Professor, Université du Luxembourg

Dissertation Defence Committee:

Dr. Johannes Meiser, dissertation supervisor
Director, Department of Cancer Research, Luxembourg Institute of Health

Assoc. Prof. Jan Van den Bossche
Associate professor, Amsterdam University Medical Centers

Dr. Emiel Van der Vorst
Group Leader, RWTH Aachen University

Prof. Michel Mittelbronn, Chair
Professor, Université du Luxembourg

Prof. Dirk Brenner, Vice Chair
Professor, Université du Luxembourg

Asst. Prof. Jochen Schneider, Expert in an advisory capacity
Assistant Professor, Université du Luxembourg

The work presented in this thesis was part of the
Nextimmune PhD training Program and was conducted at the:

Cancer Metabolism Group (CMG)
Department of Cancer Research (DoCR)
Luxembourg institute of health (LIH)

Medical Translational Research Group
Luxembourg Centre for Systems Biomedicine (LCSB)
University of Luxembourg.

In association with the
University Hospital Homburg

In collaboration with the
National Centre of Pathology
Laboratoire National de Santé (LNS)

The work presented in this thesis was funded by

The Program for Research-Intensive Doctoral Education (PRIDE) project code 11012546 from the Luxembourg National Research Fund (FNR)

Affidavit

I hereby confirm that the PhD thesis entitled “The Role of IRG1 in Atherosclerosis” has been written independently and without any other sources than cited. All necessary ethical approvals have been obtained in accordance with the EU directive 2010/63/EU of care and use of laboratory animals.

Luxembourg,30th of September 2023 Lara Haase

ACKNOWLEDGEMENTS

First, I would like to express my deepest gratitude to Dr. Johannes Meiser for his supervision, guidance, and support of the past four years. You created an immensely positive working environment shaping the CMG group towards solid and trustworthy science. Thank you for transmitting your passion for metabolism which is (still) for many a scary subject in science. I can now proudly say that I know how the TCA cycle works.

I am extremely grateful to Asst. Prof. Jochen Schneider without whom I would not have been able to start the project. Thank you for your scientific advice and guidance for all atherosclerosis related experiments. I would also like to thank my other CET committee member Assoc. Prof. Alexander Skupin for his constructive comments and feedback.
I deeply thank Assoc. Prof. Jan Van den Bossche, Dr. Emiel Van der Vorst, Prof. Dirk Brenner and Prof. Michel Mittelbronn for having accepted to evaluate my thesis. I highly appreciate your constructive feedback and value your presence at the defence.

I am immensely grateful to the Luxembourg institute of health, the Luxembourg centre for system biomedicine and the university of Luxembourg for enabling me to undergo the PhD journey. I am also thankful to the Luxembourg national research fund and the programme for research-intensive doctoral education for their funding enabling the entire work depicted in this thesis.

Special thanks to Iris Adrian who nicely took care of all the mice during the four years. Thank you for the little teatime before the long days of *in vivo* work. I am also grateful to Dr. Etienne Moussay for his RNA seq analysis. Many thanks to Dr. Anne Largeot for her help with the OPP assay. A big thank you to Jean-Jacques Gerardy for his assistance on cutting and staining aortic arch slices. I would also like to thank the members of the metabolomics platform of the LCSB Dr. Christian Jaeger, Xiangyi Dong and Florianne Gavotto for their efficient work acquiring all the GC-MS data. A big shoutout to the members of the metabolomics platform of the LIH Dr. Antoine Lesur and Francois Bernardin for measuring the multiple last-minute batches shaping a great part of my thesis.
I also wish to thank the members of the national cytometry platform Maira Konstantinou, Mario Gomez and Fanny Hedin for their precious help with the Quanteon, advice on data analysis as

well as their tips on panel design. Thank you also for the pleasant chats on scientific and less scientific topics.
I am extremely grateful to the entire CMG team: the dream team. Thank you all for the 4 years of supportive uplifting atmosphere and positive working environment promoting mutual aid. Nicole, thank you for the extremely valuable scientific feedback and help answering all my questions. Also thank you for all the mouse Homburg days together with Laura, spending several hours on tissue processing for this project. Laura, thank you for the help during the mouse Homburg days and more generally for the entire lab management. Thank you for enduring all my last-minute very urgent orders and thank you for all the outside of the lab adventures. Catherine, I really enjoyed your cheerful motivating personality as well as all our lab conversations about the PhD life and the spontaneous after work cake days. Mohaned, thank you for teaching me everything you knew about BMDMs when I started. Also thank you for all your advice on metabolic data analysis (metabolite master). Björn, thank you for all the various scientific discussion and for all the very surprising topics you sometimes bring up. Kim thank you for all your support to keep me motivated especially at the end of my PhD. Oleg, thank you for all the itaconate, succinate epigenetic related discussions giving me new insights on the project. Also thank you for teaching me a bit of Ukrainian. To our newest CMG member Christina, thank you for your support in the final moments of my PhD.

A big thank you to my former office colleagues Carina with whom I had great discussions on the very late lab work-evenings. Also, Yahaya, Mohamad, Yolanda and Hugo who made the beginning of the PhD easier. I am also very grateful to all my colleagues at DoCR, Andrea, Frida, Alice, Alex, Redouane and to all the others I could not cite here, thank you for shaping the nice working atmosphere of the department.

Finally, I wish to thank my friends and family who supported me throughout this journey. To my parents for their love and support of the past 28 years. Thank you for your reassuring words every time I doubted myself. To my friends with whom I shared endless game nights. Thank you for all the cheerful moments. At last but not least I would like to thank Dr. Axel Chemla who followed and supported me through each step of the PhD. Thank you for the motivational boosts and all the adventures we went on, exploring the other side of the world.

TABLE OF CONTENT

ABBREVIATIONS

APC	Antigen-presenting cell
ApoB	Apolipoprotein B
ApoE	Apolipoprotein E
ASC	Apoptosis-associated speck-like protein
ATP	Adenosine triphosphate
BIR	Baculoviral inhibitory repeat
BMDM	Bone marrow derived macrophage
CARD	Caspase recruitment domain
CCL	C-C motif chemokine ligand
CCR	C-C motif chemokine receptor
CD	Cluster of differentiation
CETP	Cholesterol ester transfer protein
CHD	Coronary heart disease
cIAP	Cellular inhibitor of apoptosis
CIITA	MHC-II transactivator
CLR	C-type lectin receptor
CTP	Cytosine triphosphate
CVD	Cardiovascular diseases
CXCL	C-X-C motif chemokine ligand
CyTOF	Cytometry by time-of-flight
DAMPs	Danger associated molecular pattern
DC	Dendritic cell
DEG	Differential expression of genes
dsRNA	Double stranded ribonucleic acid
DTT	DL-Dithiothreitol
ECAR	Extracellular acidification rate
EDTA	Ethylenediaminetetraacetic acid
FBS	Foetal bovine serum
FH	Familial hypercholesterolemia
Glc	Glucose
Gln	Glutamine
GSEA	Gene set enrichment analysis
GTP	Guanosine triphosphate
HDL	High density lipoprotein
HFD	High fat diet
ICAM-1	Intercellular adhesion molecule 1
IDH	Isocitrate dehydrogenase
IDL	Intermediate density lipoprotein
IFNγ	Interferon gamma
IFNGR	Interferon gamma receptor
Ig	Immunoglobulin

IKKε	I kappa B kinase ε
IL	Interleukin
IL-1R	Interleukin-1 receptor
IL-6R	Interleukin-6 receptor
iNOS	inducible nitric oxide synthase
IRAK	Interleukin-1 receptor associated kinase
Jak1	Janus tyrosine kinase
JAM-A	Junctional adhesion molecule A
KO	Knock-out
LAMP	Lysosome-associated membrane protein
LDL	Low density lipoprotein
LDLr	Low density lipoprotein receptor
LFA1	Lymphocyte function-associated antigen 1
LN	Lymph node
LOX-1	Lectin-type oxidized LDL receptor 1
LPS	Lipopolysaccharide
LRP1	LDL receptor related protein 1
LRR	Leucine rich repeat
LTA	Lipoteichoic acid
Mac1	Macrophage antigen 1
MARCO	Macrophage receptor with collagenous structure
M-CSF	Macrophage colony-stimulation factor
MHC-I	Major histocompatibility complex class I
MHC-II	Major histocompatibility complex class-II
miRNA	Micro ribonucleic acid
MR	Mannose receptor
NAIP	Neuronal apoptosis inhibitory protein
NES	Normalized Enrichment Score
NF-κB	Nuclear factor-kappa B
NK	Natural killer
NLR	NOD-like receptor
NO	Nitric oxide
NOD	Nucleotide-binding-oligomerization domain
OCR	Oxygen consumption rate
OPP	O-propargyl-puromycin
OXPHOS	Oxidative phosphorylation
PAMPs	Pathogen associated molecular pattern
PBS	Phosphate-buffered saline
PCR	Polymerase chain reaction
PECAM1	Platelet/endothelial-cell adhesion molecule 1
PFA	Paraformaldehyde
PRR	Pattern recognition receptor
PSGL	P-selectin glycoprotein ligand 1
ROS	Reactive oxygen species

S1P	Sphingosine-1-phosphate
SD	Standart deviation
SDH	Succinate dehydrogenase
SR	Scavenger receptor
ssRNA	Single stranded ribonucleic acid
Stat	Signal transducer and activator of transcription
TAK1	TANK binding kinase 1
TAM	Tumour associated macrophage
TANK	TRAF family member-associated NF- κB activator
TBS	Tris-buffered saline
TCA	Tricarboxylic acid
TCR	T-cell receptor
Th	T-helper
TIR	Toll interleukin 1 receptor
TLR	Toll like receptor
Treg	Regulatory T-cell
UTP	Uridine triphosphate
VCAM1	Vascular cell adhesion protein 1
VLA4	Very late antigen 4
VLDL	Very low-density lipoprotein
WT	Wild-type
XIAP	X-linked inhibitor of apoptosis protein

The dimensions of this thesis are consistent with the International System of Units (SI)

LIST OF FIGURES

LIST OF TABLES

1. ABSTRACT

Atherosclerosis is a primary contributing factor to heart attacks and strokes which are the leading cause of death on a global scale. This disease is characterised by the accumulation of lipids and macrophages in the artery walls. Over the recent years, metabolism in macrophages gained increasing attention when it has been discovered that metabolic adaptation is central to cellular function. The immune responsive gene 1 (*IRG1*) is expressed in macrophages after a pro-inflammatory stimulus. The protein catalyses the synthesis of itaconate in the cell which influences certain metabolic pathways, reduces the production of reactive oxygen species and, promotes anti-inflammatory mechanism through activation of NRF2 and inhibition of the NLRP3 inflammasome. This thesis aims to understand the role of itaconate in inflammatory vascular diseases.

To study this question *Irg1*$^{-/-}$ mice were crossed with *Apoe*$^{-/-}$ or *Ldlr*$^{-/-}$ mice, two widely used atherosclerosis models. They were fed during 12 weeks with a high fat diet. Plaques are quantified in the aorta as well as the aortic root. Moreover, blood and spleen are further processed to characterize immune cells in presence or absence of *Irg1*. Bone marrow derived macrophages (BMDMs) are differentiated from the bone marrow of IRG1 deficient mice and are metabolically profiled to further understand the mechanism induced by itaconate in macrophages.

The plaque size in the aorta was reduced in female ApoE IRG1 deficient mice compared to their IRG1 wild-type (WT) littermates. However, the plaque size in the aortic valve was similar. Interestingly, LDLr IRG1 deficient male mice showed an increased body weight gain as well as an increased plasma cholesterol concentration. The immune cell profiling demonstrated that IRG1 deficiency influences T cells, especially in female mice in both atherosclerotic models. The BMDM study highlights metabolic changes induced by itaconate which are exacerbated if the cells are stimulated with lipopolysaccharide and interferon-gamma, both relevant stimuli in atherosclerosis.

Taken together this study supports the involvement of IRG1 in atherosclerosis and highlights the IRG1-induced metabolic rewiring in pro-inflammatory macrophages. Gaining a better understanding on the role of *Irg1* in context of atherosclerosis may help for developing novel therapeutic strategies aiming to reduce inflammation and plaque size thereby reducing the incidence of cardiovascular events.

2. INTRODUCTION

2.1. Atherosclerosis

The leading cause of death on a global scale are cardiovascular diseases (CVD). According to the world health organization, 17.9 million people died from CVDs in 2019 (32% of total deaths) and amongst all CVD deaths, 85% were due to ischaemic heart disease and stroke (Global Health Estimates, 2020). Atherosclerosis is a major underlying cause for CVDs. The disease consists in an abnormal accumulation of lipids and immune cells in the vessel wall forming plaques leading in later stages to a calcification of the intimal layer. The lumen of the affected artery narrows over time and instable plaque rupture can lead to a complete occlusion of the vessel leading to a cardiovascular event or stroke.

2.1.1. The Pathogenesis of atherosclerosis

Over the years several hypotheses have been established to understand atherogenesis, however the main cause of atherosclerosis onset is not yet clearly established. This section aims to give an overview of all potential atherogenesis factors.

2.1.1.1. The lipid hypothesis:

Around 1850 Von Rokitansky described an abnormal but frequent form of disease consisting in an “excessive formation and deposition of the lining membrane of the artery” (Rokitansky et al., 1855). His observations led him to believe that the thrombus formation is the first event of atherosclerosis. According to his hypothesis, the thrombus later degrades into lipids and creates the lesion (Stehbens, 1992). Only years after in 1913, Anichkov demonstrated that cholesterol alone could cause atheromatous changes in the vessel wall in rabbits fed with cholesterol (Anichkov and Chalatov, 1983; Konstantinov et al., 2006). In the early years following his publication, many scientist believed his work to be specific to the rabbit as they could not reproduce the finding in dogs or rats and could therefore be irrelevant to humans (Steinberg, 2013). However, several decades later the Framingham study showed a link between elevated cholesterol levels in the blood and increased coronary heart disease (CHD) risk in humans (Kannel et al., 1961). The same long term study also gave evidence that high density lipoproteins (HDL) are protective against CHD while low density lipoproteins (LDL) increase the risk of developing CHD (Castelli et al., 1992; Gordon et al., 1977). The lipid infiltration hypothesis was then born stating that elevated plasma cholesterol has a causal role in atherosclerosis development. The atherosclerosis research was then mainly focused on lipid metabolism.

2.1.1.2. The oxidative stress hypothesis

A genetic driven disease called familial hypercholesterolemia (FH), which is characterized by elevated LDL-cholesterol concentration in the plasma, leads to early occurring heart attacks. By studying fibroblast from persons having FH, Goldstein and Brown discovered LDL receptors (LDLr) (Goldstein and Brown, 2009). Indeed, FH patients usually have a loss of function mutation in the gene coding for LDLr. A paradox then emerged as those patients also have foam cells in their arteries despite having dysfunctional LDLr indicating another potential mechanism explaining foam cell creation (Brown and Goldstein, 1983). They carried on their research on mouse peritoneal macrophages and observed that macrophages could not efficiently phagocyte LDL compared to a modified version of LDL: acetyl-LDL thereby discovering another receptor type that they called acetylated LDL receptor (Goldstein et al., 1979). However, acetyl-LDL does not exist *in vivo* and the search for modified LDL continued. In 1981, Henriksen et al. made a significant discovery, demonstrating that endothelial cells possess the ability to modify the LDL molecule metabolically. This modification leads to the production of a specific form of LDL that is more rapidly degraded by macrophages and is recognized by the macrophage receptor for acetylated LDL (Henriksen et al., 1981). Further studies showed that endothelial cells can cause oxidative modifications to LDL now called oxLDL (Steinberg et al., 1989; Steinbrecher et al., 1984) The oxidation modification theory was born stipulating that oxLDL is an important factor in atherogenesis. Since then, oxLDL is widely studied in context of atherosclerosis (Steinberg, 2009).

LDL can undergo oxidative modification in the subendothelial space of arteries due to exposure to cell-derived oxidants, including transition metal ions and various catalysts. Both enzymatic and non-enzymatic mechanisms are proposed for the oxidation of LDL within the artery wall. The process of oxidative modification can occur when LDL particles interact with various cell types like macrophages, endothelial cells, and smooth muscle cells (Yoshida and Kisugi, 2010).

2.1.1.3. The endothelial cell dysfunction hypothesis

The vascular endothelium is a single layer of cells lining the entire circulatory system. It was once considered a passive barrier, but it is now recognized as an essential organ for maintaining vascular health and playing a key role in the development and complications of vascular diseases. The endothelium acts as a selectively permeable barrier and interacts with circulating blood components, and cells in the surrounding tissues (Cahill and Redmond, 2016). Disrupted communication between endothelial cells and adjacent cell types like vascular smooth muscle cells is linked to vascular dysfunction and CVDs including atherosclerosis and hypertension (Méndez-Barbero et al., 2021). Endothelial cells

are subjected to alterations in the vessel lumen, including shear stress, mechanical injury, and exposure to various chemicals like signalling molecules, lipoproteins etc. In response, these cells release various cytokines, chemokines, and growth factors, leading to an endothelial dysfunction phenotype (Sun et al., 2019). This phenotype is marked by an imbalance between vasodilation, vasoconstriction, increased levels of reactive oxygen species (ROS), proinflammatory factors, and reduced availability of nitric oxide (NO) (Botts et al., 2021).

2.1.1.4. The inflammation hypothesis

Since the end of the 20th century more studies linked inflammation to atherosclerosis which is now considered as an inflammatory disease. While the link between atherosclerosis and inflammation was made around 1850 by Virchow, it was put aside for the lipid research. Virchow viewed atherosclerosis as an active tissue reaction process as opposed to a simple thrombus encrustation or fatty material build-up (Libby, 2012). In 1986 macrophages as well as T cells could be observed in human plaques (Jonasson et al., 1986). Animal models and human studies show that inflammation occurs alongside the early accumulation of lipids in artery walls (Mehu et al., 2022). In animal models, the ingestion of high fat diet rapidly induced the expression of adhesion molecules like the vascular cell adhesion molecule-1 (VCAM-1) in endothelial cells of the arteries (Li et al., 1993; Nakashima et al., 1998). In humans VCAM-1 is expressed in certain plaques but not in healthy arteries (Davies et al., 1993). These adhesion molecules then attract white blood cells, particularly monocytes and T cells, to sites of atherosclerotic lesion formation (Galkina and Ley, 2007).

It is interesting to note that disturbed blood flow at arterial branch points is associated with dysfunctional endothelium, leading to reduced NO secretion. This reduction in NO selectively reduces the expression of adhesion molecules and proinflammatory cytokines in endothelial cells (De Caterina et al., 1995). Once adhered to the endothelium, leukocytes migrate into the intima and contribute to a local inflammatory response. Macrophages become foam cells by ingesting lipids, and T cells secrete inflammatory cytokines (Libby et al., 2002). This inflammatory process leads to the progression of atherosclerotic lesions. In later stages inflammatory mechanisms also contribute to acute thrombotic complications of atherosclerosis, as macrophages produce enzymes that weaken the protective fibrous cap of plaques (Libby, 2002). Furthermore, Interferon gamma (IFNγ) produced by T cells in the plaque can inhibit the collagen produced by SMCs (Amento et al., 1991).

2.1.1.5. The infection hypothesis

Closely linked to the endothelial dysfunction and inflammation hypothesis the infection hypothesis suggests that infectious agents may also contribute to atherosclerosis. This can happen either through direct infection of vascular cells or indirectly by inducing cytokines

and acute phase reactant proteins (Campbell and Rosenfeld, 2015). Several bacterial and viral pathogens have been linked to atherosclerosis (Jung and Lee, 2022; Shah, 2001). For example the infection of Chlamydia pneumoniae accelerated plaque development in mice and induced endothelial dysfunction (Blessing et al., 2001; Liuba et al., 2000) In human plaques Chlamydia pneumoniae could also be detected (Kuo et al., 1993). The infectious hypothesis is also closely linked to the response to injury hypothesis which proposes that endothelial cell activation is caused by an injury which itself could have several causes like infections, chronic hyperlipidaemia, or shear stress (Ross et al., 1977).

2.1.1.6. Atherosclerosis and miRNAs

In the past years the research on micro ribonucleic acids (miRNAs) increased and revealed important links between miRNAs and atherosclerosis. MiRNAs are a class of small non-coding RNA molecules that modulate gene expression post-transcriptionally by degrading and repressing the translation of target messenger RNAs. They can regulate several cell factors and can also be transmitted from cell to cell. In endothelial cells, miRNA-126 expression is linked to the inhibition of VCAM-1 therefore playing a decisive role in leukocyte recruitment (Harris et al., 2008). Due to their stable presence in peripheral blood and convenient detection in fluids, such as serum, plasma, saliva, and urine, through conventional non-invasive methods, microRNAs could serve as biomarkers for diagnosing and monitoring CVD (Hosen et al., 2020). Interestingly low miRNA-126 levels have been associated to higher plaque complexity and therefore an increased risk for cardiac events (Theofilis et al., 2023). Several other miRNA are studied regarding their expression in endothelial cells, macrophages, dendritic cells, smooth muscle cells in regards of their capacity to regulate inflammation, angiogenesis, apoptosis, migration, vascular integrity and permeability (Hosen et al., 2020).

2.1.1.7. Summary

All the factors mentioned above have been shown to contribute to atherogenesis in several ways (Figure 1). They are important target options in therapies aiming to reduce plaque formation. However, a lack of understanding of the intricate interplay between these factors and their dynamic interactions within the atherosclerotic process hinders the development of highly effective and precise therapeutic interventions. Further research is needed to elucidate these complex mechanisms, ultimately leading to more tailored and efficient strategies for preventing and treating atherosclerosis.

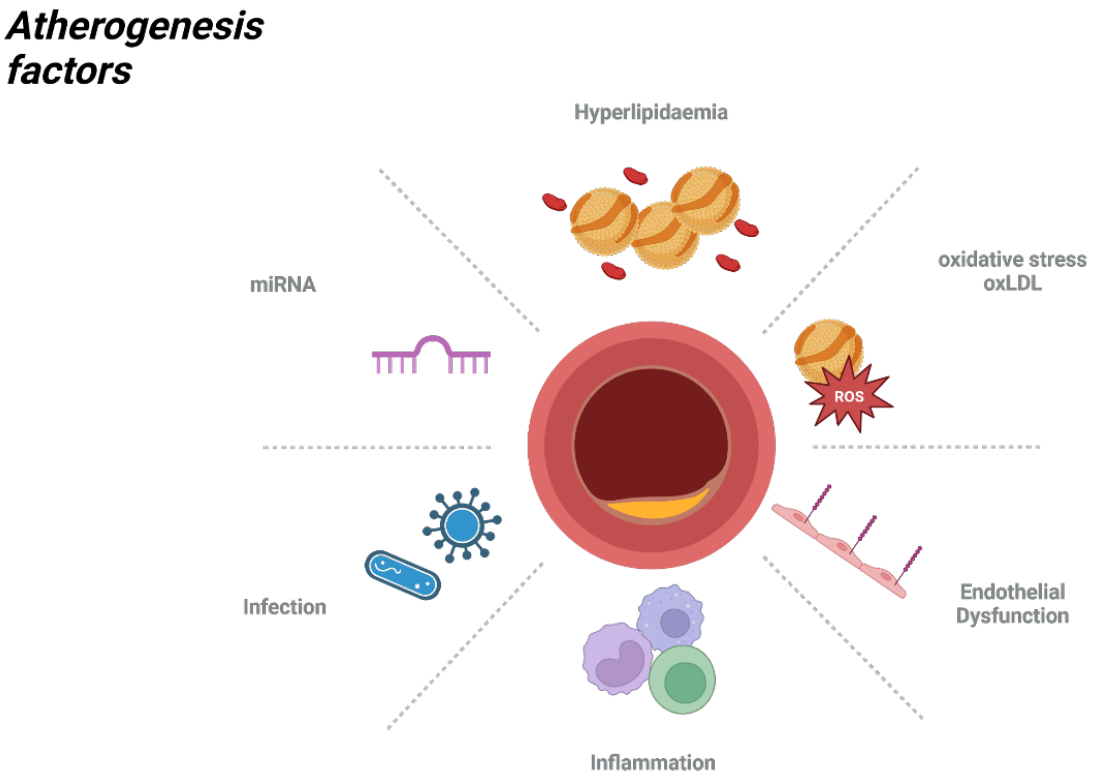

Figure 1. Atherogenesis factors

Illustration showing all different factors contributing to atherosclerosis onset. This includes hyperlipidaemia, oxidative stress, endothelial dysfunction, inflammation, infection, and certain miRNAs. Made with Biorender.

2.1.2. Plaque stages of atherosclerosis

In the 90s, the American Heart Association's Committee on Vascular Lesions published three Scientific Statements that encompassed a substantial amount of knowledge covering information on the composition and structure of human atherosclerotic lesions, as well as the arterial locations where they commonly form. The lesion types were classified in the believed chronologic order of plaque formation.

Early lesions encompass type I and type II lesions. The type I lesion is the earliest described change microscopically observed, composed of isolated macrophages and foam cells. The type II lesion is commonly referred as fatty streak and is composed by several layers of foam cells. Interestingly early lesions are found in children and young adults showing that the disease can start early in life (Hong, 2010). Compared to type II lesions, type III lesions contain isolated extracellular lipid pools. This lesion type is considered to be the intermediate between early lesions and advanced plaques (Stary et al., 1994). The advanced plaques are numbered from type IV to VIII and depending on their size can lead to vascular obstruction (Stary, 2000). Type IV lesions, also referred to as atheroma, are the first advanced lesions in this classification due to the significant intimal disorganization

caused by the lipid core. Type V lesions, known as fibroatheroma, retain a lipid core and exhibit a prominent presence of fibrous connective tissue. Without lipid core but with fibrous connective tissue lesions are associated to type VIII. Lesions where calcification has occurred are associated to type VII lesions. Atherosclerosis-related morbidity and mortality primarily stem from type IV and type V lesions, characterized by disruptions of the lesion surface, hematoma or haemorrhage, and thrombotic deposits. Lesions with these additional features are categorized as type VI or complicated lesions (Stary et al., 1995).

It is important to note that plaque types can evolve in several directions. Early plaque types can regress to become normal tissue while regression of type IV and V lesions can lead to type VII and VIII lesion formation. Additionally, several type VI episodes can occur and accelerate the occlusion process (Stary, 2000).

2.1.3. Animal models of atherosclerosis

Over the years several animal models have been used to study atherosclerosis. Each model presents its benefits and limitations. Amongst large animals, rabbits, pigs and non-human primates are common models. Pigs have a close phylogenetic relation to humans and similar anatomy, with comparable heart and vasculature size. Additionally, being omnivores like humans, pigs exhibit a vascular response to increased dietary fat content that resembles human physiology (Hamamdzic and Wilensky, 2013). Non-human primates have similarities to humans in lipoprotein metabolism, HDL subclasses, and expression of cholesterol ester transfer protein (CETP). Some species do develop complex coronary lesions like humans (Getz and Reardon, 2012). However, the use of genetic and immunological tools is often limited in large animals.

Currently the mouse is the most widely used animal model of atherosclerosis due to the possibility of genetic manipulation, relatively low costs, and ease of breeding. However, mice have a different lipid profile from humans, with HDL being the primary carrier of cholesterol due to the lack of CETP (Hogarth et al., 2003). They do not naturally develop atherosclerosis unless exposed to atherogenic diets for extended periods which only gives rise to fatty streaks (Gisterå et al., 2022). Therefore genetic manipulation or specific vectors injections inducing lipid metabolism change are mandatory (Emini Veseli et al., 2017; Goettsch et al., 2016).

In this thesis the Apolipoprotein E (ApoE) knock- out (KO) as well as the LDLr KO mouse models are used as atherosclerosis models.

2.1.3.1. The ApoE model

ApoE is synthesized in the liver and brain and is associated with various lipoproteins, including very low-density lipoprotein (VLDL), intermediate density lipoproteins (IDL), chylomicron remnants, and certain subclasses of HDL. Its main role is to regulate the clearance of these lipoproteins from the plasma by acting as a ligand for specific cell-surface receptors, such as the LDLr family members (Huang and Mahley, 2014). It also has local effects on cholesterol homeostasis and inflammatory reactions in atherosclerotic vessels. Additionally, it may play a role in dietary absorption and biliary excretion of cholesterol (Meir and Leitersdorf, 2004). The ApoE KO mouse line was generated in 1992 simultaneously in two different laboratories by homologous recombination (Piedrahita et al., 1992; Plump et al., 1992). The mouse line which is nowadays commercialized by the Jackson Laboratories comes from the Maeda Lab. They generated the model by replacing a portion of exon 3 and part of intron 3 of the ApoE gene with a neomycin resistance cassette (Piedrahita et al., 1992). These mice have a delayed clearance of lipoproteins and have higher cholesterol levels around 400mg/dL due to an accumulation of chylomicron and VLDL remnants (Breslow, 1996). They do develop plaques on chow diet: after 10 weeks fatty streaks appear and after 20 weeks fibrous plaques start to appear. When fed a Western type diet their cholesterol levels increase above 1500mg/dL and the plaque formation process is accelerated.

2.1.3.2. The LDLr model

The LDLr plays an important role in the LDL plasma clearance. The LDLr recognizes the apolipoprotein B (ApoB) on the surface of LDL particles which initiates the endocytosis process. LDL is then rapidly degraded in the lysosome and releases its components including cholesterol which can be metabolized by the cell (Go and Mani, 2012; Goldstein and Brown, 2009). To mimic the FH condition in humans, a LDLr KO mouse was generated in 1993 by insertion of a neomycin cassette in the exon 4 of the *Ldlr* gene (Ishibashi et al., 1993). On chow diet the total plasma cholesterol levels reach 200-250 mg/dL while on a cholesterol rich diet they reach levels over 1000mg/dL (Ishibashi et al., 1994). According to the national lipid association, humans with homozygous FH have total cholesterol levels between 650mg/dL and 1000mg/dL indicating that the LDLr KO mouse model is comparable to human FH when fed a high cholesterol diet. On chow diet these mice do not develop atherosclerosis. However, when fed an atherogenic diet, plaques develop in the proximal aorta and in later stage in the distal aorta.

2.2. The Immune system

2.2.1. Overview

The immune system is a complex network of specialized cells, tissues, and organs that work together to defend the body against several dangers like infections, foreign substances, and abnormal cells. It plays a crucial role in recognizing and destroying pathogens, such as bacteria, viruses, and parasites, as well as identifying and eliminating damaged or cancerous cells.

The immune system can artificially be divided into two major categories: the innate and the adaptive immune system (Murphy and Weaver, 2017).

1. The innate immune system:

It is present in all metazoan animals. It is characterized by several defence mechanism that are genetically inherited which are already functional at birth. This response is quick, available in all tissues of the organism and constitute a first line of defence. However, its mechanism cannot adapt to specific pathogens over time.

2. The adaptive immune system:

It only exists in vertebrates. It is based on the generation of an almost infinite possibilities of receptors based on the random recombination of a certain available gene pool. When the organism is confronted to a pathogen, the adaptive immunity must select the specific receptor against the pathogen to build defences which are specifically raised against this pathogen. The effector mechanisms are acquired over time and adapt to the pathogens encountered by the organism. Moreover, after encountering a pathogen a memory starts to build up in case the organism encounters the pathogen several times.

Cells from the immune system commonly called leukocytes, are generated from stem cells during haematopoiesis. Leukocytes are often classified from which lineage they are derived from. The common myeloid progenitor generates all cells from the myeloid lineage including granulocytes, mast cells, macrophages, and dendritic cells (DC). The common lymphoid precursor generates cells from the lymphoid lineage such as B cells, T cells and Natural killer (NK) cells.

In atherosclerosis cells from the innate and adaptive immune system play a crucial role.

2.2.2. Macrophages

Macrophages were already observed by Elie Metchnikoff in 1882 after inserting a splinter in a transparent starfish larva. He described them as amoeboid cells engulfing foreign

objects, calling them phagocytes: eating cells (Tauber, 2003). They are present in various tissues and can originate from embryonic development or differentiate from circulating monocytes. They are associated to the innate immune response but also serve an essential role in the adaptive immune response. Their functions include phagocyting and eliminating invading microorganisms, pathogens and infected cells, inducing inflammation by producing inflammatory mediators as well as presenting antigens to cells from the adaptive immunity. (Murphy and Weaver, 2017).

2.2.2.1. Danger recognition

Being part of the innate immune response macrophages possess a panel of receptors recognizing a broad range of danger associated patterns. These receptors are called pattern recognition receptors (PRRs), and they recognize specific structures called danger associated molecular patterns (DAMPs) released by damaged or dying cells or pathogen associated molecular patterns (PAMPs) found in various microorganisms. The PAMPs are conserved throughout evolution, making them effective targets for immune recognition (Li and Wu, 2021; Murphy and Weaver, 2017).

2.2.2.1.1. Scavenger Receptors

Scavenger receptors (SRs) are part of a large family of cell-surface receptors. The range of ligands they recognize is extremely diverse and includes unmodified endogenous proteins, lipoproteins, modified lipoproteins (such as oxLDL) as well as several conserved microbial structures, such as bacterial lipopolysaccharide (LPS) and lipoteichoic acid (LTA). They are divided in several classes from A to L based on their structure and numbered within each class based on the order in which the molecules were identified (Alquraini and El Khoury, 2020).

Class A:

The first type of SR was discovered by Goldstein and Brown in 1979 named as acetylated LDL receptor (see section 2.1.1.2). Nowadays this receptor is called SR-A1. It exhibits broad ligand specificity, as it can bind to various molecules such as heat shock proteins, amyloid-β, surface molecules of bacteria, as well as acetylated LDL and oxLDL. Another class A SR widely expressed in macrophages is the macrophage receptor with collagenous structure (MARCO, also called SCARA2 or SR-A6). MARCO binds soluble LPS, intact Gram-positive and -negative bacteria as well as oxLDL. Binding to SR-A receptors will result in the phagocytosis of the ligand (Areschoug and Gordon, 2009; Plüddemann et al., 2007).

Class B:

Class B SRs are characterized by two transmembrane domains with a short intracellular domain and a large extracellular loop with a hydrophobic sequence. Two receptors are composing this class. SR-B1 (also SCARB1, or CD36L1) is a selective lipid transporter and the first identified surface receptor for anionic phospholipids and HDL. SR-B1 might play a protective role against atherosclerosis, as its removal in ApoE KO mice induced spontaneous myocardial infarctions (Braun et al., 2002). However, an SR-B1 knock-down in another mouse model of atherosclerosis expressing CETP and a modified ApoE (ApoE*3-Leiden.CETP) showed reduced atherosclerosis (Zhou et al., 2021). SR-B2 (known as SCARB3, or CD36) also binds to HDL but has a more significant role in binding oxLDL. It is involved in cell-to-cell interactions, angiogenesis, and directly contributes to the formation of foam cells (Alquraini and El Khoury, 2020).

Class D:

The class D comprises one type I transmembrane glycoprotein containing lysosome-associated membrane protein (LAMP) and mucin-like domains. Like all previous SRs, SR-D1 (also called CD68 or SCARD1) can bind oxLDL. Aside from recognizing modified LDL it can also bind to phosphatidylserine, and apoptotic cells. In an inflammatory context this receptor can be highly upregulated. However, the extent of SR-D1's contribution to oxLDL clearance in comparison to SR-B2 remains uncertain (Chistiakov et al., 2017).

Class E:

Class E scavenger receptors are part of the C-type lectin receptor (CLR) family. They form a large superfamily of proteins with a common carbohydrate recognition domain. Among these receptors, the mannose receptor (MR, also known as CD206 or SR-E3) recognizes branched sugars with terminal mannose, fucose or *N*-acetyl-glucosamine and facilitates the clearance of various microorganisms and microbial products (Weis et al., 1998). The lectin-type oxidized LDL receptor 1 (LOX-1, also called OLR1 or SR-E1), also belongs to the CLR family as well as to the SR family. It recognizes oxLDL and participates to the formation of foam cells in atherosclerosis (Tian et al., 2019).

Another important CLR is Dectin-1 (SR-E2), which recognizes β-1,3-linked glucans from fungi, bacteria, and plants. While most CLRs act as endocytosis or phagocytosis PRR, Dectin-1 also functions as a signalling PRR, regulating the expression of pro-inflammatory cytokines.

Class F to L:

Each class comprises 1 to 3 receptors. Some receptors of these classes are linked to atherosclerosis. Indeed, SR-F1 (SCARF1), SR-G1 (CXCL16) have been shown to bind oxLDL while SR-L1 (LDL receptor related protein 1 LRP1 or CD91) plays an important role in plasma cholesterol clearance. Interestingly SR-J1 (RAGE) a member of the immunoglobulin (Ig) superfamily, recognizes endogenous molecules released during chronic inflammation or infection and plays a role in the pathogenesis of atherosclerosis.
Other receptors like SR-F2 (MEGF10), SR-H1 (FEEL-1) also bind to apoptotic cells to promote their clearance while SR-I1 (CD163) binds haptoglobin-haemoglobin complexes and bacteria while triggering intracellular signalling and the release of pro-inflammatory cytokines. Lastly, SR-K1 (CD44) serves as a receptor for hyaluronan, facilitating the clearance of its extracellular matrix ligands through endocytosis (Alquraini and El Khoury, 2020).

2.2.2.1.2. Toll-like receptors

The Toll gene was initially discovered by Christiane Nüsslein-Volhard as playing an important role in the development of the fruit fly *Drosophila melanogaster* (Anderson et al., 1985). In 1996 Jules Hoffmann discovered that Toll signalling induces host-defence mechanism in the adult fly (Lemaitre et al., 1996). Homologs of this receptor were discovered in other animals including humans and were therefore called Toll like receptors (TLRs). In humans 10 TLRs were discovered and 12 in the mouse. TLRs are transmembrane PRRs that recognize characteristic molecules of Gram-negative, Gram-positive bacteria, viruses, and fungi. Some TLRs are present on the surface of the cell while others are located intracellularly in the membrane of endosomes. They therefore can detect extracellular PAMPs as wells as components that were internalized by phagocytosis, receptor mediated endocytosis or macropinocytosis. Their intracellular region is composed of a toll-interleukin-1 receptor (TIR) domain which is important for further signalling pathway activation. Their extracellular region is composed of several leucine rich repeats (LRR) creating a horseshoe shape which can recognize and bind ligands on both surfaces. In mammals, activation of TLRs generally leads to TLR homodimer or heterodimer formation which leads to transcription factor activation and cytokine production (Murphy and Weaver, 2017).

TLR-1, TLR-2 and TLR-6 are located on the cell surface. They are activated by diacyl and triacyl lipoproteins (Gram-negative bacteria), LTA (Gram-positive bacteria), Cells wall β-glucans (bacteria and fungi) and, Zymosan (fungi). Once activated they either form TLR-2 and TLR-1 or TLR-2 and TLR-6 heterodimers. Interestingly TLR-2 can cooperate with

scavenger receptors such as CD36 and Dectin-1 in the recognition of PAMPs (El-Zayat et al., 2019; Murphy and Weaver, 2017).

Another TLR cell surface receptor is TLR-4. It plays a crucial role in detecting and responding to bacterial infections. It recognizes LPS found in Gram-negative bacteria through a partly direct and partly indirect mechanism. TLR-4 uses an accessory protein, MD-2, to recognize LPS. When the TLR4-MD-2 complex encounters LPS, five lipid chain of LPS attach to MD-2 while remains free. This free chain binds to TRL-4 which induces TLR-4 dimerization and activates intracellular signalling pathways. Besides MD-2, CD14 can also be involved in TLR-4 activation by LPS (Molteni et al., 2016; Murphy and Weaver, 2017).

TLR-3, TLR-7, TLR-8 and TLR-9. are endosomal nucleotide sensors involved in viral recognition. TLR-3 detects double-stranded RNA (dsRNA) from various viruses. TLR-7 and TLR-8 are activated by single-stranded RNA (ssRNA) found in certain virus genomes. Lastly TLR-9, recognizing unmethylated CpG dinucleotides, plays a role in detecting bacterial and viral genomes, as they contain unmethylated CpG dinucleotides, unlike mammalian genomes (Kumar et al., 2009; Murphy and Weaver, 2017).

2.2.2.1.3. NOD-like receptors

Nucleotide-binding-oligomerization domain (NOD)-like receptors (NLRs) are cytoplasmic PRRs that sense intracellular bacterial invasion as well as certain cytokines like Interferon gamma (IFNγ). After activation some NLRs undergo conformational changes leading to the formation of multi-protein complexes called inflammasomes (Motta et al., 2015).

They all have a central NOD, a C-terminal LRR domain (except NLRP10) and a variable N terminal domain. Like the TLRs, the LRR domain binds the ligand while the N terminal domain performs effector functions. The NLRs are classified in four subfamilies based on their N terminal domain (Ting et al., 2008). The N-terminal of the NLRA family is composed of an acidic transactivation domain and the NLRB family has baculoviral inhibitory repeat (BIR)-like domains. Both families consist of one member: the major histocompatibility complex (MHC)-II transactivator (CIITA) and the neuronal apoptosis inhibitory protein (NAIP) respectively. CIITA acts as a regulator of MHC-II while NAIP is a flagellin sensor, apoptosis inhibitor, which plays a role in the inflammasome assembly (Kim et al., 2016).

The N terminal domain of the NLRC family contains a caspase recruitment domain (CARD). This subfamily consists of 6 members NLRC1 (NOD1), NLRC2 (NOD2), NLRC3, NLRC4, NLRC5, and NLRX1. NOD1 and NOD2 were the first discovered NLRs. They can detect peptidoglycan fragments and muramyl dipeptide enabling the detection of both Gram negative and positive bacteria. They mediate the activation of the nuclear factor-kappa B (NF-κB) which mediates cytokine production (Caruso et al., 2014).

The NLRP family contains a pyrin domain. In humans it comprises 14 members named from NLRP1 to NLRP14. They play diverse roles in the immune system and cellular processes. Some members of the NLRP subfamily, such as NLRP1, NLRP3, and NLRP6, activate the inflammasome through the recruitment of an adaptor protein known as apoptosis-associated speck-like protein (ASC) to the pyrin domain (Motta et al., 2015).

The NRLP3 inflammasome has been extensively studied. Activation of the NLRP3 inflammasome in macrophages involves two steps: priming and activation. Priming is achieved through inflammatory stimuli, leading to NLRP3 and pro-IL-1β expression. Activation occurs when PAMPs and DAMPs promote NLRP3 inflammasome assembly and caspase-1-mediated IL-1β and IL-18 secretion (Yang et al., 2019). Amongst activation mechanism, ROS generation is a well identified trigger. Elevated plasmatic free fatty acid induced by consumption of a HFD can activate NLRP3 inflammasome in a ROS dependent manner (Wen et al., 2011). In atherosclerosis several factors can mediate NLRP3 activation Cholesterol crystals, which are present in the early and advanced stages of atherosclerosis, were found to strongly activate NLRP3 inflammasomes in macrophages. Oxidized LDL, known for its atherogenic properties, was found to induce cholesterol crystallization and activate priming signals that lead to IL-1β release (Duewell et al., 2010).

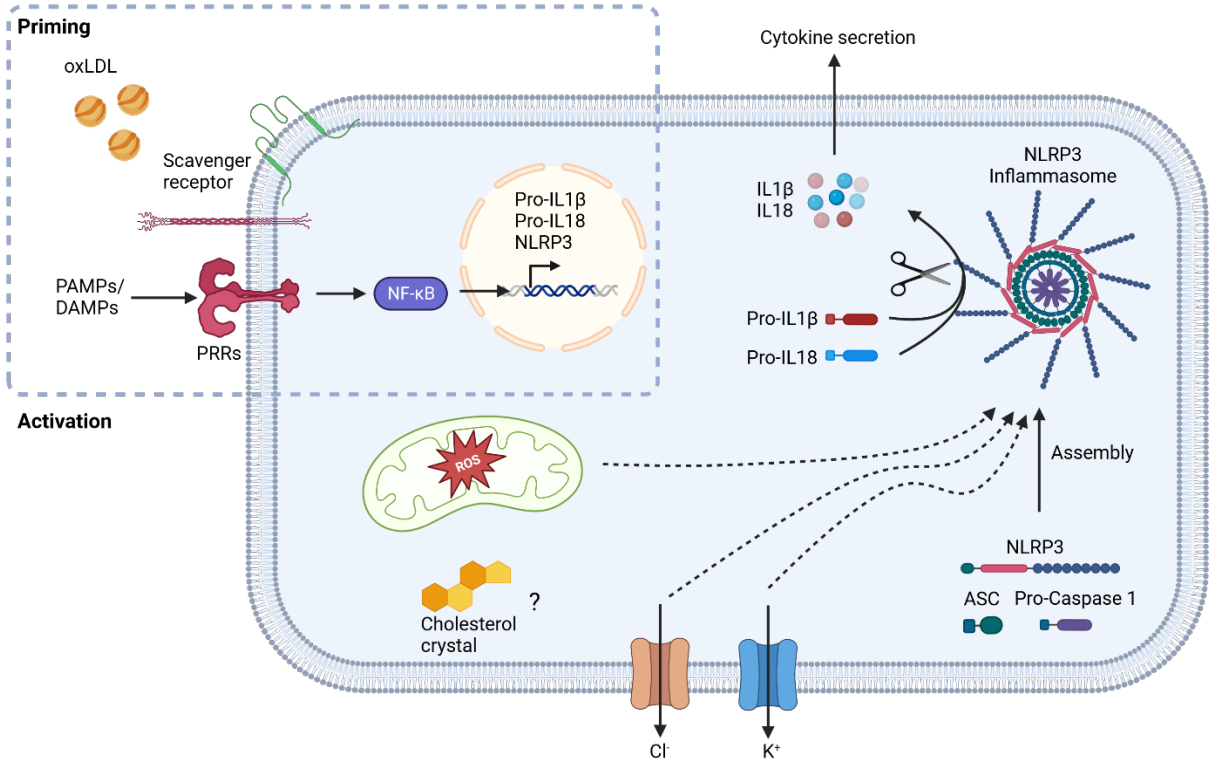

Figure 2. NLRP3 inflammasome activation

Priming requires the binding of PAMPs or DAMPs to PRRs. This interaction initiates the transcription of NLRP3, pro-IL-1β and pro-IL-18. The activation step is generated by PAMPs/DAMPs such as ATP or crystals/particles. This secondary

signal induces intracellular events such as the efflux of potassium ions, chlore ions and mitochondrial damage inducing ROS. Both priming and activation result in the assembly of NLRP3 oligomers with ASC and pro-caspase 1. The inflammasome cleaves pro-IL-1β and pro-IL-18 into their mature form which can be released by the cell. Adapted from (McKee and Coll, 2020). Made with Biorender.

2.2.2.2. Phagocytosis

Endocytosis englobes several mechanisms by which cells internalise proteins, fluids, microorganism, or apoptotic cells. Some mechanism can be used by all cell types of the body however other processes such as phagocytosis are more commonly employed by professional phagocytes such as macrophages. Phagocytosis is a complex process involving the engulfment of foreign particles commonly larger than 0.5µm however, phagocytosis can be involved in the uptake of far smaller particles (Rennick et al., 2021). It begins when certain receptors on the cell surface like scavenger receptors, opsonisation receptors or some TLRs recognize and bind their ligand. This engagement activates signalling pathways that lead to changes in the membrane composition and the actin cytoskeleton.

Remodelling of the actin cytoskeleton is crucial for generating membrane protrusions, known as pseudopodia, that cover the target particle. Different steps are involved in pseudopodia formation, including cortical cytoskeleton disruption, F-actin polymerization, and actin depolymerization at the base of the phagocytic cup while the phagosome is sealed at the distal end (Uribe-Querol and Rosales, 2020). After being internalized, the newly formed phagosome undergoes a process called phagosome maturation, where its membrane composition and contents are modified to transform into a phagolysosome (Levin et al., 2016). During this process, the phagosome undergoes a series of fusion events with early endosomes, regulated by the small GTPase Rab5, and facilitated by molecules like EEA1. As the maturation progresses, Rab5 is lost, and Rab7 appears on the membrane, mediating fusion with late endosomes. Concurrently, V-ATPase molecules accumulate on the phagosome membrane, leading to acidification of the phagosome interior. Finally, the phagosome fuses with lysosomes, becoming a phagolysosome. Various toxic substances are released in the phagolysosome to kill the engulfed microorganisms, including antimicrobial peptides, reactive nitrogen species like NO, which is generated by the high-output enzyme nitric oxide synthase 2 (iNOS2), whose expression is induced by different stimuli. The highly acidic phagolysosome is also equipped with the NADPH oxidase complex responsible for producing ROS such as the superoxide anion (O_2^-) and hydrogen peroxide (H_2O_2). All the elements enable the degradation of ingested microorganisms (Murphy and Weaver, 2017; Uribe-Querol and Rosales, 2020). Interestingly while native

LDL is ingested via clathrin mediated endocytosis, modified LDL enters the cells via phagocytosis (Schrijvers et al., 2007).

2.2.2.3. Cytokine production

Cytokines are small proteins that play an important role in intercellular communication. They are produced by various cell types of the immune system especially macrophages and lymphocytes, and regulate processes like inflammation, cellular proliferation, chemotaxis, and tissue repair. Cytokines bind to specific cell surface receptors, triggering signalling cascades that affect cell function and gene regulation. They can act locally (paracrine or autocrine) or travel to distant parts of the body (endocrine) (Arango Duque and Descoteaux, 2014).

Cytokine release can be initiated by some PRRs upon binding their ligand. Well described signalling PRRs are TLRs. They recruit specific TIR domain-containing adaptors like MyD88, TRIF, TIRAP (also called MAL), or TRAM, leading to different signalling pathways. Most TLRs interact with MyD88 alone while TLR4, TLR2/1 and TLR2/6 interact with the MyD88/TIRAP pair to initiate signal. On its N-terminus, MyD88 has a death domain which will interact with IL-1receptor associated kinase 4 (IRAK4) and IRAK1. The IRAK complex associates with TRAF6, which generates K63-linked polyubiquitin scaffolds. This signalling scaffold recruits TANK-binding kinase 1 (TAK1) and two other regulatory subunits. Due to its proximity with IRAK, TAK1 becomes phosphorylated resulting in the activation two pathways: the IKK complex-NF-κB pathway and the MAPK pathway.

The IKK complex is formed by three subunits: IKKα, IKKβ, and IKKγ. The activated TAK1 phosphorylates the IKKβ subunit leading to the ubiquitination and degradation of IκB, the cytoplasmic inhibitor of NF-κB. The released NF-κB enters the nucleus and drives transcription of genes encoding for TNF-α, IL-1β, IL-6. TAK1 also activates MAPKs, leading to the activation of AP-1 transcription factors and regulation of inflammatory responses (Kawasaki and Kawai, 2014).

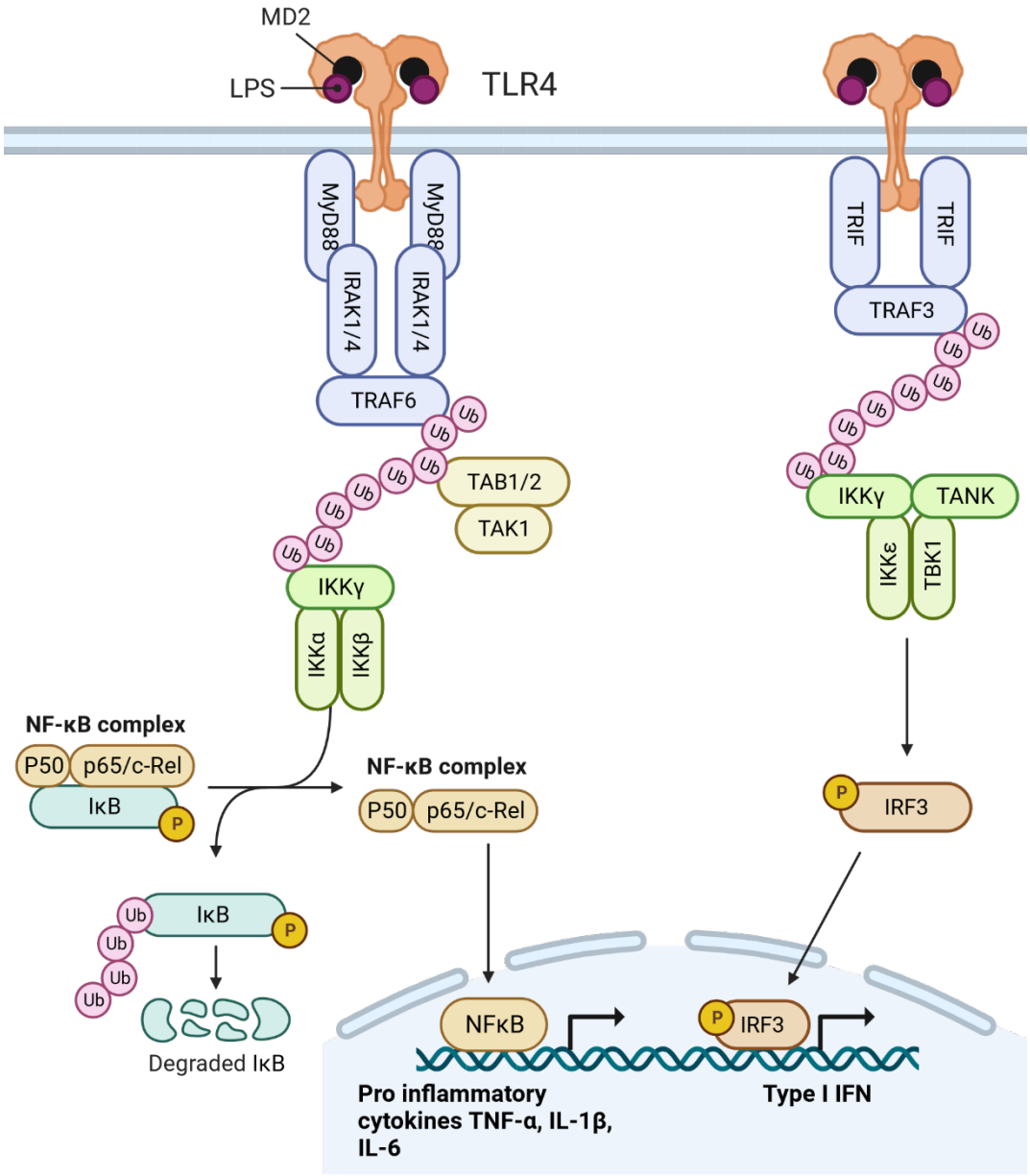

Figure 3. TLR4 signalling after LPS stimulation.

The TLR4 signalling can be MyD88 dependent or independent. MyD88 interacts with IRAK molecules associating with TRAF6 promoting polyubiquitin scaffolds. This leads to the phosphorylation of TAK1, leading to IKK complex recruitment and NF-κB activation. Alternatively, the TRIF dependent pathway also interacts with TRAF3 recruiting several kinases leading to the phosphorylation and activation of the transcription factor IRF3. The signalling cascade leads to the transcription of pro-inflammatory cytokines as well as type I IFN related genes. Adapted from (Murphy and Weaver, 2017; Papadakos et al., 2023). Made with Biorender.

Another TLR activation pathway is MyD88 independent and TRIF dependent. Only TLR4 and TLR3 can activate this alternative pathway that induces type I IFN production. TLR4 requires the help of TRAM which links TRIF to TLR4.

TRIF interacts with both TRAF6 and TRAF3. TRAF6 acts in a similar way to the MyD88 pathway leading to activation of the TAK1 complex and NF-κB and MAPK activation, resulting in the induction of inflammatory cytokines. TRAF3 forms K63-linked polyubiquitin chains. This scaffold then recruits IKKγ and TANK (TRAF family member associated NFκB activator), which associate with the IκB kinase ε (IKKε) and TBK1. TBK1 phosphorylates the transcription factor IRF3, allowing IRF3 to translocate to the nucleus and activate the expression of type I interferon genes (Ullah et al., 2016).

NLRs activation also induces cytokine production. The binding of ligands to NOD1 or NOD2 induces aggregation, leading to the recruitment of the kinase RIP2 through CARD-dependent interactions. RIP2 associates with the X-linked inhibitor of apoptosis protein (XIAP), the cellular inhibitor of apoptosis 1 (cIAP1), and cIAP2, forming a polyubiquitin scaffold, similar to TLR signalling. This scaffold facilitates the association of TAK1 and the IKK complex, leading to NFκB activation. The inflammasome also contributes to IL-1β and IL-18 production (see 2.2.2.1.3).

2.2.2.4. Macrophage polarization

Macrophages are sensitive cells that can quickly adapt to their microenvironment. In 1992 the effect of IL-4 on macrophages was firstly described and contrasted with the “classical” IFNγ activation. This “alternate activation” gave rise to a classification system where macrophages were either labelled M1 as pro-inflammatory or M2 as anti-inflammatory (Mills et al., 2000; Stein et al., 1992, p. 4). Nowadays this classification system seems oversimplified or obsolete as some macrophages do not fit in the M1/M2 spectrum. Other subcategories were created such as M2a, M2b, M2c, Mox, M4, tumour associated macrophages (TAM) and more. (Aras and Zaidi, 2017; Chinetti-Gbaguidi et al., 2015).

The “classical” activated macrophages are polarized by IFNγ, LPS or TNF-α. IFNγ binds to the functional IFNγ receptor (IFNGR). This receptor is composed of IFNGR1 and IFNGR2 chains. Both IFNGR1 and IFNGR2 lack intrinsic kinase/phosphatase activity and rely on signalling machinery for signal transduction. IFNγ signals primarily through the Jak-Stat pathway, a common mechanism used by many cytokines to regulate gene expression. IFNGR1 contains binding motifs for Janus tyrosine kinase 1 (Jak1) and signal transducer and activator of transcription 1 (Stat1), while IFNGR2 contains binding motifs for Jak2. When IFNγ binds to the receptor, conformational changes are induced allowing downstream signalling components to associate. Ligand binding triggers Jak2 autophosphorylation and activation, leading to Jak1 transphosphorylation by Jak2. Consequently, Stat1 is recruited, phosphorylated, and dissociated from the receptor. The Stat1 homodimer enter the nucleus, binds promoter elements, and initiate the transcription of IFNγ regulated genes (Schroder et al., 2004).

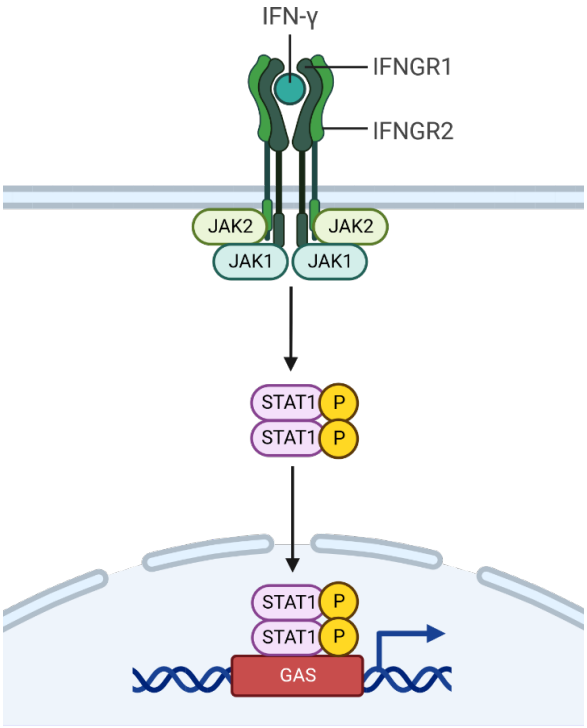

Figure 4. IFNγ signalling.

Upon IFNγ binding, conformational changes occur, enabling downstream signalling components to associate. This leads to Jak2 autophosphorylation and activation, which, in turn, causes Jak1 to be phosphorylated by Jak2. Subsequently, Stat1 is recruited, phosphorylated, and dissociated from the receptor. The phosphorylated Stat1 proteins form homodimers that enter the nucleus, bind to promoter elements, and initiate the transcription of genes regulated by IFNγ which leads to M1 polarisation. Made with Biorender.

Pro inflammatory macrophages will release several cytokines and chemokines including IL-1β, TNF-α, IL-6, IL-12, IL-23, CXCL9, CXCL10, which promote recruitment of leukocytes, pathogen elimination and can promote tissue damage.

In this thesis the work is mostly focalized on pro-inflammatory macrophages.

2.2.3. T cells

T cells are part of the adaptative immune system and originate from the lymphoid system. Each T cell is characterized by its own T-cell receptor (TCR) that is specifically targeted against an antigen. T cells can be classified based on their TCR components and based on certain markers they express. Most of the TCRs are composed of an α and a β chain. Once mature they either express a CD4 or a CD8 co-receptor and are called T CD4+ or T CD8+ cell. The co-receptors will determine what type of MHC they recognize and what type of response the cells have. Usually, T CD8+ cells recognize peptides bound to the MHC-I and have a cytotoxic role. Once activated they become effector cells and lyse target cells

presenting antigens, for example cells that are infected by a virus (Murphy and Weaver, 2017). On the other hand, T CD4+ cells can be T helper (Th) cells or regulatory (Treg) cells. Depending on their subtype, they secrete several cytokines that influence other immune cells. They also support the activation of T CD8+ cells and can regulate the inflammatory response. The differentiation of naïve T cells begins with antigenic stimulation triggered by the interaction between the TCR and CD4 co-receptor with the antigen bound to the MHC-II presented by professional antigen-presenting cells (APCs) (Luckheeram et al., 2012). Compared to the MHC-I which is expressed by almost all cells in the body, MHC-II is only expressed by a few immune cells. Amongst APCs are dendritic cells, macrophages, and B cells. These cells have the capacity of activating T CD4+ cells. The attachment of the antigen to the MHCII happens in the late endosome. After endocytic processes or autophagy, peptides are located in endosomes which increase their acidity over time leading to the progressive degradation of the engulfed object. The endosome fuses with MHC-II containing compartments when the peptide degradation process is optimal leading to small peptides composed by 12-18 amino acids. They can then attach to the MHC-II which is exported to the cell surface by class II-containing transport vesicles (Roche and Furuta, 2015). The activation of the TCR results in the proliferation and differentiation of naïve cells into specific effector cells. The type of effector cell lineage formed is influenced by the cytokines within the microenvironment, as well as factors such as antigen concentration, APC type, and costimulatory molecules (Luckheeram et al., 2012).

Several Th subsets exist including Th1, Th2, Th17, Th9. Each subset produces certain cytokines and therefore modulate their microenvironment.

Th1 cells play a central role in cell-mediated inflammation and delayed-type hypersensitivity reactions. They are crucial for immunity against intracellular pathogens and are characterized by producing cytokines like IFNγ, TNFα or IL-2. They promote a pro-inflammatory macrophage activation, upregulation of iNOS, and the elimination of intracellular pathogens. Their development is regulated by IL-12 (Raphael et al., 2015). Th17 cells are implicated in a range of inflammatory conditions as they produce IL-17 and IFNγ. The IL-17 cytokine plays a critical role in inflammation and host defence against extracellular pathogens. It contributes to various inflammatory processes by recruiting neutrophils, activating immune cells, enhancing B cell functions, and inducing the release of proinflammatory cytokines including TNF and IL-1β. While Th17 cells are associated with promoting inflammation and tissue damage, they can also have regulatory functions. They produce anti-inflammatory cytokines like IL-10, which can dampen inflammation and contribute to the downregulation of immune responses. The role of Th17 cells is complex and context-dependent, as they are involved in both pathogenic and protective mechanisms

in diseases. IL-6, IL-21, IL-23 and TGF-β signalling are regulating Th17 differentiation (Luckheeram et al., 2012; Raphael et al., 2015).

Tregs can be induced from a naïve CD4+ cell after antigen exposure by APCs or can come from distinct lineage cells (natural Treg). TGF-β exposure induces FOXP3 expression which is a key marker of Tregs. They maintain immunological tolerance to self and foreign antigens and negatively regulate the immune response post-pathogen clearance, protecting against immunopathology. Their main effector cytokines include IL10, TGF-β, and IL35. IL10 suppresses proinflammatory responses, limiting tissue damage from inflammation (Raphael et al., 2015).

2.3. Inflammation

2.3.1. Overview

Inflammation is a general term that refers to the localized establishment of the immune response following tissue damage at a specific location in the body. It results in the accumulation of fluid, plasma proteins, and white blood cells. It is a process that has been described during the first century by the Roman writer Aulus Celsus who defined the characteristic four signs of inflammation “Rubor et tumor cum calore et dolore” meaning redness and swelling with heat and pain. A few centuries later a fifth sign has been added by Galien, the “functio laesa” meaning loss of function. During the 19th century the cellular process of inflammation started to be described by several scientist like Rudolph Virchow, Henri Ducrochet, Rudolph Wagner, Julius Cohnheim and Elie Metchnikoff. In the 20th century major technological advances enabled further cellular and molecular description of the process (Granger and Senchenkova, 2010; Plytycz and Seljelid, 2003).

Two types of inflammation can be distinguished (Pahwa et al., 2023):

- The acute inflammation, which occurs after a harmful stimulus such as tissue damage due to trauma, pathogen invasion, irradiation, or toxic compounds. It starts quickly and lasts for a short time.
- The chronic inflammation, which is a slow, long-term inflammation that can last for several years. The extend of the inflammation varies with the cause. Several diseases are linked to chronic inflammation like diabetes, cancer, arthritis, and CVDs including atherosclerosis.

The Inflammatory response can be broken down into major steps (Chen et al., 2018):

1. Cell surface pattern receptor detect PAMPs or DAMPs.
2. Inflammatory pathways are activated leading to secretion and/or expression of inflammatory markers.
3. Inflammatory cells are recruited.

2.3.2. Leukocyte adhesion cascade

Danger signals can stimulate nearby cells such as endothelial cells, fibroblasts, immune cells which will secrete several messenger molecules contributing to hemodynamic changes. This includes bradykinin, histamine, NO production promoting vasodilatation and vascular permeabilization. The reduced blood flow speed and increased permeability enables increased leukocyte recruitment possibilities.

The initial adhesion step of leukocytes to the endothelium is called rolling. It is mediated by selectins. The P-selectin and E-selectin expressed by inflamed endothelial cells, interact with the P-selectin glycoprotein ligand 1 (PSGL1) expressed by leukocytes while the L-selectin expressed by leukocytes, interacts with CD34 expressed by activated endothelial cells. The interactions between selectins and their ligands are characterized by high on- and off-rates, determining bond formation and breakage speed. This bond strength increases with applied shear stress, and the rolling motion of cells facilitates the formation of new bonds before old ones break (Ley et al., 2007).

Rolling is reversible unless stronger bonds form resulting in firm adhesion also called arrest. This step is mediated by chemokines, integrins and immunoglobulin superfamily members VCAM-1 and intercellular adhesion molecule 1 (ICAM-1). Endothelial chemokines activate leukocyte ligand very late antigen 4 (VLA4 also called $\alpha_4\beta_1$-integrin) as well as lymphocyte function-associated antigen 1 (LFA1 also known as $\alpha_L\beta_2$-integrin) and macrophage antigen 1 (Mac1 also known as $\alpha_M\beta_2$-integrin) which bind to the endothelial VCAM-1 and ICAM-1 (Leick et al., 2014).

After arrest, the leukocytes flatten and crawl on endothelial cells in a step which is mainly mediated by Mac1 and ICAM-1. The transmigration can then initiate. Endothelial junctional molecules that also have ligands expressed by leukocytes, such as platelet/endothelial-cell adhesion molecule 1 (PECAM1; also known as CD31) and junctional adhesion molecule A (JAM-A), can move to the luminal surface to attract leukocytes. The leukocyte can then move between the tight junction of the endothelium and reach the tissue. Depending on the type of leukocyte and the location of the tissue, the transmigration can depend on various other ligands (Ley et al., 2007).

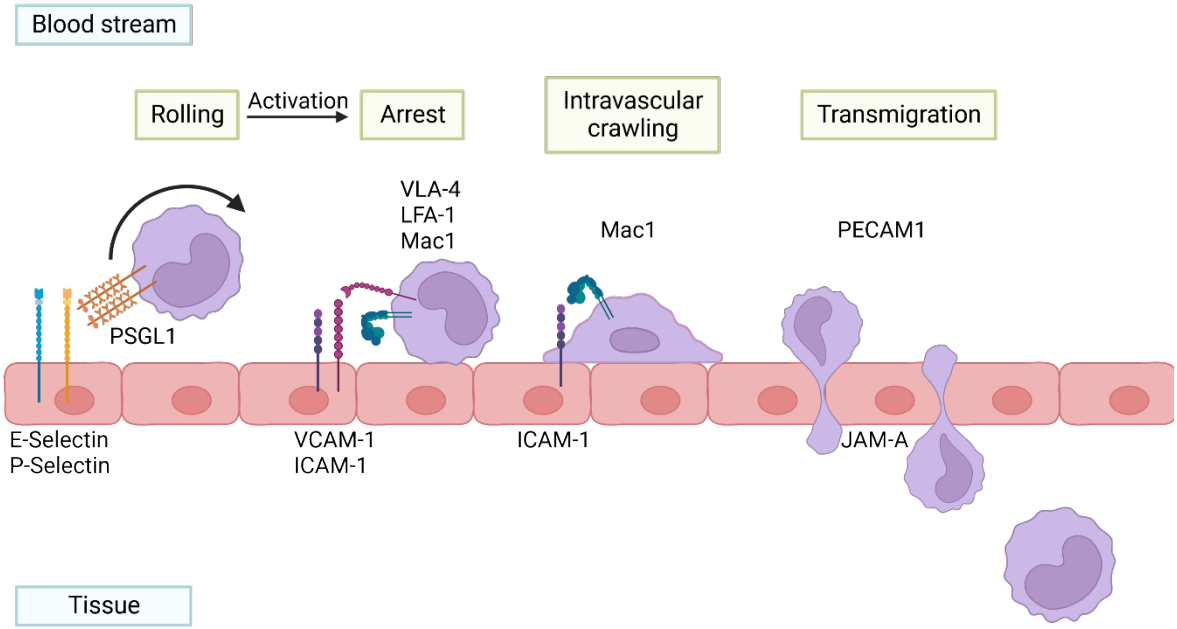

Figure 5. Leukocyte adhesion cascade

The leukocyte adhesion cascade comprises several steps resulting in the extravasation of leukocytes in the tissue. It starts with the capture of leukocytes followed by rolling which is mediated by selectins. The activation step is mediated by cytokines and leads to the arrest step which is mediated by integrins. It is followed by the flattening of the cell and intravascular crawling ultimately leading to transmigration. Adapted from (Ley et al., 2007). Made with Biorender.

2.3.3. Inflammatory cytokines

2.3.3.1. TNF

Chronic inflammation is a common factor in various diseases like atherosclerosis, rheumatoid arthritis, psoriasis, and inflammatory bowel diseases. Cytokines, particularly TNF, play a pivotal role in this process. TNF, mainly produced by monocytes and macrophages, impacts a range of functions through two receptors: TNFR1 and TNFR2. TNFR1 primarily promotes inflammation and tissue degradation, while TNFR2, only expressed by a few cell types, is associated with local homeostasis and cell survival. TNF has diverse roles participating in lymphoid organ development, and aiding tissue repair. It can help to resolve inflammation by inducing inflammatory cell apoptosis and exhibit cytostatic effects against tumours. However, TNF contributes to inflammation by triggering the production of pro-inflammatory mediators such as IL-6, orchestrating immune cell recruitment and survival, which can lead to tissue destruction. This cytokine is considered pro-atherogenic as it upregulates the expression of ICAM-1, VCAM-1 and MCP-1 (Fatkhullina et al., 2016).

2.3.3.2. IL-6

IL-6 is a versatile cytokine produced by various immune and stromal cells. It exerts its effects through the IL-6 receptor (IL-6R), composed of two subunits: CD126 and CD130. The receptor can signal via two pathways: the classical pathway, relevant for cells expressing both subunits, and trans-signalling, which involves the soluble form of CD126 and allows many cells to respond to IL-6. In the immune system, IL-6 plays essential roles. In innate immunity, it modulates haematopoiesis and neutrophil accumulation at infection sites by controlling granulopoiesis. In adaptive immunity, IL-6 promotes the differentiation of naive T cells into pro-inflammatory Th17 cells at the expense of regulatory T cells. IL-6 also supports T and B cell proliferation, survival, and cytokine production. IL-6's effects are mainly controlled via the classical pathway in homeostasis and immune regulation. However, trans-signalling becomes prominent in diseases. It contributes to leukocyte recruitment, apoptosis, maintenance of effector T cells, and inflammatory activation of the stroma. Overproduction of IL-6 is linked to various pathologies such as inflammatory arthritis, neuroinflammation, and Castelman's disease, where it drives inflammatory symptoms. While protective in infections, excessive IL-6 production in chronic inflammation leads to disease progression.

In experiments involving ApoE KO mice, the administration of recombinant IL-6 worsened the advancement of atherosclerosis. Furthermore, clinical investigations have demonstrated that levels of IL-6 in the bloodstream are elevated in individuals with unstable angina and are regarded as an autonomous contributor to the development of CAD (Tousoulis et al., 2016).

2.3.3.3. IL-1 family

IL-1 is an important cytokine mainly secreted by macrophages, monocytes, and dendritic cells. It consists of IL-1α and IL-1β, which exert similar effects through the IL-1 receptor (IL-1R1) and can also bind to the decoy receptor IL-1R2 and IL-1Ra. IL-1 is a classic endogenous pyrogen and plays a role in immune cell differentiation and function. IL-1α is released during cell necrosis and initiates sterile inflammation, while IL-1β, produced under inflammatory signals, promotes pro-inflammatory activity, vasodilatation, and activation of innate immune cells. IL-1β influences T cell differentiation into Th17. IL-1Ra prevents uncontrolled IL-1 signalling. IL-1 is pro-inflammatory and affects various cells and organs. Overproduction of IL-1β is associated with autoinflammatory and autoimmune disorders like Familial Mediterranean Fever. Elevated IL-1 levels are implicated in inflammatory pathologies such as heart disease and also contributes to tumour angiogenesis and metastasis (Kany et al., 2019; Murphy and Weaver, 2017). The IL-1 cytokines are

considered pro-atherogenic as they regulate activation of endothelial cells, macrophages and promote the differentiation of Th17 cells (Fatkhullina et al., 2016).

2.3.3.4. IL-17 family

IL-17 is a pro-inflammatory cytokine primarily secreted by Th17 lymphocytes. It binds to a receptor composed of IL-17RA and IL-17RC subunits, triggering signal transduction and inflammatory cytokine production. IL-17 has dual roles: homeostatic functions in host defence against bacterial and fungal infections by recruiting neutrophils, and pathogenic functions in chronic inflammatory and autoimmune diseases. In homeostasis, IL-17 aids in fighting infections by recruiting neutrophils and activating other immune cells. However, excess IL-17 secretion contributes to chronic inflammatory and autoimmune diseases by promoting the release of pro-inflammatory cytokines and chemokines, as well as matrix-degrading enzymes. In diseases like psoriasis, multiple sclerosis, and rheumatoid arthritis, IL-17 is implicated in tissue destruction (McGeachy et al., 2019). In atherosclerosis, IL-17 facilitates the chemokine-dependent infiltration of monocytes and neutrophils into the intima. It also controls the expression of VCAM-1 and stimulates the secretion of pro-inflammatory cytokines such as IL-6 and TNF-α. However, IL-17 can also have anti-atherogenic properties: it can increase IL-5 production and decrease IFNγ production (Fatkhullina et al., 2016).

Elevated levels of pro-inflammatory cytokines are present in both inflammatory sites and in the bloodstream of patients with chronic inflammatory conditions. These systemic cytokines have widespread effects on various organs, leading to diverse manifestations in chronic inflammatory diseases. Liver responses involve IL-6 and TNF inducing the synthesis of acute-phase inflammation proteins, elevating cardiovascular risk. The cardiovascular risk stems from these circulating cytokines and their impact on blood vessels (vascular wall inflammation) and lipid metabolism favouring atherosclerosis. IL-17, along with TNF, exacerbates atherosclerosis and thrombosis while inducing insulin resistance contributing to glucose metabolism disruption. Dysregulated cytokine production is a key player in chronic inflammatory disorders. Consequently, targeting these cytokines can be a promising therapeutic strategy for these diseases (Alfaddagh et al., 2020; Pahwa et al., 2023).

2.3.4. Inflammation in atherosclerosis

In recent years atherosclerotic plaques of mice and humans have been extensively described using single cell analysis methods such as single cell sequencing, Cytometry by time-of-flight (CyTOF) or cellular indexing of transcriptomes and epitopes by sequencing. The immune landscape of plaques is extremely diverse containing Macrophages, DCs, T

CD4+, T CD8+, B cells and some NK cells (Eberhardt and Giannarelli, 2022; Fernandez et al., 2019).

2.3.4.1. Macrophages in plaques

Macrophages are crucial cells in atherosclerosis onset and progression. Some are already resident in the aortic wall while others are recruited from the blood flow in form of monocytes (Yu et al., 2023). Their migration to plaques follows the leukocyte adhesion cascade (described in 2.3.2) and is mediated by chemokines like CCR2, CCR5, and CX3CR1, with the CCL2:CCR2 axis being particularly influential. Once in the tissue, the differentiation process relies on growth factors and cytokines in the microenvironment such as M-CSF and GM-CSF which can promote their differentiation into macrophages or DCs. Monocytes exhibit different roles based on their classifications, which further develop into different types of macrophages during atherosclerotic progression (Mehu et al., 2022).

Once differentiated into macrophages, they start to take up lipoproteins which constitute an early event in atherosclerosis. While the LDLr can clear lipoproteins, its expression decreases during foam cell formation due to high cellular cholesterol. Moreover, oxLDL formation in the artery wall, which is recognized by PRRs, initiates foam cell formation. Scavenger receptors (described in 2.2.2.1.1) like SR-A1, CD36, LOX1, play a major role by binding oxLDL (Moore and Freeman, 2006). These receptors internalize lipoproteins, leading to cholesterol ester hydrolysis in the endolysosomal compartment. Lipoprotein modification by proteases and lipases in the intima can also induce foam cell formation, independently of scavenger receptors. These various pathways, rather than a single modification model, collectively contribute to foam cell development in atherosclerosis.

Defective cholesterol trafficking in macrophages can result from excessive cholesterol uptake, leading to various pathological processes. Cholesterol stored as cholesteryl ester is relatively inert, but free cholesterol can be harmful. Elevated free cholesterol levels in ER membranes hinder proper cholesterol esterification by ACAT1, promoting further accumulation. Dysfunctional trafficking of free cholesterol from lysosomes hampers cholesterol efflux and amplifies inflammation. These disruptions contribute to ER stress, increases macrophage apoptosis and impairs efferocytosis, resulting in secondary necrosis and the formation of the necrotic core in advanced atherosclerotic plaques. Cells respond to excessive lipid accumulation by upregulating pathways that facilitate lipid efflux. Macrophage transporters like ABCA1, ABCG1, and SR-B1 mediate lipid efflux. Transcriptional upregulation of ABCA1 and ABCG1 is prompted by cellular cholesterol levels through liver X receptors, which have anti-inflammatory effects. Autophagy plays a crucial role in cholesterol efflux through processes like lipophagy, where the autophagy machinery targets lipid droplets for degradation, making cholesterol available for efflux via

an ABCA1-dependent pathway. These efflux pathways promote lipid homeostasis and mitigate inflammation, thus serving as atheroprotective mechanisms (Moore et al., 2013).
Cholesterol crystals present in plaques, even in early lesions, induce the NLRP3 inflammasome when engulfed by macrophages. These crystals prompt lysosomal destabilization, releasing proteases or ROS that activate NLRP3, leading to cytokine IL-1β secretion. CD36 plays a key role in cholesterol crystal nucleation and lysosomal disruption, contributing to NLRP3 inflammasome activation. Cholesterol-loaded macrophages can also form intracellular cholesterol crystals triggering NLRP3 activation (Moore et al., 2013).

TLR signalling pathways also contribute to atherosclerosis development. Indeed, oxLDL species are also proposed ligands for TLRs. Minimally oxidized LDL triggers TLR4 signalling, moderately oxidized LDL signals via the TLR4-TLR6 heterodimer, and oxidized phospholipids and fatty acids activate TLR2 and CD36 cooperative signalling. Free cholesterol enrichment in macrophage membranes also activates various TLRs, contributing to sustained inflammation in atherosclerotic plaques (Kong et al., 2022; Moore et al., 2013).

Overall, the cholesterol crystals and oxLDL triggering NLRP3 and TLR signalling lead to an “M1” phenotype. Moreover, cholesteryl esters like linoleate and 7-ketocholesteryl-9-carboxynonanoate activate M1 polarization through the TLR4 NF-κB pathways. On the other hand, 9-oxononanoyl-cholesterol promotes an anti-inflammatory M2 phenotype by increasing TGF-β secretion. Sphingosine-1-phosphate (S1P) switches mouse macrophages from M1 to M2 through S1P1 receptor activation. Omega-3 polyunsaturated fatty acids, like resolvin D1, shift macrophages towards an M2-like phenotype, and conjugated linoleic acid induces an anti-inflammatory M2 phenotype (Eligini et al., 2023).
Aside from M1/M2 phenotypes, the complex plaque microenvironment induces further phenotypic diversity, such as Mox, M(Hb), HA-mac, Mhem, and M4 macrophages, each having distinct roles and markers. Oxidized phospholipids can lead to a Mox phenotype driven by NFE2L2 transcription factor activation, characterized by redox-regulatory gene expression. In advanced atherosclerotic mouse lesions, about 30% of macrophages display the Mox phenotype, while its presence in human lesions requires further study. In haemorrhagic areas of atherosclerotic plaques, distinct macrophage subsets are linked to haemoglobin and erythrocyte presence. M(Hb) macrophages express CD206 and CD163, scavenger receptors for haemoglobin/haptoglobin, essential for effective haemoglobin removal after intraplaque haemorrhage. Ingested erythrocytes release heme, prompting the Mhem phenotype. Activating transcription factor 1 activation triggers heme oxygenase-1, liver X receptor-α, and ATP-binding cassette transporter ABCA1 expression, offering

atheroprotective functions and preventing foam cell formation. HA-mac macrophages have high CD163 and HO-1 levels but low human leukocyte antigen-DR levels. Macrophages polarized by CXCL4 lead to M4 macrophages characterized by MMP-7 expression. They are similar to M1 but have a reduced phagocytic activity (Chinetti-Gbaguidi et al., 2015; Eligini et al., 2023; Kong et al., 2022; Mehu et al., 2022).

Single cells technologies could further confirm macrophage heterogeneity within human plaques. Some macrophages display a heightened activation with high inflammation levels and genes related to inflammatory responses, toll-like receptor binding, and oxidoreductase activities. Other macrophage types exhibit genes involved in cholesterol uptake and metabolism, lipid accumulation, and foam cell attributes, with reduced pro-inflammatory signalling indicating an anti-inflammatory role for these macrophages. Macrophages of plaques from patients that experienced stroke or transient ischaemic attack are different from asymptomatic patients. Interestingly TLR4 signalling cascades, IFNγ, IL-1 and IL-6 signalling is upregulated in asymptomatic patients while CXCR4, IL-21, IL-35 signalling events are upregulated in symptomatic patients (Fernandez et al., 2019).

2.3.4.2. T cells in plaques

Interestingly the T cell population in plaques is abundant and extremely diverse. Th1 cells are prevalent in atherosclerotic plaques and promote atherosclerosis by activating macrophages and other cells. They are enriched in plaques of patients with recent stroke. Their cytokine profile includes IFNγ, IL-2, IL-3 and TNF, intensifying the inflammatory response. Lack of IFNγ, its receptor, or T-bet protects against atherosclerosis, while IFNγ administration increases it. IFNγ influences vascular smooth muscle cell proliferation and macrophage polarization, affecting plaque stability. Although other Th1 cell cytokines may be relevant, limited specific research exists on their impact in atherosclerosis (Chen et al., 2022; Saigusa et al., 2020).

Treg cells play a protective role in atherosclerosis, with lower Treg cell numbers associated with increased risk of cardiovascular events. The specificity of Treg cell antigens remains largely unknown, but their activation leads to the secretion of anti-inflammatory cytokines like IL-10 and TGFβ, contributing to atheroprotection. The existence of LDL-reactive Treg cells responding to atherosclerosis-related antigens, such as ApoB peptides, has been demonstrated using MHC class II tetramers. However, in atherosclerosis, Treg cells can undergo pathological changes in response to disease progression. In later stages of atherosclerosis, Treg cell numbers decrease while effector T cells increase. Treg cells can exhibit dual expression of FOXP3 and T-bet, losing their immunosuppressive and atheroprotective abilities. The stable expression of FOXP3 is vital for Treg function. Factors

like increased methylation of the FOXP3 locus, elevated cholesterol levels, decreased IL-2 signalling, and alternative splicing mechanisms might trigger the loss of FOXP3 expression in Treg cells (Saigusa et al., 2020). Most other Th cell types like Th2, Th17 or Th9 display controversial or unclear results whether their role is atheroprotective or not (Kong et al., 2022).

2.4. Immunometabolism

Metabolism is the collection of chemical reactions that sustain life in organisms. Its main functions include converting nutrients into cellular energy, producing molecular building blocks and eliminating waste. Metabolic reactions are categorized as catabolic (breaking down compounds like glucose) or anabolic (building up compounds like proteins), with catabolism releasing energy and anabolism consuming it. Enzymes drive these reactions, acting as catalysts to facilitate and regulate the processes. Metabolic pathways are similar across diverse species, reflecting their shared evolutionary origins. Diseases such as diabetes, metabolic syndrome, and cancer have the potential to disturb regular metabolic processes, rendering metabolism a popular field of research.

Immunometabolism is an expanding field that explores the intricate relationship between immune responses and metabolic processes. Cellular metabolism also plays a crucial role in activating and regulating immune cells, influencing their functions and adaptations. Indeed, various immune cell types employ distinct metabolic pathways based on their specific requirements. These metabolic pathways are further influenced by external stimuli such as DAMPs, PAMPs, cytokines, and chemokines, which immune cells encounter. Chronic metabolic inflammation, is a key feature of metabolic disorders, impacting conditions like type 2 diabetes and fatty liver disease. This metabolic-immune interplay is implicated in various pathologies, including cancer and autoimmune disorders (Chavakis, 2022). Given that macrophages are the central focus of this thesis, the following sections describe important pathways in macrophage metabolism.

2.4.1. Macrophage Metabolism

Due to the ability of macrophages to adjust their characteristics in response to their microenvironment, they can adapt their metabolic profiles to their specific roles in homeostasis and inflammation. Once stimulated, M1 and M2 macrophages present different metabolic characteristics (Figure 6). Indeed, M1 macrophages are characterized by increased glycolysis activity, pentose phosphate pathway (PPP) activity, fatty acid synthesis. They present a divided tricarboxylic acid (TCA) cycle due to the synthesis of the

metabolite itaconate, leading to the accumulation of succinate and citrate. Moreover, M1 macrophages produce NO by converting arginine into citrulline. In contrast, M2 macrophages rely on oxidative phosphorylation (OXPHOS) and fatty acid oxidation, with reduced glycolysis and PPP activity. They convert arginine to ornithine releasing urea (Geeraerts et al., 2017).

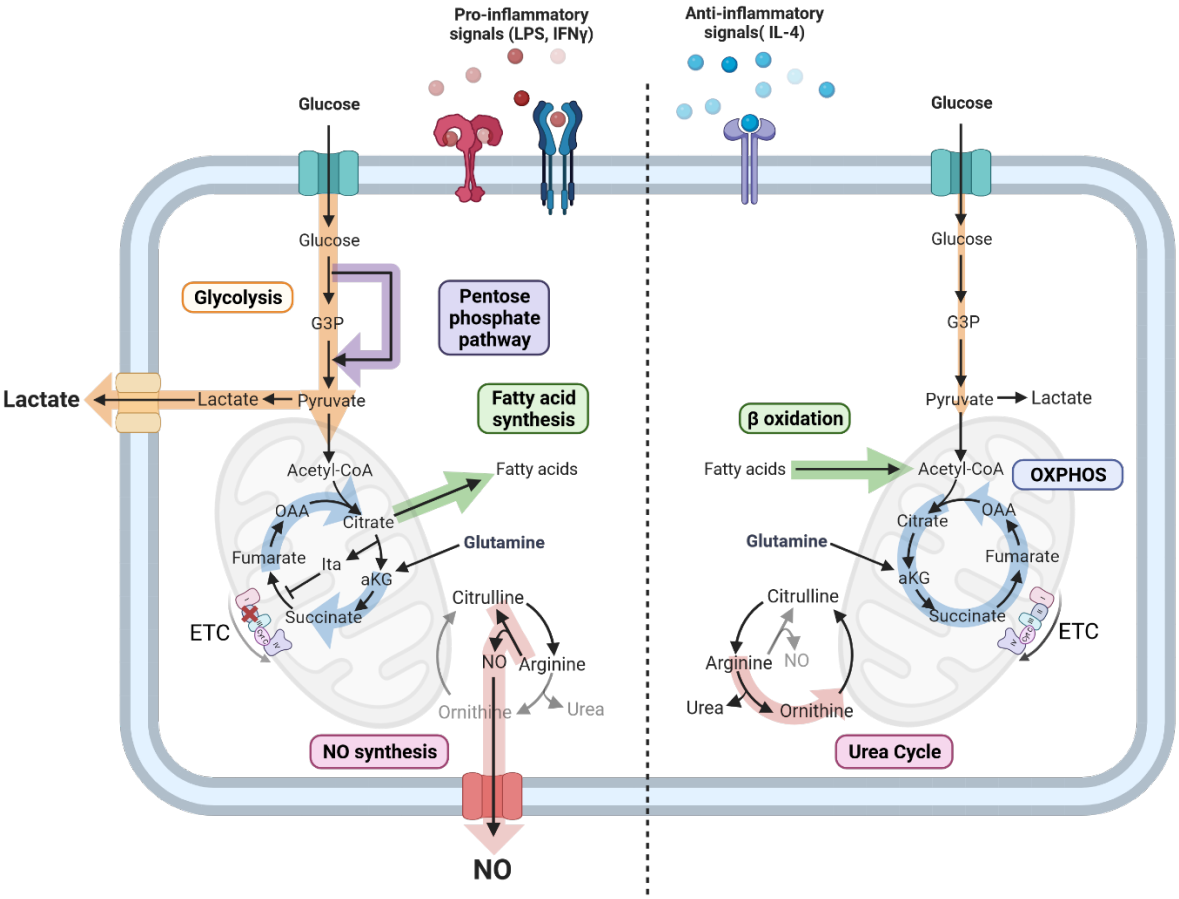

Figure 6. Metabolic differences between pro-inflammatory and anti-inflammatory macrophages

Activation of macrophages with LPS and IFNγ promotes the M1 phenotype and major metabolic changes. M1 macrophage metabolism is characterized by enhanced aerobic glycolysis, converting glucose into lactate. This also promotes the flux through the pentose phosphate pathway. The tricarboxylic acid (TCA) cycle is divided leading to the accumulation of succinate and citrate. Citrate is used for the generation of fatty acids as well as itaconate which inhibits the succinate dehydrogenase. Another aspect of M1 macrophage metabolism is the conversion of arginine to citrulline generating NO. On the other hand, M2 macrophages do rely more on OXPHOS to produce ATP and less on glycolysis. The TCA cycle is fuelled with β-oxidation and glutamine anaplerosis. Instead of producing NO, M2 macrophages convert arginine into urea and ornithine. Adapted from (Geeraerts et al., 2017). Made with Biorender.

The next sections will give details on M1 relevant metabolic pathways such as glycolysis, the TCA cycle as wells as the urea cycle.

2.4.1.1. Urea cycle

The urea cycle is a metabolic pathway in ureotelic organisms that converts ammonia, mainly generated in liver mitochondria, into urea. This cycle was discovered by Hans Krebs and Kurt Henseleit in 1932 (Krebs, 1973). Urea production occurs primarily in the liver, which is then released into the bloodstream for excretion through urine. The cycle involves several steps spanning both mitochondria and cytosol. It begins with the conversion of ammonia and CO_2 into carbamoyl phosphate, catalysed by carbamoyl phosphate synthetase I in the mitochondrial matrix. This step consumes 2 ATP. The carbamoyl phosphate acts as a carbamoyl group donor and enters the urea cycle. The next step of the cycle involves the donation of the carbamoyl group to ornithine to form citrulline. The second amino group, contributed by aspartate, joins the cycle by forming argininosuccinate, which is then cleaved into arginine and fumarate. Arginine is further cleaved into urea and ornithine. Urea is released from the cycle, while ornithine is recycled for another round. The cycle involves both mitochondrial and cytosolic enzymes, with some intermediate compounds channelled directly between enzymes to facilitate efficient reaction progression (Nelson et al., 2021).

Interestingly this cycle plays an important role in macrophages and exhibits great differences between pro-inflammatory and anti-inflammatory macrophages. Indeed, M1 macrophages highly express iNOS which converts arginine into citrulline releasing NO. On the other hand, M2 macrophages express arginase-I, the enzyme catalysing the conversion from arginine to ornithine releasing urea. Another enzyme, arginase-II catalyses the same process, however it is expressed by M1 macrophages. The function of arginase-II might have a distinct role in macrophage inflammatory responses compared to Arg-I, with recent research aiming to clarify its function, particularly in chronic inflammatory conditions like obesity-related insulin resistance, type-II diabetes, and atherosclerosis (Yang and Ming, 2014).

2.4.1.2. Glycolysis

Glycolysis is a fundamental metabolic pathway that breaks down glucose into pyruvate through a series of enzyme-catalysed reactions, producing ATP and NADH. Its elucidation marked a significant milestone in biochemical research. Glycolysis is widely conserved across species and is a primary source of energy in various tissues. Despite some variations, the core chemistry of glycolysis remains consistent throughout evolution.

Glycolysis involves the breakdown of glucose into two pyruvate molecules through a series of 10 steps, with the initial 5 steps forming the preparatory phase. Glucose is phosphorylated at C-6, resulting in glucose 6-phosphate. This compound is then converted to fructose 6-phosphate and subsequently phosphorylated at C-1 to produce fructose 1,6-bisphosphate. In these steps, ATP serves as the phosphoryl group donor resulting in the

use of 2 ATP molecules for one glucose molecule. Fructose 1,6-bisphosphate is broken down into dihydroxyacetone phosphate and glyceraldehyde 3-phosphate, marking the "lysis" step. The dihydroxyacetone phosphate is converted to another glyceraldehyde 3-phosphate, completing the first phase (Nelson et al., 2021).

The second phase of glycolysis is called “payoff phase”. Each glyceraldehyde 3-phosphate is oxidized and phosphorylated using inorganic phosphate, forming 1,3-bisphosphoglycerate releasing NADH. During the step 1,3-bisphosphoglycerate forming 3-phosphoglycerate, ATP is released. This ATP can compensate the ATP loss from the preparatory phase of glycolysis. 3-phosphoglycerate is later converted in 2-phosphoglycerate and further dehydrated to form phosphoenolpyruvate. Energy is released during the conversion of phosphoenolpyruvate into pyruvate, leading to the phosphorylation of two ADP molecules into ATP. Accounting for the two ATP molecules initially invested the net production of the reaction is 2 ATP per glucose molecule. Additionally, energy is conserved in the formation of two NADH molecules for each glucose molecule (Nelson et al., 2021). The product of glycolysis, pyruvate can be converted to lactate in the cytosol, replenishing NAD^+ for glycolysis-driven ATP production. Alternatively, pyruvate can contribute to alanine synthesis or enter mitochondria in eukaryotic cells.

Classically activated M1 macrophages are marked by a transition from oxidative phosphorylation (OXPHOS) to increased glucose uptake and aerobic glycolysis. Due to the increased lactate production by pyruvate, the extracellular acidification increases which is a measurable parameter in M1 macrophages. This metabolic shift coincides with upregulated expression of glycolytic genes, increased bactericidal activity, ROS generation, and pro-inflammatory cytokine release. The glycolytic shift is regulated by several enzymes, notably Hexokinase 1 (HK1), which governs the initial rate-limiting step in glycolysis. HK1 is not only pivotal in glucose to glucose-6-phosphate conversion but also crucial for pro-inflammatory functions like inflammasome activation (Kolliniati et al., 2022).

2.4.1.3. TCA cycle

The Tricarboxylic acid (TCA) cycle also called Krebs cycle has been discovered by Hans Krebs and William Johnson in 1937 using pigeon breast muscle (Krebs and Johnson, 1937; Wilson et al., 2010). It is a cyclic metabolic pathway that facilitates the oxidation of acetyl-CoA which can be formed by pyruvate. In the mitochondria, the pyruvate dehydrogenase complex, orchestrates the irreversible oxidative decarboxylation of pyruvate, producing acetyl-CoA, CO_2 and NADH. The NADH then transfers electrons to the respiratory chain, ultimately leading to ATP generation.

The TCA cycle begins with the condensation of acetyl-CoA and oxaloacetate, forming citrate, a reaction catalysed by citrate synthase. The next reactions are catalysed by the

enzyme aconitase. It catalyses the reversible conversion of citrate to isocitrate through the intermediate formation of cis-aconitate. The transformation involves the addition of water to cis-aconitate, leading to either citrate or isocitrate formation. The equilibrium is skewed toward isocitrate due to its rapid consumption in the next cycle step.

In the subsequent step, isocitrate dehydrogenase facilitates the oxidative decarboxylation of isocitrate into α-ketoglutarate (aKG) reducing NAD^+ to NADH. The next step of the cycle entails another oxidative decarboxylation, where aKG is converted to succinyl-CoA and CO_2 via the aKG dehydrogenase complex also reducing NAD^+ to NADH. In the following step of the TCA cycle, succinyl-CoA undergoes a reaction catalysed by succinyl-CoA synthetase. This reaction liberates the energy stored in the thioester bond of succinyl-CoA, which results in the formation of succinate releasing GTP or ATP.

Following the formation of succinate from succinyl-CoA, the next step involves the oxidation of succinate to fumarate, catalysed by succinate dehydrogenase (SDH). In eukaryotes, this enzyme is integral to the mitochondrial inner membrane. SDH contains various iron-sulfur clusters and a covalently bound FAD molecule, serving as an entry point for electrons into the electron transport chain in the inner mitochondrial membrane. The reversible hydration of fumarate to L-malate is facilitated by fumarase. Fumarase exhibits high stereospecificity, preferring the hydration of the trans double bond of fumarate. In the reverse direction (from L-malate to fumarate), fumarase maintains equal stereospecificity, where D-malate is not accepted as a substrate. In the final step of the citric acid cycle, L-malate dehydrogenase catalyses the oxidation of L-malate to oxaloacetate, simultaneously reducing NAD^+ to NADH. Under standard thermodynamic conditions, the equilibrium of this reaction favours oxaloacetate formation (Nelson et al., 2021).

Overall, for one Acetyl-CoA molecule oxidized by the TCA cycle, 3 NADH, 1 $FADH_2$ and either 1 ATP or 1 GTP are produced. While the ATP gain does not seem important at first glance, each NADH and $FADH_2$ can contribute to ATP production via the electron transport chain during OXPHOS. Each NADH molecule undergoing OXPHOS can generate 2.5 ATP while each $FADH_2$ can generate 1.5 ATP. Therefore, it is possible with one glucose molecule undergoing glycolysis, generating two pyruvate, two Acetyl-CoA entering the TCA cycle, and subsequently transferring the electrons to oxygen via OXPHOS, to obtain a total of 32 ATP molecules (Cooper, 2000; Nelson et al., 2021).

In macrophages the TCA cycle can be linked to pro-inflammatory as well as anti-inflammatory properties. Indeed, the conversion of citrate to acetyl-CoA via ATP-citrate lyase promotes the M1-like phenotype by facilitating histone acetylation on pro-inflammatory gene promoters (Kolliniati et al., 2022). Moreover, while shifting their metabolism towards glycolysis, M1 macrophages increase succinate levels and enhance

mitochondrial oxidation of succinate through SDH. This process, combined with elevated mitochondrial membrane potential, leads to the generation of mitochondrial ROS. Inhibiting succinate oxidation, promotes an anti-inflammatory response (Mills et al., 2016).
On the other hand, the accumulation of aKG steers macrophage metabolism towards fatty acid oxidation and collaborates with JMJD3 histone demethylase to activate an M2-like transcriptional program (Kolliniati et al., 2022).

2.4.2. Itaconate

One major metabolic hallmark of activated pro-inflammatory macrophages is itaconate. This metabolite was discovered in 1836 when Samuel Baup noticed an unknown compound during citric acid distillation (Baup, 1836). In 1840, Gustav Crasso synthesized the same compound, naming it itaconate, an anagram of (cis)-aconitate (Crasso, 1840). It was later found in 1931 to be produced by the fungus *Aspergillus itaconicus*. In 2011, 175 years after itaconates initial discovery, it was discovered that mammalian immune cells could also synthesize itaconic acid (Strelko et al., 2011). In 2013, Michelucci *et al.* showed that the immune responsive gene 1 (IRG1 also known as aconitate decarboxylase 1, ACOD1), was accountable for itaconate synthesis in pro-inflammatory macrophages (Michelucci et al., 2013). Indeed, IRG1 catalyses the decarboxylation of cis-aconitate generating itaconate.
To understand how itaconate impacts macrophage metabolism several strategies have been employed. Some consists in treating murine macrophages with itaconate or itaconate derivatives such as dimethyl itaconate (DI) or 4-octyl-itaconate (4OI), while others use *Irg1* deficient mouse models or cell lines. Most studies use a combination of several methods to understand the impact of itaconate on macrophage immune response and metabolism.
Addition of itaconate to RAW 264.7, a murine macrophage cell line, for 6h promoted the increase of succinate concentration. This observation could be repeated on murine bone marrow derived macrophages (BMDM) stimulated with LPS (Cordes et al., 2016). This same study demonstrated that itaconate inhibits SDH promoting the accumulation of succinate which was further demonstrated by Lampropoulou et al., (Cordes et al., 2016; Lampropoulou et al., 2016). Another metabolic modulation induced by itaconate is linked to glycolysis. Indeed, the addition of 4OI in the culture medium could inhibit GAPDH activity and therefore inhibit glycolysis in RAW 264.7 and BMDMs (Liao et al., 2019). Another metabolic pathway affect by itaconate is the NO synthesis. Indeed, LPS-IFNγ stimulated BMDMs of IRG1 KO mice produce more NO (Lampropoulou et al., 2016). Interestingly NO also affects itaconate: iNOS KO cells produced more itaconate after LPS-IFNγ stimulation (Bailey et al., 2019).

As a high glycolytic activity, as well as NO production are hallmarks of inflammatory macrophages, the itaconate induced reduction of both demonstrates the anti-inflammatory potential of this metabolite.

Itaconate is also linked to the macrophage immune response. Indeed, an increase of several pro-inflammatory cytokines such as IL-1β, IL-6 but not TNFα could be observed in IRG1 KO BMDMs after LPS stimulation linking the absence of itaconate to increased inflammation markers (Lampropoulou et al., 2016). Experiments involving 4OI showed that itaconate could alkylate and inactivate kelch-like ECH-associated protein 1 (KEAP1), an inhibitor of the anti-inflammatory transcription factor NRF2, thereby reducing IL-1β secretion and promoting glutathione (GSH) synthesis (Mills et al., 2018). Furthermore, 4OI could block the NLRP3- NIMA-related kinase 7 (NEK7) interaction, inhibiting the NLRP3 inflammasome activation. In Irg1 KO BMDMs, the NLRP3 inflammasome activation was increased confirming the implication of itaconate (Hooftman et al., 2020). Another itaconate derivative DI, could also induce NRF2 activation and GSH synthesis and inhibited IL-6 secretion via ATF3 and IκBζ (Bambouskova et al., 2018).

Overall itaconate can push pro-inflammatory M1 macrophages towards an M2 phenotype by modulating metabolic pathways and dampening pro-inflammatory cytokine secretion. However, differences between DI, 4OI and unmodified itaconate treatment have been highlighted. IRG1 KO BMDMs treated with itaconate showed a succinate accumulation which could not be observed with DI or 4OI. On the other hand, NRF2 activation could not be observed with unmodified itaconate and required either DI or 4OI treatment (Swain et al., 2020). It has been shown that DI does not metabolize into itaconate (ElAzzouny et al., 2017; Swain et al., 2020). However, this statement is controverted with 4OI as some studies show that 4OI metabolizes into itaconate (Hooftman et al., 2020) while others do show the opposite (Swain et al., 2020). The different experiments demonstrate that itaconate derivatives could affect certain pathways that unmodified itaconate cannot activate.

3. AIMS OF THE STUDY

Recent years have provided substantial evidence indicating the role of itaconate in reducing ROS, alleviating inflammation, and influencing certain metabolic pathways. While atherosclerosis was traditionally attributed to LDL deposition, growing evidence underscores the intertwined relationship between inflammation and atherogenesis. The therapeutic potential of anti-inflammatory therapy in cardiovascular diseases has been highlighted by studies such as the CANTOS trial, where treatment with an anti-IL1β monoclonal antibody reduced major cardiovascular events (Everett et al., 2020). Patients given colchicine, theorized to inactivate the NLRP3 inflammasome, also demonstrated reduced cardiovascular risks in the COLCOT trial (Tardif et al., 2019). Therefore, itaconate's modulation of NLRP3 and IL1β pathways provides another layer of interest. As of today, no study was published demonstrating the effects of itaconate on atherosclerosis. While more evidence shows that TLR4 activation as well as IFNγ signalling is relevant in atherosclerosis (Roshan et al., 2016; Voloshyna et al., 2014), only a few studies investigated metabolic changes caused by itaconate after LPS-IFNγ double stimulation. Moreover, it has recently been shown that itaconate can also affect other immune cells despite being mostly synthetized by monocytes/macrophages (Zhao et al., 2022).

The work of this thesis therefore aims:

- To assess plaque severity in two different atherosclerosis models that do not express IRG1.

- To investigate the systemic role of itaconate on other immune cell types in inflammation.

- To study the effects of LPS INFγ double stimulation on macrophage metabolic pathway in the presence or absence of itaconate.

4. MATERIALS AND METHODS

4.1. Ethics statement

This study was carried out at the University of Luxembourg and at the University of Saarland in strict accordance with the recommendations to European and German guidelines for the welfare of experimental animals. Animal experiments were approved by the Saarland state's "Landesamt für Gesundheit und Verbraucherschutz" in Saarbrücken, Germany under the number 37/2019.

4.2. Animals

Mouse breeding and animal experiments were performed in the animal facilities of the University of Saarland according to European and German guidelines for the welfare of experimental animals. The IRG1 KO mice were generated by Dr. Haruhiko Koseki at the RIKEN Institute (Yokohama, Japan) using stem cells obtained from the Knockout Mouse Project Repository (KOMP) under the strain ID: $Irg1^{tm1a(KOMP)Wtsi}$. The ApoE KO and LDLr KO mice were purchased from the Jackson Laboratory, strain number: 002052 and 002207 respectively (Ishibashi et al., 1993; Piedrahita et al., 1992). For the atherosclerosis experiments we used $Irg1^{-/-}Apoe^{-/-}$ and $Irg1^{-/-}Ldlr^{-/-}$ as KO mice while $Irg1^{+/+}Apoe^{-/-}$ and $Irg1^{+/+}Ldlr^{-/-}$ were used as wild-type (WT) control. For the metabolomics experiments we used $Irg1^{-/-}$ as KO mice while $Irg1^{+/+}$ were used as WT control. The genotype of the mice was confirmed by polymerase chain reaction (PCR) prior to experimentation.

Gene	Target	Sequence (5'-3')
Ldlr	KO Reverse	AATCCATCTTGTTCAATGGCCGATC
Ldlr	Common Forward	CCATATGCATCCCCAGTCTT
Ldlr	WT Reverse	GCGATGGATACACTCACTGC
Apoe	KO Reverse	GCCGCCCCGACTGCATCT
Apoe	WT Reverse	TGTGACTTGGGAGCTCTGCAGC
Apoe	Common Forward	GCCTAGCCGAGGGAGAGCCG
Irg1	WT Forward	GCCTTGTGTGAGAGAGAGATCTTCC
Irg1	WT Reverse	TTCAGATCCTCCCCTGTCCAGTTCC
Irg1	KO Forward	GAGATGGCGCAACGCAATTAATG
Irg1	KO Reverse	GAGGACCTGAATTTGGTTCCAAGGC

Table 1: List of Primers for genotyping

4.3. Atherosclerosis induction

To induce atherosclerosis, 6 to 12 weeks old LDLr or ApoE KO animals were given a high fat diet for 12 weeks (Envigo, TD.88137). They were then sacrificed with an overdose of isoflurane (Baxter) inhalation followed by blood collection from the vena cava. The blood was placed in an Ethylenediaminetetraacetic acid (EDTA) coated tube (Sarstedt, Microvette) for flow cytometry and plasma collection. The plasma cholesterol levels were

measured using a cholesterol quantitation kit (Sigma Aldrich, MAK043) according to the manufacturers protocol.

Directly after blood collection, the mice were perfused with 10mL PBS (Westburg, LO BE17-515Q). The spleen was collected for flow cytometry. The aorta and heart were carefully removed and placed in 4% formol (VWR chemicals, 11699404) for 48h for histological analyses.

4.4. BMDM preparation

Three to five months old IRG1 WT or KO mice were sacrificed by CO_2 asphyxiation. For each mouse both femurs and tibias were extracted. The bones were cleaned for 1min in 70% ethanol followed by three washes in Dulbecco's Modified Eagle medium (DMEM; Thermo Fisher, A1443001) supplemented with 17mM glucose (Sigma Aldrich, G8769-100ML), 4mM glutamine (Thermo Fisher, 25030081) and 1mM Sodium Pyruvate (Sigma Aldrich, S8636-100ML). All four bones are then flushed with 10mL DMEM using a 24G needle. The obtained bone marrow is centrifuged for 10min at 300g at 4°C and resuspended in 2mL red blood cell lysis buffer for 5min. To stop the reaction, 5mL DMEM is added, and the cells are centrifuged. They are plated in 4 non-tissue culture treated petri dishes (Thermo Fisher Scientific) filled with 10mL differentiation medium composed of DMEM supplemented with 17mM glucose, 4mM glutamine, 1mM sodium pyruvate, 10% v/v foetal bovine serum (FBS, Thermo Fisher Scientific, 10270106), 100 U/mL penicillin, 100µg/mL streptomycin (Westburg, DE17-602E) and 20ng/mL recombinant mouse macrophage colony stimulating factor (rm M-CSF, Immunotools, 12343115). The cells differentiate during 6 days with a fresh medium supplementation at day 3 and are plated on day 6 in 12 well plates with $9x10^5$ cells per well. During the replating step, fresh differentiation medium is added, and the cells are left to adhere overnight. The BMDMs can then be stimulated for 24h in DMEM without M-CSF with 100ng/mL LPS (from E. coli O55:B5, Sigma Aldrich, L6529-1MG), 100ng/mL recombinant mouse IFNγ (Immunotools, 12343536), 20ng/mL recombinant mouse IL-4 (Immunotools, 12340043), 1mM itaconate (Sigma Aldrich, I29204) or 50µM 1400w (MedChemExpress,).

After 24h, the medium of LPS-IFNγ stimulated cells was collected and nitrite (NO_2^-), a stable breakdown product of NO, was measured with a Griess Reagent System Kit (Promega, G2930).

4.5. Flow Cytometry

4.5.1. Tissue preparation

Spleen: The spleen was grinded by squeezing it against a 70µm filter using a syringe plunger. The cells were then centrifuged 5min 400g at 4°C. The supernatant was aspirated

with a pump and the spleen homogenate was resuspended in 1mL red blood cell lysis buffer. After 5min, the cells were centrifuged, washed with 1mL FACS-Buffer to finally be resuspended in 500µL FACS buffer. In each flow cytometry tube, 50µL of the cell suspension was added.

Blood: In flow cytometry tubes, 50µl of whole blood was added with 1mL red blood cell lysis buffer. After 10min, the tubes were centrifuged 5min at 400g at 4°C and the cells were resuspended in 1mL PBS.

BMDMs: At day 6 of differentiation, $5x10^5$ cells are placed in flow cytometry tubes.

4.5.2. Staining

All cells are washed with 1mL PBS prior to the live/dead staining. The Zombie NIR (BMDM) and Zombie Red (immune cell profiling) are added to the cells for 30min in the dark at room temperature in a final volume of 100µl diluted in PBS (Table 2).

Protein	Supplier	Concentration
TruStain FcX (anti CD16/32)	Biolegend, 101319	1:500
Zombie NIR	Biolegend, 423105	1:400
Zombie Red	Biolegend, 423109	1:900

Table 2: List of Live/Dead dyes and Block solution

The cells are washed with FACS buffer and resuspended in 25µl TruStain block solution for 5min at room temperature in the dark. The primary antibody mix (Table 3) was added for 30min at 4°C. The cells were then fixed with 4% formol during 10min and were resuspended in FACS buffer to be acquired.

Antibody	Fluorochrome	Clone	Supplier	Host	Concentration
Purity assessment BMDMs					
CD11b	FITC	M1/70	BD	Rat	1:100
F4/80	PE	T45-2342	BD	Rat	1:100
Immune cell Profiling: Lymphoid Panel					
CD19	APC	1D3	BD	Rat	1:300
CD4	APC-Cy7	GK1.5	BD	Rat	1:900
CD44	BV605	IM7	BD	Rat	1:100
CD45.2	PE	104	BD	Mouse	1:50
CD49b	FITC	DX5	BD	Rat	1:150
CD62L	BV510	MEL-14	BD	Rat	1:450
CD8a	BV711	53-6.7	BD	Rat	1:900
TCRβ	PE-Cy7	H57-597	BD	Hamster	1:300

Table 3: List of Flow-Cytometry antibodies

4.5.3. Data acquisition and analysis

The BMDM purity assessment was measured with a FACSCanto II cell analyser (BD Biosciences) and the immune cell profiling was measured with a NovoCyte Quanteon flow cytometer (Agilent). The BD FACS Diva software (BMDM purity assessment) and the Agilent NovoExpress software (immune cell profiling) were used to record the data. For both cytometry experiments, doublets were eliminated by plotting the FSC-height and the FCS-area. The living cells were then selected. Fluorescence-Minus-One (FMO) controls were used to place the different fluorescent gates. The data was then processed with FlowJo (Version 10.4, TreeStar).

4.6. Histology

4.6.1. Tissue preparation

Aortic root: after fixation described in 4.3, the heart was placed in 15% w/v sucrose solution in PBS for 6h followed by a 30% w/v sucrose solution overnight. The tissue was then embedded in Tissue-Tek O.C.T Compound (Sakura, 4583) and snap frozen using isopentane and dry ice for cryosection. The embedded tissue was serially cut at 4µm on a cryostat (Leica CM1850 UV). Sections were placed on super frost slides to ensure adherence during staining protocols.

Aortic arch: After fixation, the aortic arch was dehydrated with a tissue processor (Leica TP1020) for paraffin embedding. The embedded tissue was serially cut at 3µm on a microtome.

4.6.2. Tissue staining

Oil-red-O staining:

The slides were incubated for 10min in an Oil-red-O solution (1,8mg/mL Oil-red-O Sigma, O0625-25G, in 60% v/v isopropanol, filtered before use). The slides were then rinsed in running tap water for 10min and counterstained with a hematoxylin solution acc. to Gill II (Carl Roth, T864.2) for 40 seconds. They were washed in running tap water and mounted with aqueous mounting medium.

Masson’s trichrome stain

The slides were incubated overnight in Bouin’s solution. They were washed in running tap water for 10min and stained in Weigert's Iron Hematoxylin solution for 7min (Hematoxylin 5mg/mL, Ferric chloride 5mg/mL in 50% ethanol and 0.5% Acetic Acid). The samples were then washed in running tap water and stained for 1min in a Biebrich Scarlet-Acid Fuchsin

solution (Biebrich Scarlet 9mg/mL, Acid Fuchsin 1mg/mL in 1% Acetic Acid). The slides are then placed for 30min in a Phosphomolybdic-Phosphotungstic solution (Phosphomolybdic acid, 12.5mg/mL, Phosphotungstic acid 12.5mg/mL). After, the slides are stained for 7min in aniline blue solution (Aniline Blue 25mg/mL in 4% acetic acid). The samples were then rinsed in 1% acetic acid solution for 4min. The slides were finally dehydrated and mounted with Entellan (Sigma Aldrich, 1079600500)

Hematoxylin and Eosin staining:
Paraffin-embedded sections were stained with hematoxylin and eosin (H&E). The staining was performed using a Ventana HE staining system (Roche).

4.6.3. En Face

The thoracic and abdominal aorta was prepared for the en face analysis. After fixation, the aorta was cut open from top to bottom. The adventitia was then carefully removed. During the entire process the aorta remained moist with regular PBS washes. The aorta was then washed in a 60% v/v isopropanol solution and stained with an Oil-red-O solution (3mg/mL in 60% isopropanol, filtered) for 15min. After, the aorta was washed in 60% isopropanol, shortly placed in dH_2O, and mounted with Kaiser's Glycerin Jelly (80mg/mL gelatine, Sigma G-1890, in 50% glycerol).

4.6.4. Microscopy

Pictures were taken with a Nikon Eclipse Ni microscope using the NIS-Elements software (Nikon). For each mouse 4 slices were analysed with 40µm intervals for the aortic root. For the aortic arch 3 slices were analysed with 36µm intervals between each other.
The plaque composition of the aortic arch was analysed as mentioned in Figure 7. Foam cells are stained with a light pink colour due to their high lipid content. The collagen rich area is composed of several cells and is stained with a slightly darker pink. Finally, cholesterol crystals form a crystal shaped "hole" in the tissue due to the dehydration process. Figures were analysed using ImageJ.

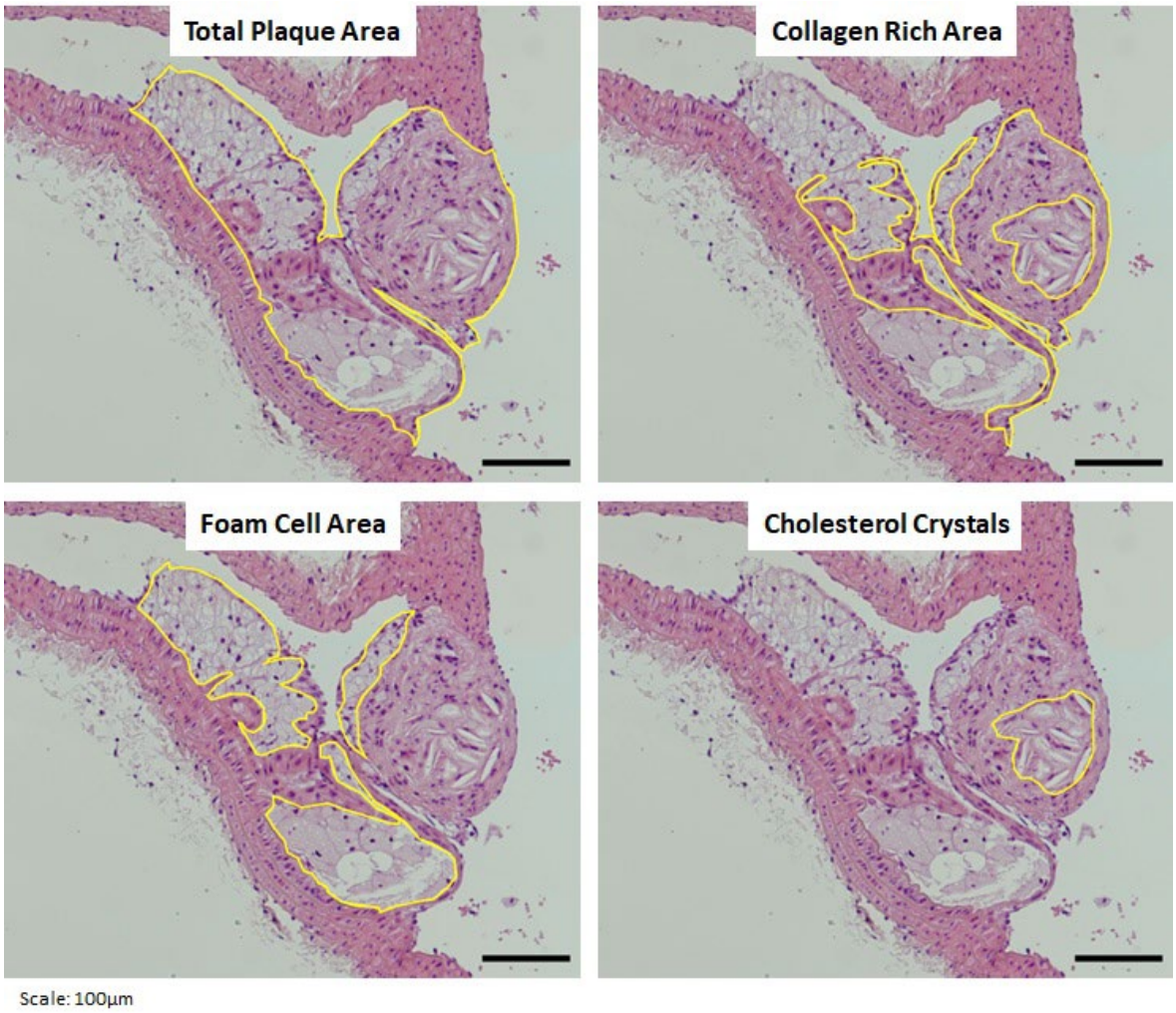

Figure 7. Plaque composition analysis of the aortic arch.

H&E staining of a plaque in the aortic arch. For each section the plaque area was measured (up left), as well as the collagen rich area (up right), foam cell area (down left) and other sections such as the cholesterol crystals (down right). In each panel the region of interest is marked by a yellow line. Scale bar: 100µm.

4.7. Metabolomics

4.7.1. Stable isotope tracing

For stable isotope experiment DMEM without glucose, glutamine and phenol red was supplement with 17mM Glucose, 4mM glutamine, 1mM sodium pyruvate, 10% FBS and 1% penicillin streptomycin. Depending on the experiment glucose was either replaced with D-Glucose [U-^{13}C6] 99% (Eurisotop, CLM-1396-1) or D-Glucose [4-D] 98% (Cambridge Isotope laboratories, inc. DLM-9294-PK). Glutamine was replaced with L-Glutamine [U-^{13}C5] 99% (Eurisotop, CLM-1822-H-0.25), L-Glutamine [Alpha-^{15}N] 98% (Eurisotop, NLM-1016-0.5) or L-Glutamine [Amide-^{15}N] 98%+ (Eurisotop, NLM-557-0.5).

Each condition was run in duplicates with 800µL tracing medium for $9x10^5$ BMDMs per well. The cells were then stimulated for 24h as described in 4.4. For the D-Glucose [4-D] tracing experiment cells were stimulated for 24h, and the tracer was added during the 4 last hours of the experiments.

4.7.2. GC-MS

The following method is adapted from Delbrouck et al., 2023 . To extract the metabolites, BMDMs were quickly washed with a cold 0.9% sodium chloride solution. Subsequently, 400µL ice-cold GC-MS extraction buffer (composed of 50 % MeOH (Carl Roth: KK44.1), 50% Milli-Q H_2O with 1µg/mL pentanedioc-d6 acid, 1µg/mL [U-13C]-ribitol and 5µg/mL tridecanoid-d25 acid as internal standards) was added to each well. After 5 minutes of incubation at 4°C on a rocking shaker, the supernatant was collected into Eppendorf tubes containing 200µL of ice-cold chloroform (Sigma-Aldrich: 154733). The tubes are then centrifuged for 10min at 13000g at 4°C. This leads to the separation of the solution into two phases: the upper phase which is the polar phase and the lower phase which is the non-polar phase. The inserts of GC vials were filled with 250 µL of the polar phase. The vials were then dried at -4°C in a vacuum drier and were ready to be measured. The plates in which the BMDMs were cultured, were kept for protein measurements (Lowry-Assay).

The samples were measured at the metabolomic platform of the Luxembourg Center of System Biomedicine. The polar metabolites underwent derivatization for 90 minutes at 55°C using 20µL of methoxyamine (20mg/mL) dissolved in pyridine with continuous shaking. Subsequently, they were subjected to an additional 60min derivatization at 55°C with 20µL of N-tert-Butyldimethylsilyl-N-methyltrifluoroacetamide (MTBSTFA) containing 1% tert-butyldimethylchlorosilane (TBDMCS). The GC-MS analysis was conducted using an Agilent 7890B GC coupled with an Agilent 5977A Mass Selective Detector (Agilent Technologies). A sample of 1µL was injected into a Split/Splitless inlet, operating in splitless mode at 270°C. The gas chromatograph was equipped with a 30m (I.D. 250µm, film 0.25µm) ZB-35MS capillary column with a 5m guard column (Phenomenex). Helium served as the carrier gas with a constant flow rate of 1.2mL/min. The GC oven temperature started at 100°C for 2min, then ramped up to 300°C at a rate of 10°C/min, and finally held at 300°C for 4min. The total runtime lasted 26min. The transfer line temperature was set at 280°C. The mass selective detector (MSD) operated under electron ionization at 70eV. The MS source was maintained at 230°C, and the quadrupole at 150°C. For accurate MID quantification, measurements were conducted in selected ion monitoring mode. To analyse the GC-MS data including metabolite quantification, natural-isotope correction, MID calculation, the MetaboliteDetector software package (Version 3.2.20180913) was used.

4.7.3. LC-MS

The following method is adapted from Delbrouck et al., 2023. To extract the metabolites, BMDMs were quickly washed with cold PBS. Subsequently, 300µL ice-cold LC-MS extraction buffer (composed of 50% Methanol (Carl Roth: KK44.1), 30% acetonitrile (Carl Roth: AE70.1), 20% Milli-Q H_2O containing 1µg/mL of each internal standard: IS-AMP, IS-CPR, IS-CPA, IS-TFL, and IS-TNAD) were added into each well. After 5min incubation at 4°C on a rocking shaker, the extraction solution was placed into Eppendorf tubes. The tubes were then centrifuged for 10min at 13000g at 4°C and 100µL of the supernatant was transferred into an LC-MS vial with insert. The plates in which the BMDMs were cultured, were kept for protein measurements (Lowry-Assay).

The LC-MS measurements were performed at the metabolomic platform of the Luxembourg Institute of Health. The LC-MS setup is composed of a Vanquish Flex (Thermo Fisher Scientific) LC system configured with a binary gradient and coupled to a Q-Exactive Plus mass spectrometer (Thermo Fisher Scientific). The analytical column, a SeQuant ZIC-pHILIC (Merck) (2.1mm × 150mm, 5µm), was accompanied by a guard column (2.1mm × 20mm) and maintained at 45°C in the column oven. Solvent A consisted of 20mM ammonium carbonate at pH 9.2 with 5µM of medronic acid, while solvent B was pure acetonitrile. Samples were injected onto the column and subjected to a linear gradient elution, transitioning from 80% B to 20% B over 15min at a constant flow rate of 200µL/min. The MS acquisition involved a polarity switch between positive and negative electrospray ionization modes. Full MS spectra were acquired in the range of 75 to 1000 m/z at a resolution of 70000 (at 200m/z), with automatic gain control set to 1e6 charges and a maximum ion trap fill set to 250ms. To analyse the LC-MS data the TraceFinder software (Thermo Fisher Scientific) was used. The natural isotope correction was performed with the application Metabolite Autoplotter (Pietzke and Vazquez, 2020)

4.7.4. Lowry Assay

To normalize the intracellular metabolite levels, the protein amount of each well was measured with a lowry assay. The dried plates from the metabolite extraction are kept at 4°C until the assay is performed. 300µL of a solution made of 0.5% sodium deoxycholate and 1M sodium hydroxide was added to each well. After 40min at room temperature, 3mL of a solution made of 250mg/L sodium copper EDTA, 20g/L sodium carbonate and 4g/L sodium hydroxide was added. After 10min at room temperature, 300µL of Folin Ciocalteu's phenol (Sigma Aldrich, F9252-500ML) were added to each well for 40min at room temperature. The 12well plates were directly measured with a Clariostar (BGM Labtech) at 750nm.

4.8. RNA sequencing

Total RNA was extracted using NucleoZOL (Macherey-Nagel, 740404.200) and the NucleoSpin RNA Set for NucleoZOL kit (Macherey-Nagel, 740406.50) according to the manufacturers protocol. RNA integrity and quantity were determined using the Agilent 2100 Bioanalyzer. An RNA integrity number above 9 was accepted for downstream analysis. To prepare the library the Illumina Stranded mRNA prep ligation kit (Illumina, 20040532) was used, following the manufacturers instruction. The libraries have been pooled and sequenced on an Illumina NovaSeq 6000 system (Illumina).

After initial QCs using FastQC (https://www.bioinformatics.babraham.ac.uk/projects/fastqc/) and FastQ Screen (https://www.bioinformatics.babraham.ac.uk/projects/fastq_screen/), fastq files were processed using a local Snakemake workflow including the following main steps. First, raw reads were trimmed from their UMI index, poly A and adapter sequences using a combination of dedicated scripts and cutadapt (v2.10). Next, filtered reads were submitted for mapping (STAR v2.5.3a) on the Mouse Reference genomes (GRC38). Collapsing of reads originating from the same fragment was achieved with umi_tools (v 1.0.0) and counting was performed with featureCounts (subread v2.0.0).

Differential expression of genes (DEG) was assessed using the DESeq2 package (v1.36) and FDR < 0.05 and a fold change cut-off of 1.5 were imposed. DEG were analysed with the METASCAPE tool (https://metascape.org/, July 2022) for ontology analysis. For ranked-gene set enrichment analysis (GSEA Desktop v4.2.3 July 2022, Broad Institute, MA), all genes were ranked based on fold change and tested against the HALLMARK, REACTOME, and GOBP gene sets.

4.9. Transwell migration/invasion assay

The following method is adapted from Delbrouck et al., 2023. Migration and invasion were determined using transwell chambers with 8µm pore size (Greiner Bio-one, 662638). Migration was assessed on chambers without coating while invasion was determined on chambers coated with 0.5mg/mL ECM (Sigma Aldrich, E1270) and 0.05mg/mL collagen type I (Sigma Aldrich, A1048301) for at least 2h at 37°C. At day 6 of BMDM differentiation, $1.5x10^5$ cells in 300µL DMEM with LPS and/or IFNγ are placed in the upper transwell chamber. The lower part of the chamber was filled with 750µL of DMEM supplemented with either 50µg/mL oxLDL (Thermo Fisher, L34357), 100ng/mL CCL2 (Immunotools, 12343383), or 100ng/mL CCL11 (Immunotools, 12343213). After 72h, the cells were fixed with 4% formol for 15min and stained for 15min with 0.05% of crystal violet solution (Sigma-Aldrich: HT90132). BMDMs that could not migrate were removed from the top of the chamber using a cotton tip. For each transwell, 5 pictures were taken with a Leica inverted microscope at 20x magnification. The cells were counted using a Python script written by

the AI department of the Helmholtz Institute München. The script automatically counts the crystal violet stained cells and gives the opportunity to correct every picture manually. The Python code and the full description of the tool can be publicly accessed on GitHub. Ruolin Shen, Christina Bukas, & Marie Piraud. (2022). HelmholtzAI-Consultants-Munich/Automatic-Cell-Counter: First version of the software (v1.0.0). Zenodo. https://doi.org/10.5281/zenodo.6390980

4.10. Translation Assay

BMDMs were differentiated and treated as described in 4.4 for 24h. The translation assay was done using the O-propargyl-puromycin (OPP) Click-iT™ Kit (Thermo Fisher Scientific, C10456) adapted for a flow cytometry readout. The OPP was added to the BMDMs at a concentration of 20µM in fully supplemented DMEM, for 30min. The cells were placed at 37°C with 5% CO_2 during this time. The cells were then stained with Zombie NIR (1:500 in PBS) and incubated during 30min at 4°C. After this step, BMDMs were fixed using 4% paraformaldehyde (PFA) without methanol for 15min and were transferred in a 96 well U-bottom plate. The cells were then permeabilized with a 0.5% Triton X100 solution for 15min. After 2 washing steps, 25µL of the Click-iT™ cocktail were added to the cells for 30min at room temperature an in the dark. Finally, the cells were washed and resuspended in 100µL FACS buffer and acquired with a NovoCyte Quanteon flow cytometer (Agilent). The data was analysed with FlowJo (Version 10.4, TreeStar).

4.11. Cholesterol Influx Assay

BMDMs were differentiated as described in 4.4. After differentiation they were stimulated with LPS-IFNγ and 20µg/mL DiI conjugated oxLDL (Thermo Fisher Scientific, L34358) for 24h. The cells were then washed with PBS and stained with Zombie NIR (1:500 in PBS) and incubated during 30min at 4°C. After this step, BMDMs were fixed using 4% paraformaldehyde (PFA) without methanol for 15min and were transferred in a 96 well U-bottom plate. Finally, the cells were washed and resuspended in 100µL FACS buffer and acquired with a NovoCyte Quanteon flow cytometer (Agilent). The data was analysed with FlowJo (Version 10.4, TreeStar).

4.12. Western Blot

Protein expression was assessed by Western Blot. BMDMs were stimulated for 24 hours as described in 4.4. The cells were detached from the plate with accutase solution (Sigma Aldrich, A6964-100ML). They were then placed in an Eppendorf tube, washed with PBS, and pelleted before lysis. They were lysed with ice-cold cell lysis buffer made of 50mM Tris-HCl (Carl Roth: 0188.2) 1mM EDTA (Sigma-Aldrich: ED-100G), 150mM NaCl (Sigma-Aldrich: S3014), 1% IGEPAL® CA-630 (Sigma-Aldrich: I3021) containing Protease and

Phosphatase Inhibitors (Sigma-Aldrich: 490687001 & 4693124001)). Lysates were sonicated for 10min at 4°C in a water bath. The lysate was then centrifuged for 10min at 13000 g at 4°C. Protein concentration was assessed by Bradford assays.

20µg protein were placed in Laemmli sample buffer containing 2% SDS. 60mM Tris-Cl (pH6.8), 0.02% bromophenol blue (Merck) and 100mM dithiothreitol (DTT, Sigma-Aldrich: 10708984001). They were then denaturated at 70°C for 10min and loaded on RunBlue 4-12% Bis-Tris gels (GeneScript: M00656). The proteins were separated by molecular weight through an electrophoresis process with 150 Volt running for 1.5h in MOPS buffer (Lifetech, NP00001). After migration, proteins were blotted on a nitrocellulose membrane using wet transfer. They were transferred in transfer buffer (1% Tris-Glycine, 4% methanol) at 30 Volt for 1.5h. The membrane was blocked in 5% milk solution for 1h at room temperature and washed in 1X Tris-Buffered Saline (TBS), 0.1% Tween®-20 detergent solution (TBS-T). Primary antibodies were incubated overnight at 4°C in a 1% Bovine serum albumin (BSA, Sigma Aldrich, A7030-50G) solution in TBS-T at a concentration mentioned in Table 4. The membrane was then washed with TBS-T and incubated with the secondary antibody diluted in 1% BSA in TBS-T for 1h at room temperature. Imaging was performed using the Odyssey CLx Imaging System (LI-COR) and images were analysed using the ImageStudioLite Software Vers.5.2 (LI-COR).

Antibody	Supplier	Host	Concentration
Anti-IRG1	Abcam, ab222411	Rabbit	1:1000
Anti-GAPDH	Cell Signaling #5174	Rabbit	1:1000
Anti-Rabbit IgG (H+L)	LI-COR IRDye 680RD	Donkey	1:10000

Table 4: List of primary and secondary antibodies

4.13. Statistical analysis

Statistical differences were analyzed either with a 2way ANOVA followed by Sidak's multiple comparison test, or with the Mann Whitney U test, or with a paired or unpaired two-tailed Student t-test in GraphPad Prism v9.0.1. Data are shown as mean ± standard deviation (SD).

5. RESULTS

5.1. The role of Itaconate in Macrophage Metabolism

5.1.1. Model validation

To understand the role of itaconate in macrophages, experiments were conducted with BMDMs. To define the best differentiation protocol yielding highest purity, three differentiation methods were compared. Bone marrow cells were isolated and differentiated for 7 days in DMEM medium that was supplemented with either 20ng/mL M-CSF, 10% L929 medium, or 10% CMG14-12 medium. The CMG14-12 cell line originates from the Ltk- cell line and was modified to produce murine M-CSF (Takeshita et al., 2000). After 7 days, the macrophage population purity was assessed with flow cytometry by targeting CD11b F4/80 double positive cells (Figure 8). Bone Marrow that differentiated with M-CSF presented 93,4% double positive cells while bone marrow cells that differentiated with L929 or CMG14-12 medium presented a lower purity (84% and 74,9% respectively). Consequently, all subsequent experiments involving BMDMs in this thesis were differentiated with M-CSF.

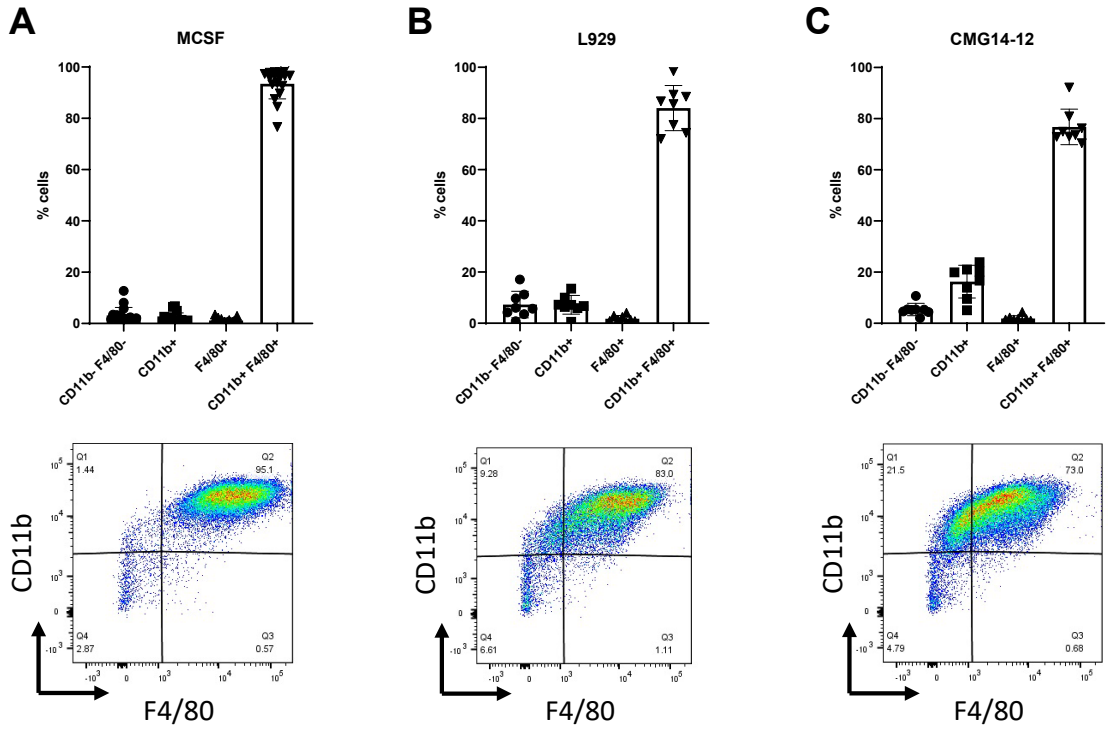

Figure 8. M-CSF differentiation yields highest BMDM purity.

Bone marrow was differentiated during 7 days with M-CSF (A), L929 medium (B), or CMG12-14 medium (C). The percentage of CD11b F4/80 positive populations were gated amongst living cells. The quantification for each mouse is represented

in the upper histogram while a representative flow cytometry plot is shown below each panel.

After having validated the best differentiation protocol we wanted to confirm the IRG1 status in WT and KO mice. As IRG1 is mostly expressed under pro-inflammatory condition, cells were treated with LPS and/or IFNγ. As control for anti-inflammatory conditions cells were treated with IL4. To validate that BMDMs from IRG1 KO mice do not induce IRG1 upon stimulation, protein abundance was monitored by Western Blot. The absence of the IRG1 band in KO BMDMs treated with LPS and IFNγ confirms that macrophages from KO mice are unable to express IRG1 under pro-inflammatory conditions (Figure 9). The absence of band in WT cells treated with IL4 further confirms that IRG1 is not expressed under anti-inflammatory conditions. Interestingly no band appeared in IFNγ stimulated WT BMDMs indicating that IFNγ alone might not induce IRG1 expression or that the amount of produced IRG1 is below the detection limit of the antibody. Interestingly dual stimulation resulted in enhanced IRG1 expression.

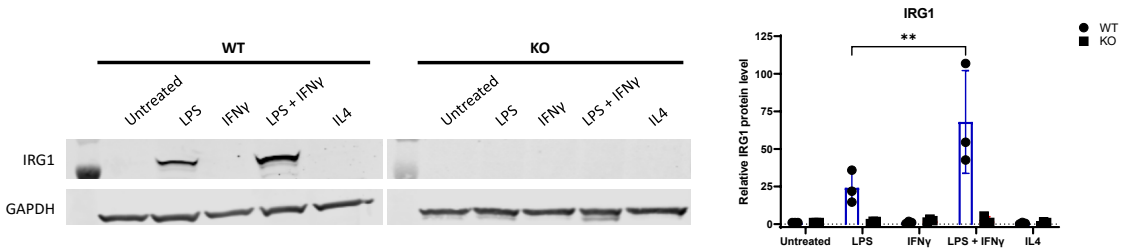

Figure 9. IRG1 KO mice do not express IRG1.

Normalised protein levels from cell lysates of unstimulated, IL4, LPS and/or IFNγ stimulated BMDMs from IRG1 WT and IRG1 KO mice. The cells were stimulated for 6h. Samples were immunoblotted against IRG1 and GAPDH. Representative blot (left), quantification (right). WT=3, KO=3 ;**P<0.01by ordinary two-way ANOVA with Sidak's multiple comparison test.

5.1.2. LPS-IFNγ stimulation reduces the relative glucose flux.

Itaconate is derived from the metabolite Cis-Aconitate, which is part of the TCA cycle. Since glucose is a major fuel of the TCA cycle, the relative flux of glucose within the cycle was investigated. To track the movement of glucose molecules within cells, stable isotope tracing was employed using fully labelled ^{13}C glucose ([U-^{13}C]Glc). The glucose molecule enters the TCA cycle through Acetyl-CoA, which is derived from pyruvate, a product of glycolysis. The two ^{13}C atoms of Acetyl-CoA can then enter the TCA cycle by combining with Oxaloacetate to form Citrate (Figure 10, A). Consequently, two out of the six carbon atoms in Citrate are ^{13}C-labelled which can be measured using Mass Spectrometry.

Accordingly, the labelled carbons cause a mass shift of 2 Dalton, (Citrate M+2). If the cycle proceeds in a classic manner, all metabolites following Citrate in the TCA cycle will continue to contain two ^{13}C atoms.

To compare the impact of different stimulation we analysed the relative glucose flux by comparing single LPS or IFNγ treatment with dual stimulation. LPS stimulation resulted in 30% Citrate M+2 enrichment in WT BMDMs while 20% Malate M+2 was detected representing 10% of labelling loss (Figure 10, B). The labelling pattern observed after IFNγ stimulation is similar to the one observed after LPS stimulation. In contrast the LPS-IFNγ double stimulation resulted in 25% labelling loss from Citrate M+2 to Malate M+2 indicating that the relative glucose flux was reduced in WT BMDMs that were stimulated with LPS-IFNγ for 24h.

In IRG1 KO BMDMs stimulated with LPS, 25% Citrate M+2 and 10% Malate M+2 was detected resulting in 15% labelling loss (Figure 10, C). IFNγ stimulated KO cells showed 5% labelling loss while double stimulated cells showed 10% labelling loss. Albeit the percentage of Citrate M+2 was around 25 to 30% in the 3 different stimuli in WT BMDMs, it was slightly lower in KO BMDMs especially in cells stimulated with LPS-IFNγ.

Overall, the results indicate that the relative contribution of glucose to fuel the TCA cycle is reduced in double stimulated BMDMs of KO and WT mice.

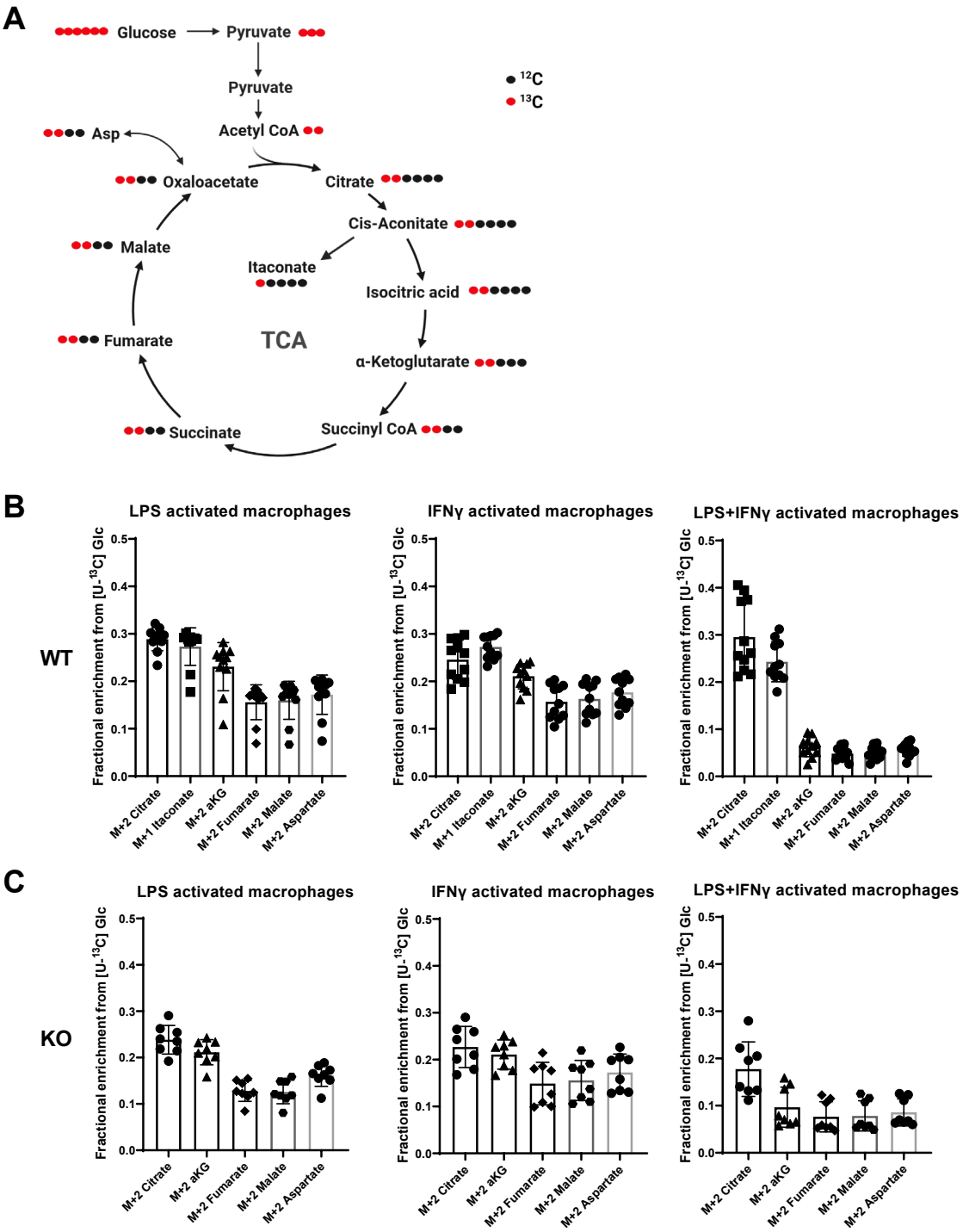

Figure 10. IFNγ LPS double stimulation reduces the relative glucose flux in the TCA cycle.

A, Scheme representing the stable isotope tracing of a fully labelled ^{13}C glucose molecule within the TCA cycle. Black dots represent ^{12}C atoms and red dots represent ^{13}C atoms. **B, C**, Fractional enrichment from ^{13}C glucose in LPS, IFNγ and double stimulated BMDMs of WT (B) and KO (C) mice. Cells were stimulated and traced for 24h. WT=11, KO=8 from two independent experiments.

5.1.3. IRG1 loss reduces citrate malate shuttle in double stimulated cells.

To understand the labelling loss from ^{13}C glucose between the different stimuli and between genotypes, we calculated the ratio of Malate M+2 to Citrate M+2 (Figure 11, A).
A ratio of 1 would indicate that all citrate molecules become malate molecules via the canonical TCA cycle. However, citrate can be exported into the cytosol and become oxaloacetate releasing Acetyl-CoA and therefore losing the two ^{13}C atoms from glucose. Oxaloacetate can convert into malate which can enter the mitochondria resulting in an unlabelled malate molecule in the TCA cycle. This metabolic process is known as citrate-malate shuttle (or non-canonical TCA cycle).
The ratio malate M+2 citrate M+2 was close to 0.6 in untreated and single treated LPS, IFNγ WT BMDMs. This ratio decreased to 0.2 in double stimulated WT cells. Interestingly the ratio in KO BMDMs was similar to WT BMDMs in the untreated and single treated conditions. In the double condition however, the ratio was 0.4 which is lower compared to the other stimuli from the same genotype but doubled when compared to WT double treated BMDMs.
The results indicate that in untreated or single treated BMDMs, more than half of the glucose generated citrate becomes malate through the TCA cycle. However, in double treated cells the proportion of exported citrate increases, especially in WT BMDMs.

To confirm the previous observation, we used a glucose tracer in which the hydrogen linked to the 4th Carbon is a deuterium atom (D-[4-^{2}H]glucose). When glyceraldehyde-3-phosphate is converted into 1,3-Bisphosphoglycerate, NAD^+ is converted into NADH and will inherit the deuterium atom. The NADH can transmit its newly acquired deuterium atom to malate during the cytosolic conversion of oxaloacetate to malate. When malate enters the TCA cycle it can either directly be converted in oxaloacetate or it can become fumarate. If the 1st option takes place the deuterium atom will be incorporated into NADH, if the 2nd option takes place fumarate will be labelled (M+1) due to the deuterium. As fumarate is a symmetrical molecule, the deuterium can be associated to the carbon number 2 or 3 and when fumarate converts back into malate, the deuterium can either be on carbon 2 or 3 resulting into two options. Either the deuterium will go into NADH during the malate oxaloacetate conversion, or it will be incorporated in citrate resulting in a citrate M+1 labelling (Figure 11, B).
WT BMDMs had 0.5% labelled citrate M+1 when stimulated with LPS only while they presented 4.4% labelling when stimulated with LPS-IFNγ. KO BMDMs presented a reduced labelling compared to WT: 0.1% labelling when stimulated with LPS only and 2% after double stimulation. These results indicate that increased amounts of citrate are exported to

the cytosol when BMDMs are exposed to LPS and IFNγ and that IRG1 loss reduces the citrate export by half.

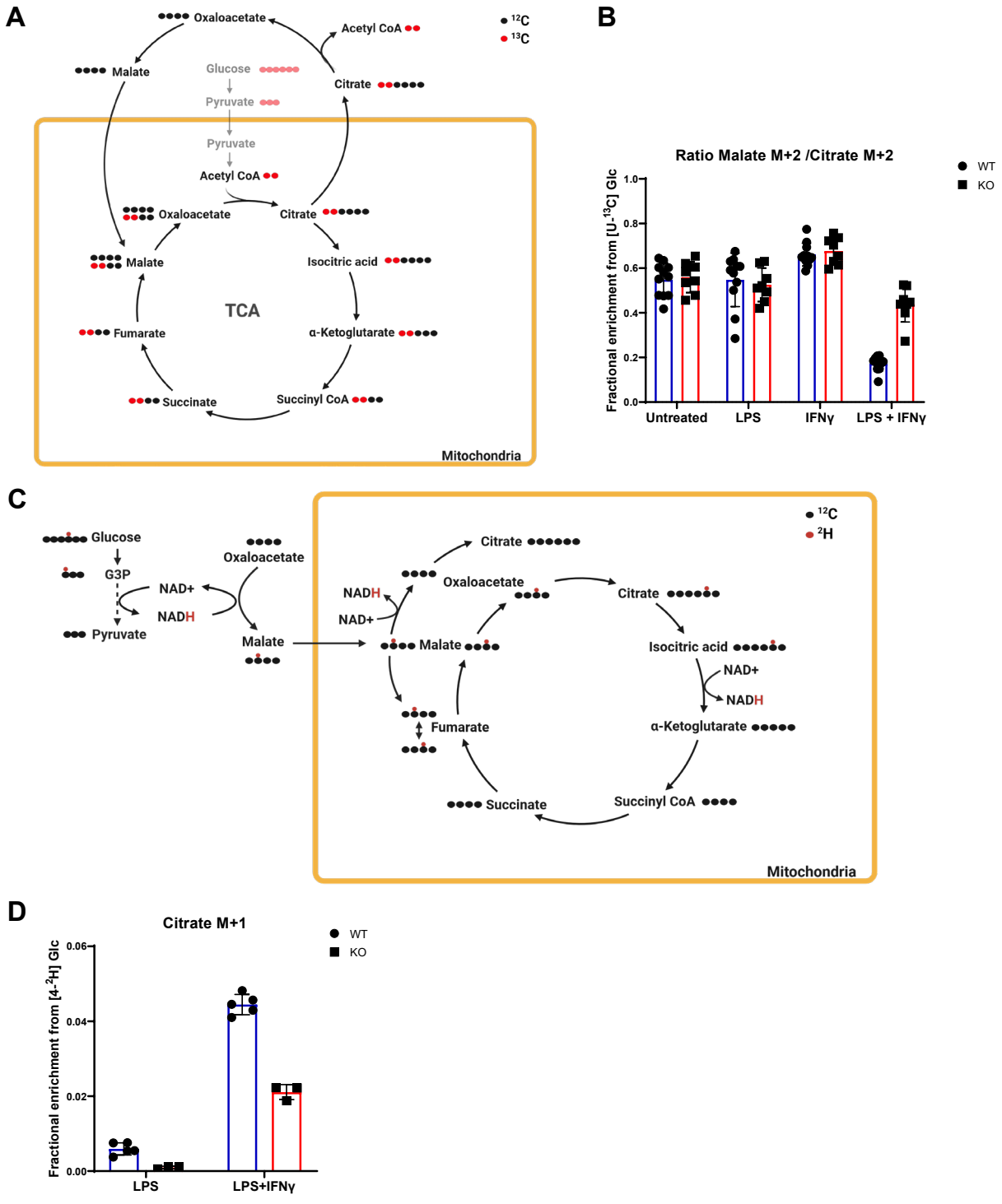

Figure 11. The Citrate Malate shuttle is more active in double stimulated WT BMDMs.

A, Schematic representation of stable isotope tracing of a fully labelled ^{13}C glucose molecule indicating how the ^{13}C carbons can leave the TCA cycle resulting in a

labelled citrate M+2 but an unlabelled malate. Black dots represent ^{12}C atoms and red dots represent ^{13}C atoms. **B,** Ratio of Malate M+2 on Citrate M+2 derived from ^{13}C glucose of untreated, LPS, IFNγ and double stimulated BMDMs of WT and KO mice. Cells were stimulated and traced for 24h. WT=11, KO=8 from two independent experiments. **C**, Schematic representation of stable isotope tracing of [4-^{2}H] glucose. During glycolysis deuterium is transferred to NADH and can be later transmitted to malate. After entering the mitochondria malate can become fumarate inducing a potential switch of the deuterium atom from carbon 2 to carbon 3. Consequently, citrate can be labelled M+1. Black dots represent ^{12}C atoms and red dots represent ^{2}H atoms. **D,** Fractional enrichment of Citrate M+1 from [4-^{2}H] glucose from BMDMs treated with LPS alone or LPS with IFNγ of WT or KO mice. The cells were treated for 24h and the tracer was added 3h before harvesting the cells. WT=5 KO=3 from one experiment.

5.1.4. Itaconate has amplified effects on metabolite levels of LPS-IFNγ double stimulated macrophages.

Cordes and colleagues as well as Lampropoulou and colleagues have already demonstrated that itaconate inhibits the succinate dehydrogenase and therefore has an impact on succinate levels as well as other TCA cycle metabolites when macrophages are stimulated with LPS (Cordes et al., 2016; Lampropoulou et al., 2016). The glucose stable isotope tracing described in previous sections demonstrated differences between genotypes especially after LPS-IFNγ stimulation. As the reduced labelling from glucose could be linked to metabolite level changes, the levels of TCA cycle metabolites were investigated in BMDMs after LPS and/or IFNγ stimulation.

As expected, the itaconate levels in WT cells were increased when stimulated with LPS only compared to IFNγ single stimulated cells. Interestingly, they are decreased in LPS-IFNγ double stimulated cells despite early increased IRG1 protein levels (Figure 12 and 8). The succinate levels mirror the itaconate levels, rising in stimulated WT BMDMs while staying low in KO cells except in unstimulated cells where they remain middle range. The results show that IFNγ stimulated cells do also produce itaconate and that the LPS addition does not raise itaconate levels to single LPS stimulated cells which is reflected in succinate levels. This suggests that the presence of IFNγ may act as a negative feedback regulator to control intracellular itaconate levels.

Citrate levels remain steady in unstimulated and single stimulated cells regardless of the genotype. However, in double stimulated KO cells the levels are significantly reduced compared to WT cells. On the contrary, aKG levels are substantially increased in KO BMDMs in response to LPS and LPS-IFNγ double stimulation. Without stimulation or following IFNγ stimulation, levels remain low and comparable between WT and KO. The results can indicate that KO macrophages produce more aKG or that they are not able to

use the metabolite as efficiently as WT cells after LPS stimulation with or without IFNγ addition.

The SDH inhibition caused by itaconate leading to succinate accumulation could lead to reduced Fumarate or Malate levels in WT cells. However, both metabolite levels remain steady in unstimulated and IFNγ single stimulated cells regardless of the genotype. Following LPS stimulation KO cells show slightly increased levels although WT levels are unchanged in comparison to other stimulations. Additionally, after LPS-IFNγ stimulation, fumarate and malate levels are significantly higher in KO cells compared WT cells. The levels of metabolites following succinate in the TCA cycle remain constant in WT cells despite the presence of SDH inhibition, however, KO cells exhibit greater levels after LPS-IFNγ double stimulation.

Overall, the results indicate that itaconate plays an increased role in macrophages after LPS-IFNγ double stimulation.

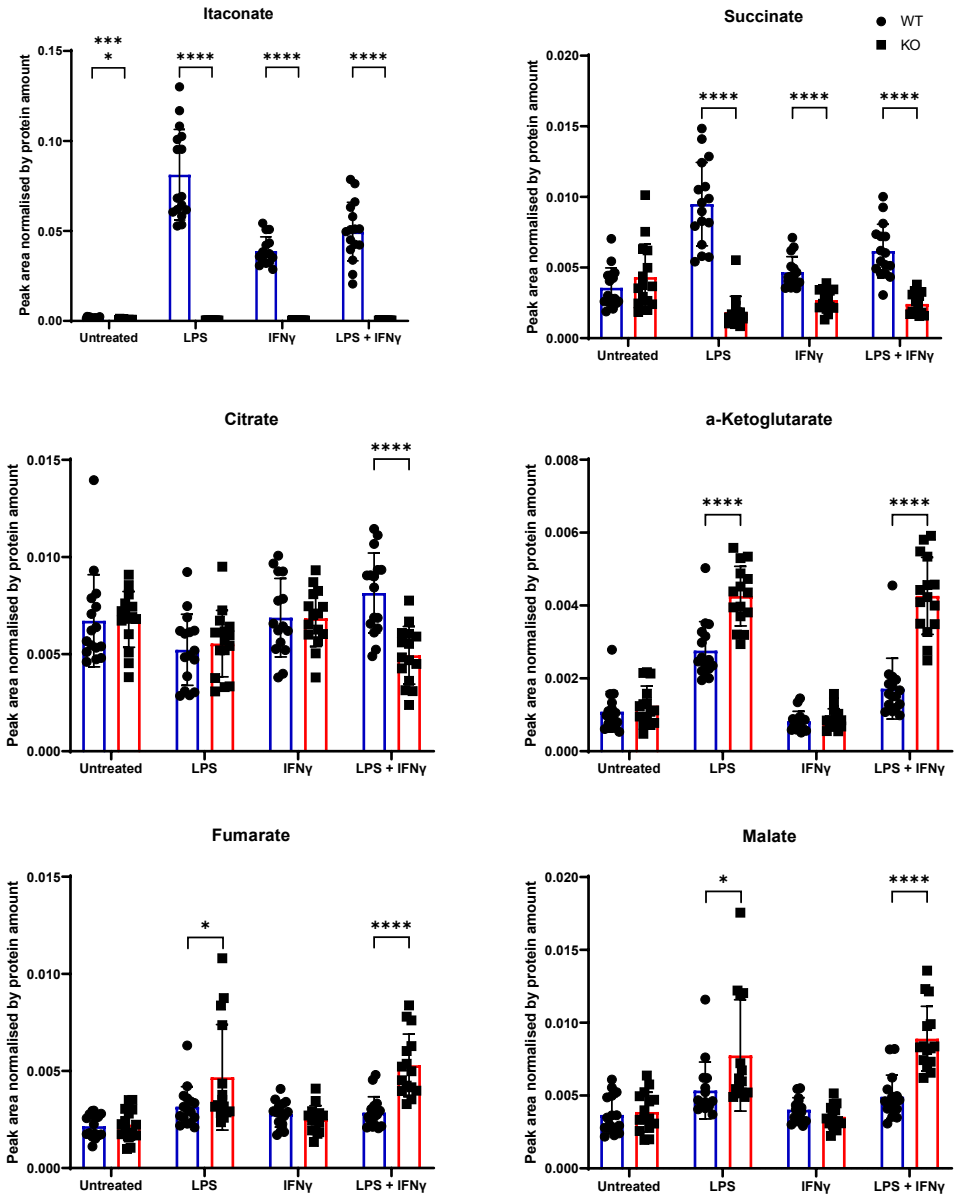

Figure 12. Itaconate loss modifies TCA cycle metabolite levels of double stimulated BMDMs.

Relative TCA cycle metabolite levels of WT (blue) and KO (red) BMDMs after 24h LPS and/or IFNγ stimulation. The peak area is normalised by one internal standard and by protein amount. *P<0.05,****P<0.0001 by two tailed unpaired t-test. WT: n=16 KO: n=15 from three independent experiments

5.1.5. Glutamine is a major TCA cycle fuel in LPS-IFNγ double stimulated BMDMs.

The section 5.1.2 of the thesis shows a decreased labelling from glucose in the TCA cycle and the section 5.1.4 demonstrates that the relative levels do not mirror the glucose labelling, indicating that the TCA cycle uses another fuel.

The relative glutamine flux within the TCA cycle was therefore investigated using fully labelled ^{13}C glutamine. Glutamine can enter the TCA cycle via aKG. In case of direct contribution, all five atoms of aKG are labelled (aKG M+5). Subsequently, the following metabolites also have all their carbons labelled until citrate, where the addition of Acetyl-CoA gives two unlabelled carbons resulting in citrate M+4 (Figure 13, A).

After LPS stimulation 20% aKG M+5 was detected in WT BMDMs. This fractional enrichment remained steady through fumarate M+4 and malate M+4 and slightly decreased to 14% Citrate M+4 (Figure 13, B). The labelling pattern observed after IFNγ stimulation is comparable to the one observed after LPS stimulation. However, after LPS-IFNγ double stimulation, 50% aKG was fully labelled indicating that half of the aKG comes from glutamine. The percentage of following M+4 labelled metabolites decreased to 35-40%.

LPS activated KO BMDMs presented 20% aKG M+5, 13% malate M+4 and 9% Citrate M+4, reducing the initial labelling by 11% (Figure 13, C). After IFNγ stimulation the labelling slightly decreased from 15% aKG M+5 to 10% Citrate M+4. In both stimulation the percentage of Citrate M+4 was similar while the percentage of aKG M+5 was slightly decreased in IFNγ showing a higher loss of labelling in LPS stimulated cells. Double stimulated cells have a doubled proportion of labelled aKG M+5 compared to single LPS stimulated BMDMs. The labelling then decreased to 34% Malate M+4, to finally reach 19% Citrate M+4. This represents a difference of 21% labelling between the glutamine entry point of the TCA cycle and later metabolites.

The labelling between WT and KO BMDMs is similar after single LPS and single IFNγ stimulation. However, it is 10% lower in KO BMDMs after double stimulation in all metabolites except citrate where it is 20% lower.

Overall, the results indicate that the relative contribution of glutamine to fuel the TCA cycle is increased in double stimulated BMDMs of KO and WT mice. Moreover, while single perturbation does not reveal any difference between WT an KO double perturbation results in lower enrichment in KO cells.

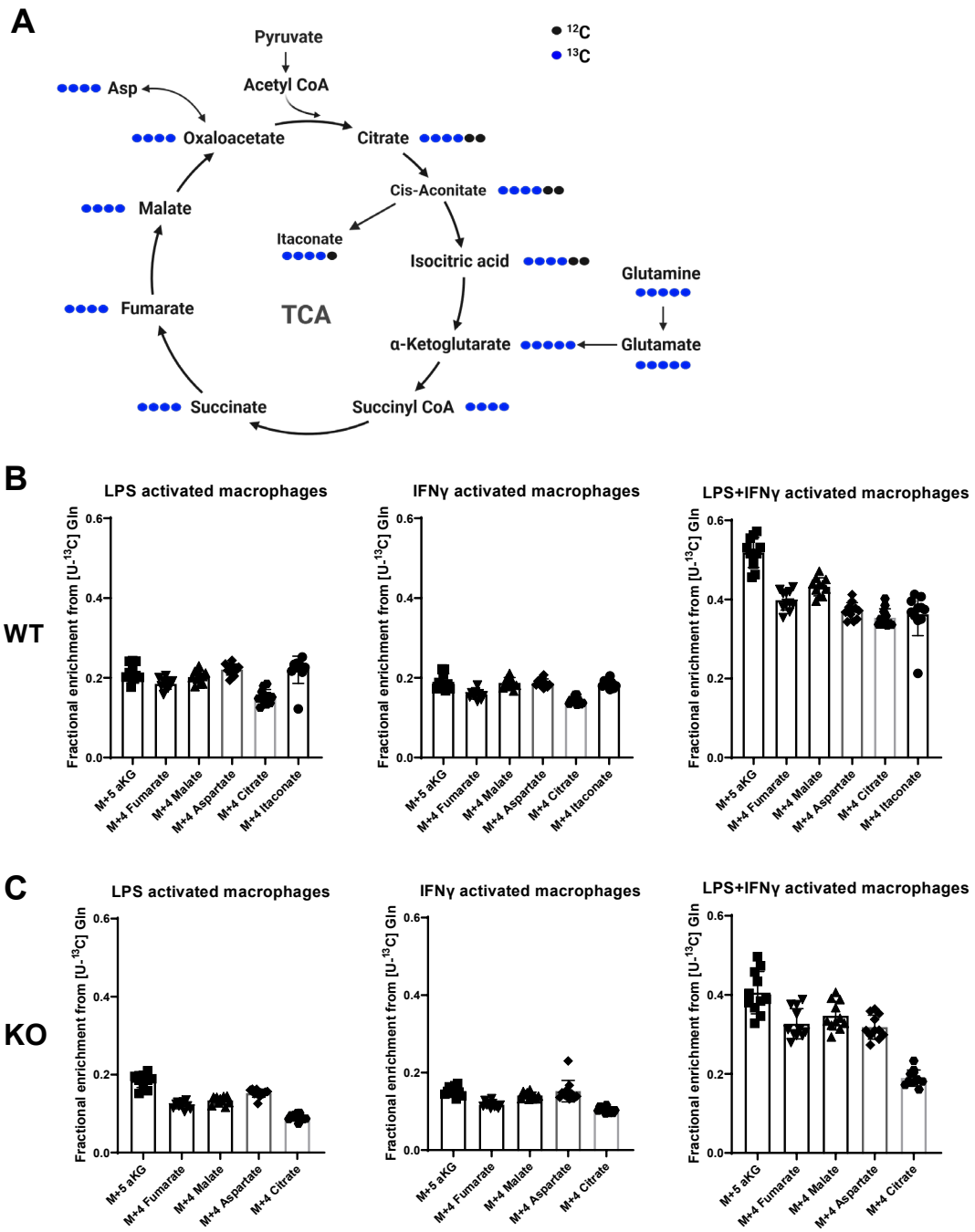

Figure 13. The relative glutamine flux is increased in LPS-IFNγ double stimulated BMDMs.

A, Schematic representation of the stable isotope tracing of a fully labelled ^{13}C glutamine molecule within the TCA cycle. Glutamine enters the cycle via aKG by first becoming glutamate. All following metabolites are fully labelled until Citrate where Acetyl-CoA give two unlabelled carbons. Black dots represent ^{12}C atoms and blue dots represent ^{13}C atoms. **B, C**, Fractional enrichment from ^{13}C glutamine in LPS, IFNγ and double stimulated BMDMs of WT (B) and KO (C) mice. Cells were stimulated and traced for 24h. WT=8, KO=11 from two independent experiments.

5.1.6. The reductive TCA cycle is active in IRG1 KO double stimulated BMDMs.

In section 5.1.4, an increased labelling loss in Citrate M+4 has been described in KO cells stimulated with LPS-IFNγ. To investigate this loss, the total ^{13}C contribution to Citrate (comprising M+0 to M+6) has been determined.

The TCA cycle usually turns in an oxidative way from Citrate to aKG, to succinate continuing to malate etc. However, several steps in the TCA cycle are reversible: within the mitochondria 6 out of 8 steps. By using fully labelled ^{13}C glutamine the reversed step from aKG to Citrate can be analysed by monitoring M+5 labelled citrate (reductive route) versus M+4 labelled citrate (oxidative route) (Figure 14, A).

The fractional enrichment of Citrate M+5 was very low in untreated and single IFNγ treated cells (1%) indicating that under both conditions, the reductive carboxylation of aKG is only minor (Figure 14, B). In LPS treated cells the labelling was slightly higher reaching 2.7% in WT and 3.7% KO. However, it reached 8.8% in double stimulated KO cells while it reached 1.9% in WT BMDMs representing 6.9% difference between genotypes.

The findings demonstrate that itaconate loss promotes the usage of the reductive TCA cycle in double stimulated macrophages.

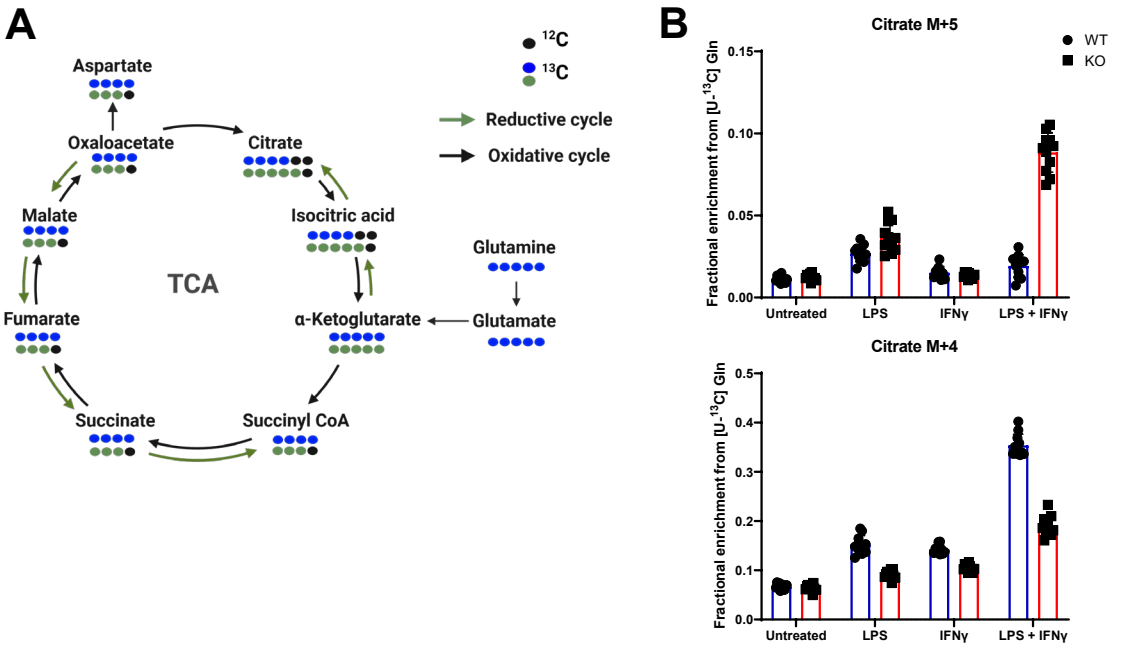

Figure 14. Double stimulated KO BMDMs convert α-Ketoglutarate to Citrate using a reductive path.

A, Schematic representation of the stable isotope tracing of a fully labelled ^{13}C glutamine molecule within the TCA cycle turning in the oxidative way (blue) and the reductive way (green). When circling in the reductive way, the five labelled carbons of aKG are transferred to become Citrate leading to Citrate M+5 instead of Citrate M+4. **B,** Fractional enrichment from ^{13}C glutamine in LPS, IFNγ and double stimulated BMDMs of WT (blue) and KO (red) mice. Cells were stimulated and traced for 24h. WT=8, KO=11 from two independent experiments

5.1.7. IRG1 deficiency promotes NO production in LPS-IFNγ activated macrophages.

Previous sections revealed increased differences of metabolic fluxes and levels between WT and KO BMDMs after LPS-IFNγ stimulation within the TCA cycle. As the TCA cycle is adjacent to other major metabolic pathways, we investigated whether the changes seen in the TCA cycle have an impact on other pathways.

In pro-inflammatory macrophages part of the urea cycle is of great importance due to its ability to produce nitric oxide (NO) which is an immunoregulator as well as a toxic agent against pathogens.

Within the mitochondria Carbamoyl phosphate merges with ornithine to create Citrulline. Citrulline can then be exported out of the mitochondria and merge with aspartate forming Argininosuccinate which turns into arginine releasing fumarate (Figure 15, A). Arginine can then either be converted into ornithine releasing urea or can be converted into citrulline releasing NO. A direct link to the TCA cycle can be established with the released fumarate: it can convert to malate, enter the mitochondria, become oxaloacetate which can turn into aspartate and fuel the urea cycle.

Between the different stimulations, Aspartate levels are relatively steady in BMDMs except after IFNγ single stimulation where they double (Figure 15, B). Between WT and KO no significant differences can be seen in single stimulated BMDMs. However, the LPS-IFNγ double stimulation causes a significant aspartate increase in KO cells which is concordant with the malate levels (Figure 12).

The Citrulline levels are very low in untreated and single stimulated BMDMs regardless of genotype. In double stimulated cells the relative citrulline abundance rises 20 times more than after single LPS stimulation. The difference between WT and KO is also reflected in aspartate levels indicating that the increased citrulline levels could be due to a slower citrulline to arginine reaction than the arginine to citrulline reaction.

The arginine levels are equal between WT and KO regardless of the stimulation. However, differences between stimulations are noticeable: the levels of untreated cells are higher than the ones of stimulated cells. Additionally, the relative abundance in double stimulated cells is lower than in single stimulated cells further indicating that the cells are using more arginine to potentially produce NO.

As the levels of Urea cycle metabolite indicate a potential link to NO release, the NO concentration was measured in the medium of double stimulated cells. The NO concentration almost doubles in KO BMDMs compared to WT BMDMs raising from 25µM to 40µM (Figure 15, C).

Overall, the findings show that the double stimulation strongly activates the urea cycle reflected by citrulline accumulation. Moreover, IRG1 loss further promotes citrulline levels resulting in enhanced NO production.

A possible way to trace metabolites from the urea cycle is via 1-pyrroline-5-carboxylate (P5C). This metabolite is generated from glutamate which can be fully labelled using a [U-^{13}C]Gln tracer. The fully labelled P5C can be converted to ornithine M+5 which would induce M+5 labelling in other urea cycle metabolites. However, no labelled ornithine could be detected in any condition in both genotypes when BMDMs are traced with [U-^{13}C]Gln indicating that the P5C to ornithine reaction does not take place in BMDMs after 24h. Interestingly, Proline, another metabolite that can be generated from P5C, exhibited significant differences between WT and KO. Indeed, Proline levels remain steady in WT BMDMs when stimulated. However, they significantly increase in KO cells after LPS single stimulation and LPS-IFNγ double stimulation (Figure 15, D). Proline accumulation can be very relevant in context of atherosclerosis as it is a major compound of collagen. The stable isotope tracing of [U-^{13}C]Gln further confirms an increase of Proline M+5 in KO BMDMs stimulated with LPS only and with LPS-IFNγ showing that an increased proportion of Proline is generated from glutamine via glutamate and P5C.

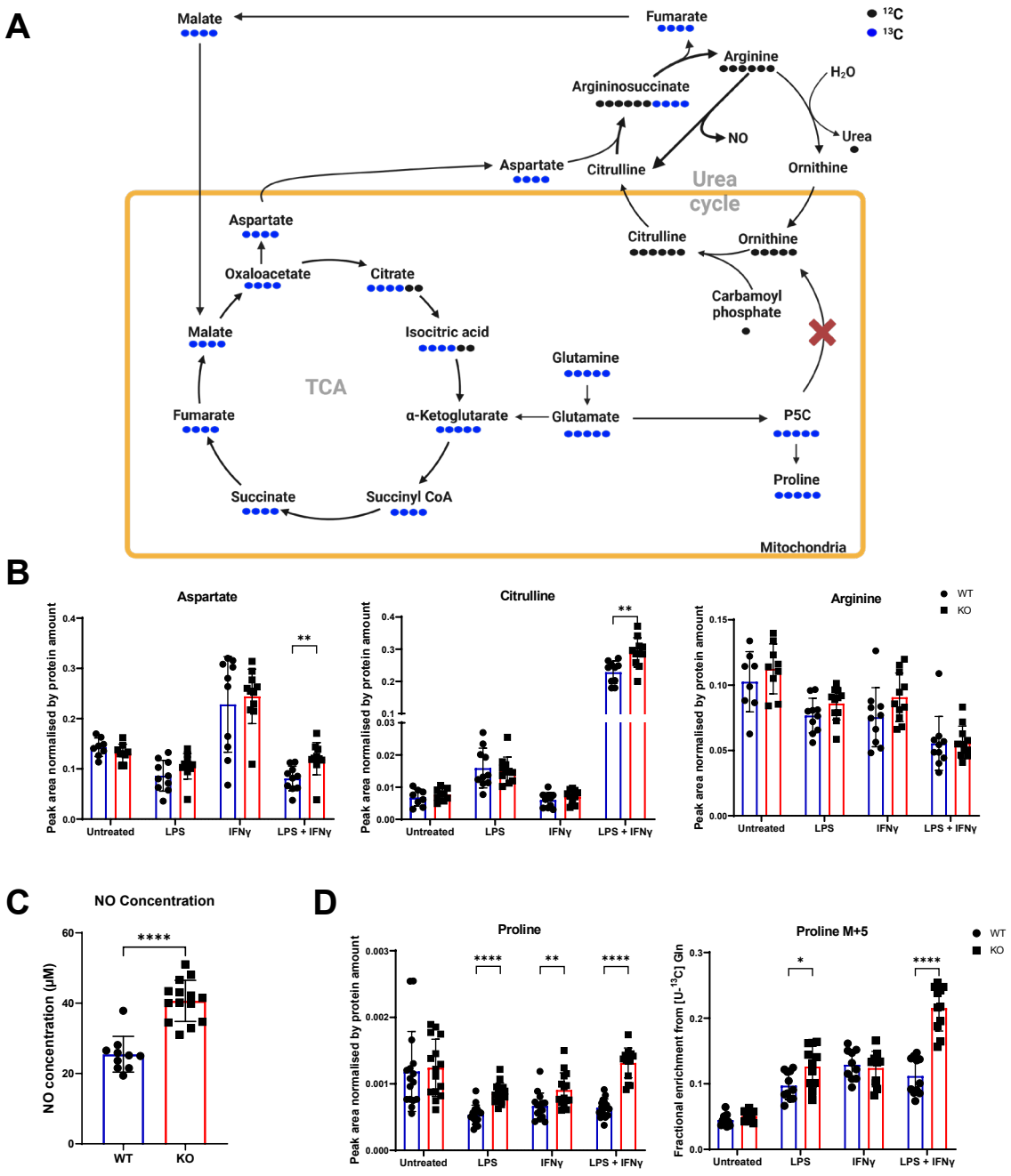

Figure 15. NO production is increased in LPS-IFNγ double stimulated KO BMDMs

A, Schematic representation of the stable isotope tracing of a fully labelled ^{13}C glutamine molecule between the TCA and Urea cycle. Aspartate M+4 enters the urea cycle merging with citrulline to become argininosuccinate M+4 which in turns become arginine M+0 releasing a fully labelled Fumarate M+4. Another entry point for the labelling is via P5C M+5 which can either become proline M+5 or ornithine M+5. Black dots represent ^{12}C atoms and blue dots represent ^{13}C atoms. **B**, Relative abundance of aspartate, citrulline and arginine in WT (blue) and KO (red) BMDMs stimulated for 24h with LPS and/or IFNγ. **C**, Griess assay to measure the NO concentration in the medium of WT and KO BMDMs stimulated for 24h with

LPS-IFNγ. **D**, Relative abundance of Proline (left) and Fractional enrichment from ^{13}C glutamine (right) in WT (blue) and KO (red) BMDMs stimulated for 24h with LPS and/or IFNγ. **B, C, D**, *P<0.05; **P<0.01, ****P<0.0001 by unpaired two-tailed Student's t-test. WT=10, KO=14

5.1.8. LPS-IFNγ stimulation reduces the effect of IRG1 deletion in the pyrimidine synthesis.

The previous sections demonstrated that the rewiring of the TCA cycle influences the urea cycle via aspartate. Indeed, aspartate and glutamate are involved in various metabolic pathways such as protein synthesis, and nucleotide metabolism. To that end we analysed nucleotide metabolism to investigate if alteration of aspartate and glutamate impact those pathways.

Glutamine contains two nitrogen atoms. One is directly linked to the α-carbon and the other is located within the amide group of the side chain. The [alpha-^{15}N]Gln tracer has its linked α-carbon nitrogen labelled and is employed to follow transamination processes within cells. When glutamine becomes glutamate, the α-nitrogen is conserved and can be in turn transmitted to aspartate during the transamination reaction combining glutamate with oxaloacetate resulting in the formation of aspartate and aKG (Figure 16, A). The labelled M+1 Aspartate can combine with Carbamoyl phosphate to generate N-Carbamoyl-L-Aspartate M+1 which in turn becomes orotate M+1 and after several steps is converted in uridine triphosphate (UTP) M+1.

The fractional enrichment of glutamate M+1 remains steady around 67% in WT BMDMs after single and double stimulation (Figure 16, B). In KO BMDMs, however, the fractional enrichment is reduced to 50% after LPS or IFNγ single stimulation. In contrast, double perturbation does not result in such a strong drop. Interestingly the total enrichment of glutamate with the [U-^{13}C]Gln tracer shows similar results with a labelling drop between single stimulated WT and KO BMDMs (Supplementary Figure 1). This indicates that IRG1 loss results in lower conversion from glutamine to glutamate in single stimulated cells. However, the double stimulation pushes the reaction in KO to reach a capacity comparable to WT BMDMs.

Because Aspartate is generated from glutamate, the labelling differences coming from glutamate M+1 are expected to be seen in aspartate M+1. Indeed, in WT cells, the fractional enrichment of Aspartate M+1 remains steady between 36% and 42% after single or double stimulation. In KOs it is reduced to 22% after single stimulation resulting in a difference of 15-16% labelling compared to WT cells. The labelling increases in KOs after LPS-IFNγ double stimulation. Yet it remains 10% below that of WT cells.

To normalise the differences of glutamine labelling, the ratio aspartate M+1 / glutamate M+1 was calculated. It shows that 56% of labelled aspartate comes from labelled glutamate in stimulated WT cells. In LPS or IFNγ single stimulated KO cells the ratio is lower and reaches 42%. However, when stimulated with LPS-IFNγ the ratio increases to 50% resulting in 6% difference between KO and WT. The results show that the reaction glutamate to aspartate is reduced in single stimulated KO BMDMs compared to WT BMDMs, but that this difference is reduced after LPS-IFNγ double stimulation.

To further analyse the pyrimidine synthesis, we analysed orotate enrichment. While being nearly absent without stimulation LPS or IFNγ single stimulation results in a strong ^{13}C enrichment of 20-30% (Figure 16, C). Interestingly, KO cells have very little orotate enrichment which is comparable to unstimulated WT cells. Only double stimulation resulted in similar ^{13}C enrichment which was, 10% below that of WT cells. After normalising the orotate M+1 enrichment to aspartate enrichment, it was apparent that pyrimidine synthesis was activated only in WT cells following single stimulation and that only dual stimulation increases ^{13}C flux into pyrimidine synthesis in KO cells. However, this flux still remained below that of WT cells.

The differences of labelling could be due to differences of orotate levels. Indeed, when measuring the relative levels, differences between the different stimuli could be observed. The orotate levels in single stimulated BMDMs were overall lower than in double stimulated BMDMs (Figure 16, D). Furthermore, levels of KO BMDMs were lower than WT BMDMs. However, the differences seen in orotate levels cannot fully explain the differences seen in orotate labelling between single stimulated WT and KO cells. The results indicate that the reaction from aspartate to orotate is overall decreased or slower in single stimulated KO cells compared to WT cells or that KO BMDMs use in priority the newly generated aspartate in other pathways.

From orotate cells can make uridine monophosphate (UMP) and in further steps UTP. A similar pattern to orotate M+1 can therefore be expected. Indeed, the UTP enrichment of LPS single and double stimulated BMDMs was comparable (Figure 16, E). However, it was very low in IFNγ stimulated cells. indicating that the reaction orotate to UTP is decreased in IFNγ stimulated BMDMs compared to LPS or LPS-IFNγ double stimulated cells. In KO BMDMs the labelling pattern of UTP M+1 is similar to Orotate M+1: lower than 1% in single stimulated cells and 7% in double stimulated cells. By calculating the ratio UPT M+1 on Aspartate M+1, a similar trend is observed with elevated values in WT LPS and LPS-IFNγ stimulated BMDMs and very low values in single stimulated KO BMDMs. Surprisingly the UTP levels are equal between WT and KOs except in double stimulated BMDMs where KO levels are significantly increased compared to WT levels.

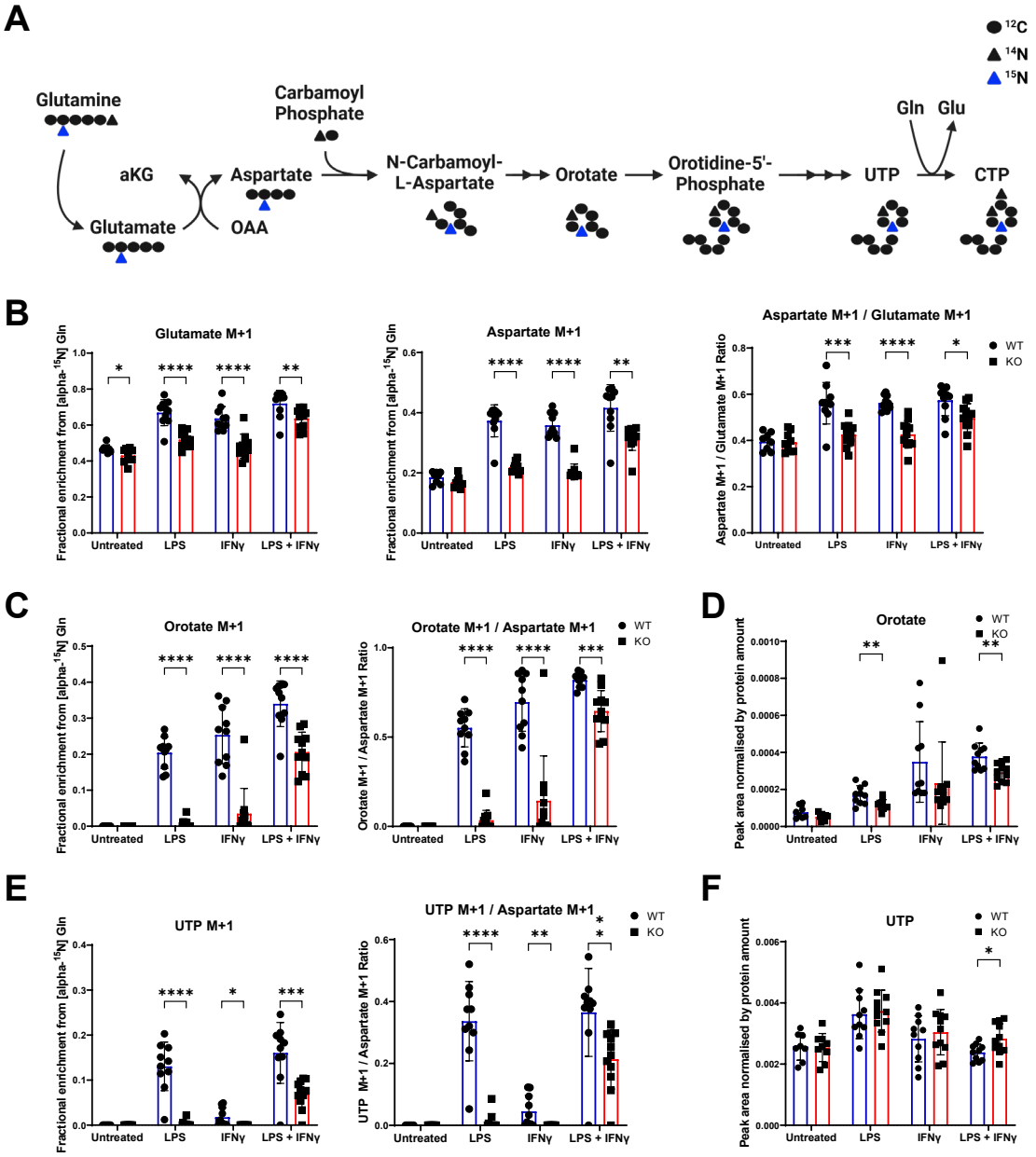

Figure 16. IRG1 deletion reduces the *de novo* pyrimidine synthesis.

A, Schematic representation of the stable isotope tracing of [alpha-^{15}N]Gln within the *de novo* pyrimidine biosynthesis pathway. Glutamine gives its labelled α^{15}N to glutamate which in turn can transmit it to aspartate by a transamination reaction. The labelled Aspartate can combine with carbamoyl phosphate to become N-carbamoyl-L-aspartate M+1 which can be converted to orotate M+1 and UTP M+1. Black dots represent ^{12}C atoms, black triangles represent ^{14}N atoms and blue triangles represent ^{15}N atoms. **B**,**C**,**E** Fractional enrichment from [alpha-^{15}N]Gln of Glutamate M+1 (B, left) Aspartate M+1 (B, middle) Orotate M+1 (C) and UTP M+1 (E) in LPS, IFNγ and double stimulated BMDMs of WT (blue) and KO (red) mice. On the right of each plot ratios of the corresponding metabolites are shown. **D**,**F**, Relative orotate (D) and UTP (F) levels of WT (blue) and KO (red) BMDMs after 24h LPS and/or IFNγ stimulation. The peak area is normalised by one internal

standard and by protein amount. **B,C,D,E,F**, *P<0.05; **P<0.01, ***P<0.001, ****P<0.0001 by unpaired two-tailed Student's t-test. All conditions are run in duplicates. WT: n=10 KO: n= 11 from two independent experiments.

Combining the increased tracing results and lower levels of WT double stimulated BMDMs compared to KO BMDMs, it can indicate that WT BMDMs consume more UTP and therefore need a faster or increased production. It can also indicate that KO cells could prefer recycling steps via the salvage pathway to produce UTP instead of *de novo* production.

To further investigate whether the *de novo* pyrimidine synthesis is affected by IRG1 deletion, a labelled glutamine amide nitrogen tracer was used. Compared to the [alpha-^{15}N]Gln tracer, the [amide-^{15}N]Gln tracer does not directly transmit its ^{15}N to glutamate. When glutamine converts to glutamate, the labelled ammonium is released and can be inserted in several pathways. This ammonium ion can be used to build carbamoyl phosphate resulting in carbamoyl phosphate M+1 which can then be used to build orotate M+1 and UTP M+1. Furthermore, UTP can be converted to cytidine triphosphate (CTP) using the amide nitrogen from glutamine potentially generating CTP M+2 (Figure 17, A). Surprisingly, we observed labelled glutamate in WT cells indicating that the glutamate dehydrogenase converts aKG to glutamate in WT BMDMs and to a lesser extent in KO BMDMs (Supplementary Figure 2)

Interestingly more than 80% of orotate M+1 is present in stimulated BMDMs regardless of the genotype (Figure 17, B). In unstimulated cells however, the labelling is reduced reaching 50% in WT cells and 17% in KO cells. Similar observations can be made with UTP M+1 where no differences between genotypes can be seen (Figure 17, C). However, the fractional enrichment of UTP M+1 is reduced in IFNγ stimulated cell.
Together with previous findings of Figure 16, C,E, the results point towards the absence of significant differences between WT and KO when attaining a steady state, however, they outline major differences of the use of *de novo* aspartate especially after LPS single stimulation.

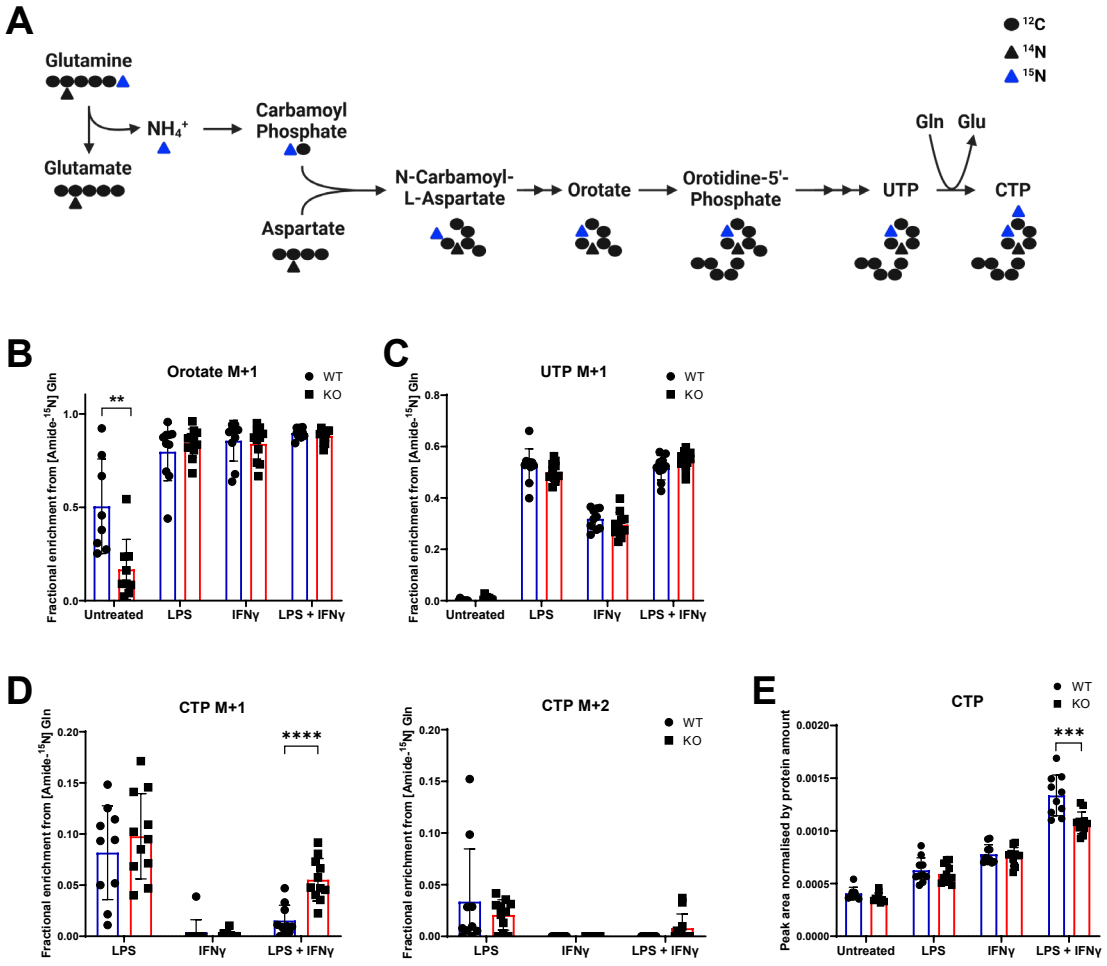

Figure 17. IRG1 deletion increases *de novo* CTP synthesis rate.

A, Schematic representation of the stable isotope tracing of [amide-^{15}N]Gln within the *de novo* pyrimidine biosynthesis pathway. Glutamine releases its labelled amide ^{15}N when becoming glutamate. This free ^{15}N unit can be used to create carbamoyl phosphate which combined with aspartate becomes N-carbamoyl-L-aspartate M+1. This metabolite can be converted to orotate M+1 and UTP M+1. UTP can become CTP by adding a free amide unit which can come from glutamine resulting in CTP M+2. Black dots represent ^{12}C atoms, black triangles represent ^{14}N atoms and blue triangles represent ^{15}N atoms. **B**,**C**,**D** Fractional enrichment from [amide-^{15}N]Gln of orotate M+1 (B) UTP M+1 (C) CTP M+1 (D, left) and CTP M+2 (D, right) in LPS, IFNγ and double stimulated BMDMs of WT (blue) and KO(red) mice. **E**, Relative CTP levels of WT (blue) and KO (red) BMDMs after 24h LPS and/or IFNγ stimulation. The peak area is normalised by one internal standard and by protein amount. **B,C,D,E,** **P<0.01, ***P<0.001, ****P<0.0001 by unpaired two-tailed Student's t-test. All conditions are run in duplicates. WT: n=10 KO: n= 11 from two independent experiments.

Due to the high labelling percentage of UTP M+1, CTP M+1 as well as CTP M+2 could be detected. While the labelling of CTP M+1 seems to be very variable between stimulated LPS cells, it is more stable in LPS-IFNγ double stimulated cells (Figure 17, D). Under this

condition a significant increase of labelling can be observed in KO cells. The results indicate that CTP generation from UTP is not a frequent process within macrophages but that this reaction increases in LPS-IFNγ stimulated KO cells. Interestingly CTP levels are lower in double stimulated KO BMDMs compared to WT BMDMs although the fractional enrichment of CTP+1 is increased (Figure 17, E).
The results indicate that double stimulated KO BMDMs generate more *de novo* CTP to potentially compensate for higher CTP needs.

5.1.9. De novo purine synthesis is not absent in BMDMs.

The previous section demonstrated that KO BMDMs do not prioritize aspartate incorporation in the pyrimidine synthesis pathway. To verify whether this statement also applies to the purine synthesis pathway, KO and WT BMDMs were traced with [alpha-^{15}N]Gln. This tracer enables the formation of Aspartate M+1 which can enter the purine synthesis pathway at an early stage during the conversion of 5'P-Ribosyl-4-Carboxy-Aminoimidazole (CAIR) to 5'P-Ribosyl-5-Amino-4-Imidazole Carboxamide (AICAR) leading to formation of AICAR M+1 which leads to the production of Inosine-5'-Phosphate (IMP) M+1 (Figure 18, A). IMP is the building block for Adenosine monophosphate (AMP) and Guanosine monophosphate (GMP). To form AMP and later adenosine triphosphate (ATP) from IMP, aspartate is required, leading to the potential formation of ATP M+1 or M+2 depending on IMP labelling. GMP and later guanosine triphosphate (GTP), on the other hand, do not require aspartate to be generated and will therefore keep the labelling of IMP potentially resulting in GTP M+1.
No labelling of GTP was detected in BMDMs from any genotype and in all stimulations using [alpha-^{15}N]Gln, indicating that IMP is probably not newly synthetised (Figure 18, B). Moreover, ATP M+1 can be detected but ATP M+2 cannot, further confirming that IMP is not synthetised within 24h after stimulation.
In WT cells the fractional enrichment of ATP fluctuates between the different stimulations reaching the highest enrichment in double stimulated cell. (Figure 18, C). Nevertheless, in KO cells, the fractional enrichment remains significantly lower. The double stimulation leads to an increase in the percentage of labelling in KO BMDMs, reaching 17% compared to 26% in WT cells. A similar trend is observed when normalising the ATP enrichment to aspartate enrichment. The ATP levels do not demonstrate any significant difference between WT and KO in stimulated cells. However untreated KO BMDMs have slightly less ATP than WT BMDMs (Figure 18, D).

To further confirm the previous observation, KO and WT BMDMs were traced with [amide-^{15}N]Gln. The free amide-^{15}N resulting from the glutamine to glutamate reaction can be incorporated in several steps of the purine synthesis. In the step generating 5-P-β-D-Ribosy amine from α-D-5-P-Ribosyl-PP (PRPP) and in the step generating 5'-Phosphoribosyl-N-Formylglycinamidine (FGAM) from 5'-Phosphoribosyl-N-Formylglycinamide (FGAR). When the cells incorporate the labelled amide group during both steps, it results in the formation of IMP M+2. This metabolite can either become ATP M+2 or GTP M+3 due to the transferred amide group from glutamine which is necessary to form GTP.

No labelled ATP could be detected in all conditions further indicating that *de novo* IMP is not generated within 24h of stimulation (Figure 18, F). This observation is further supported by the absence of GTP M+2 and GTP M+3. No significant labelling differences of GTP M+1 could be observed between WT and KO BMDMs in all tested conditions (Figure 18, G). Slight variations could be observed between the different stimuli going from 55% in single stimulated cells to 63% in double stimulated cells. Furthermore, there are no significant differences in GTP levels between WT and KO cells.

Overall, the results show no significant difference in GTP production between WT and KO cells. However significant differences are observed in ATP M+1 labelling from [alpha-^{15}N]Gln although not in ATP levels themselves. This observation is similar to the one made with the same tracer in UTP generation further indicating that differences of ATP M+1 labelling could be due to a different aspartate management between KO and WT BMDMs rather than a reduced ATP production. This can be linked to the increased NO production of KO BMDMs which requires aspartate to recycle the produced citrulline.

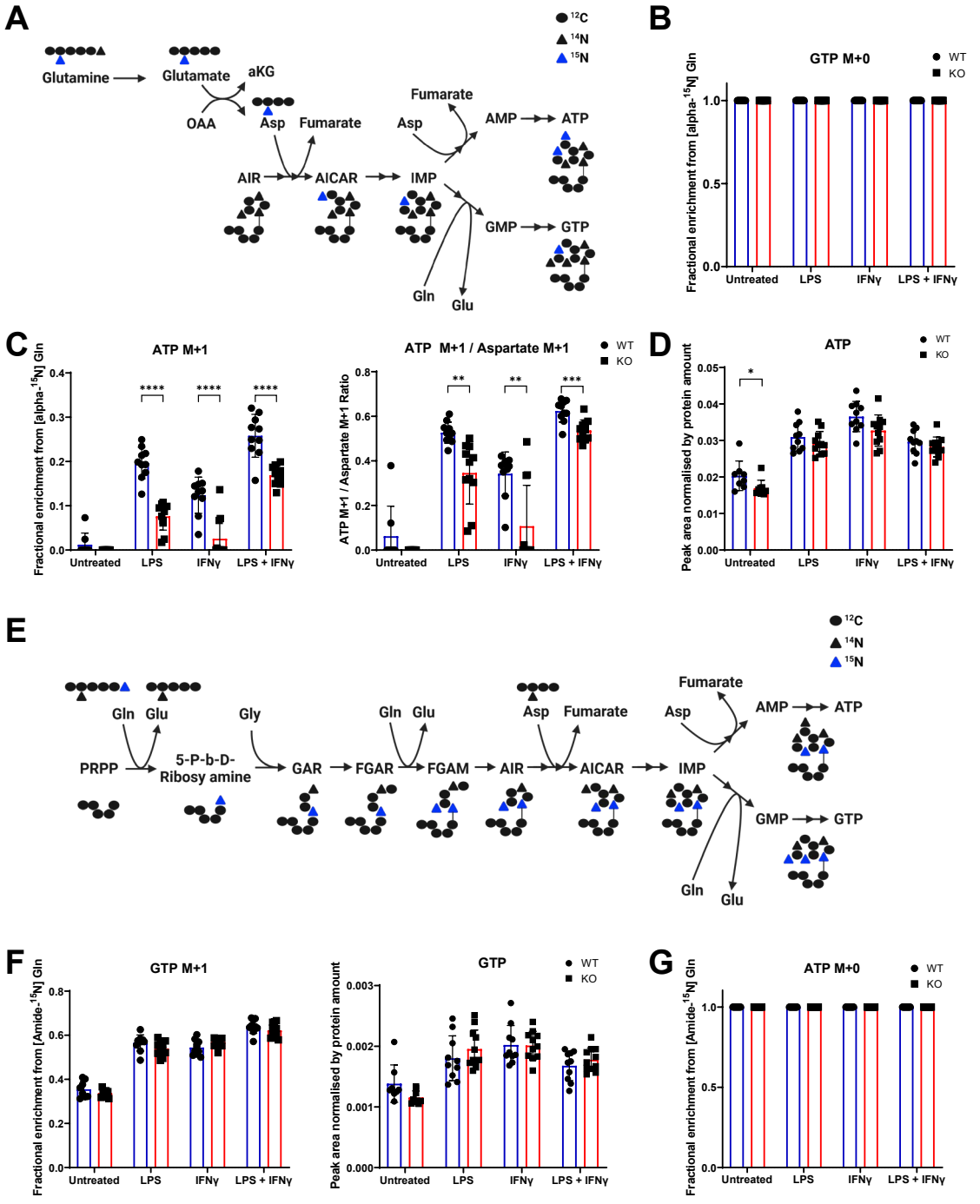

Figure 18. IRG1 deletion does not affect purine synthesis.

A, Schematic representation of the stable isotope tracing of [alpha-^{15}N]Gln within the *de novo* purine biosynthesis pathway. Glutamine gives its labelled α^{15}N to glutamate which in turn can transmit it to aspartate by a transamination reaction. The labelled Aspartate can enter the pathway in an early step between the reaction from 5'P-ribosyl-4-carboxy-5-aminoimidazole resulting in AICAR M+1, which turns into IMP M+1. Aspartate can also enter the pathway at a later stage between IMP and AMP resulting in AMP M+2 and therefore ATP M+2. IMP M+1 can also be converted to GMP M+1 and GTP M+1. **B**,**C** Fractional enrichment from [alpha-^{15}N]Gln of GTP M+0 (B) and ATP M+1 (C, left) in LPS, IFNγ and double stimulated

BMDMs of WT (blue) and KO (red) mice. On the right of the ATP M+1 plot, its ratio over aspartate M+1 is shown. **D**, Relative ATP levels of WT (blue) and KO (red) BMDMs after 24h LPS and/or IFNγ stimulation. The peak area is normalised by one internal standard and by protein amount **E**, Schematic representation of the stable isotope tracing of [amide-^{15}N]Gln within the *de novo* purine biosynthesis pathway. Glutamine releases its labelled amide ^{15}N when becoming glutamate. This free ^{15}N unit can enter the pathway in the early PRPP to 5-P-β-D-ribosy-amine step, or when FGAR is converted to FGAM potentially resulting to IMP M+1 or M+2. IMP can become ATP M+1/M+2 or can become GTP using the amide group from glutamine potentially resulting in GTP M+1 M+2 or M+3. Black dots represent ^{12}C atoms, black triangles represent ^{14}N atoms and violet triangles represent ^{15}N atoms. **F**,**G**, Fractional enrichment from [amide-^{15}N]Gln of GTP M+1 (F, left) and ATP M+0 (G) in LPS, IFNγ and double stimulated BMDMs of WT (blue) and KO (red) mice. **F**, right, Relative GTP levels of WT (blue) and KO (red) BMDMs after 24h LPS and/or IFNγ stimulation. The peak area is normalised by one internal standard and by protein amount. **C,D,F,** *P<0.05; **P<0.01, ***P<0.001, ****P<0.0001 by unpaired two-tailed Student's t-test. **B,C,D,F,G,** All conditions are run in duplicates. WT: n=10 KO: n= 11 from two independent experiments.

5.1.10. Exogenous itaconate can partially restore metabolic state.

In previous sections an extensive description of metabolic pathways of LPS and/or IFNγ stimulated BMDMs from IRG1 WT and KO mice has been provided showing that the double stimulation has enhanced effects on macrophage metabolism. To test if these observations are in causal relation to itaconate loss, 1mM itaconate was added to the medium of KO and WT BMDMs with LPS-IFNγ for 24h.

After the addition of itaconate, the itaconate levels in KO cells increase to reach the itaconate levels of WT cells that were not supplied with exogenous itaconate (Figure 19, A). This indicates that in the experimental setup itaconate levels of supplied KO cells reach basal itaconate levels of WT cell stimulated with LPS-IFNγ. However, despite the increase of succinate levels in KO cells after itaconate addition, the levels could not reach basal WT levels indicating that exogenous itaconate might not be as efficiently incorporated as produced itaconate to block SDH.

Other TCA cycle metabolites affected by IRG1 deletion like citrate and aKG are also affected by addition of exogenous itaconate. Indeed, Citrate levels are higher in WT cells compared to KO cells and itaconate addition to KO BMDMs could increase citrate levels to WT levels (Figure 19, B). Interestingly the addition of itaconate did not lead to an increase of Citrate in WT BMDMs.

In the absence of itaconate, KO cells exhibited higher aKG levels compared to WT cells. The introduction of exogenous itaconate to KO cells resulted in a significant reduction in

aKG levels; however, the levels remained elevated compared to those in WT cells. Interestingly, itaconate had less effect on aKG levels in WT BMDMs.

Citrulline levels which are increased in KO compared to WT BMDMs, decrease in KO when itaconate is added to attain WT levels (Figure 19, D). To further test if itaconate also directly affects NO production, nitrite levels were measured after addition of itaconate. Indeed, 41µM nitrite are measured in the medium of KO cells without itaconate addition (Figure 19, E). Upon itaconate addition this value decreases to 35µM. However, this decrease is not sufficient to reach the nitrite concentration of 25µM which is the concentration measured in the medium of WT regardless of itaconate addition.

After the addition of itaconate, the significantly elevated proline levels observed in LPS-IFNγ-stimulated KO BMDMs are reduced, bringing them closer to the levels found in WT cells (Figure 19, F). The same observation can also be made with UTP levels (Figure 19, G).

The dysregulated metabolic homeostasis observed in IRG1 deficient macrophages can be at least partially restored by exogenous addition of itaconate, indicating a causal relation between itaconate levels and urea cycle activity.

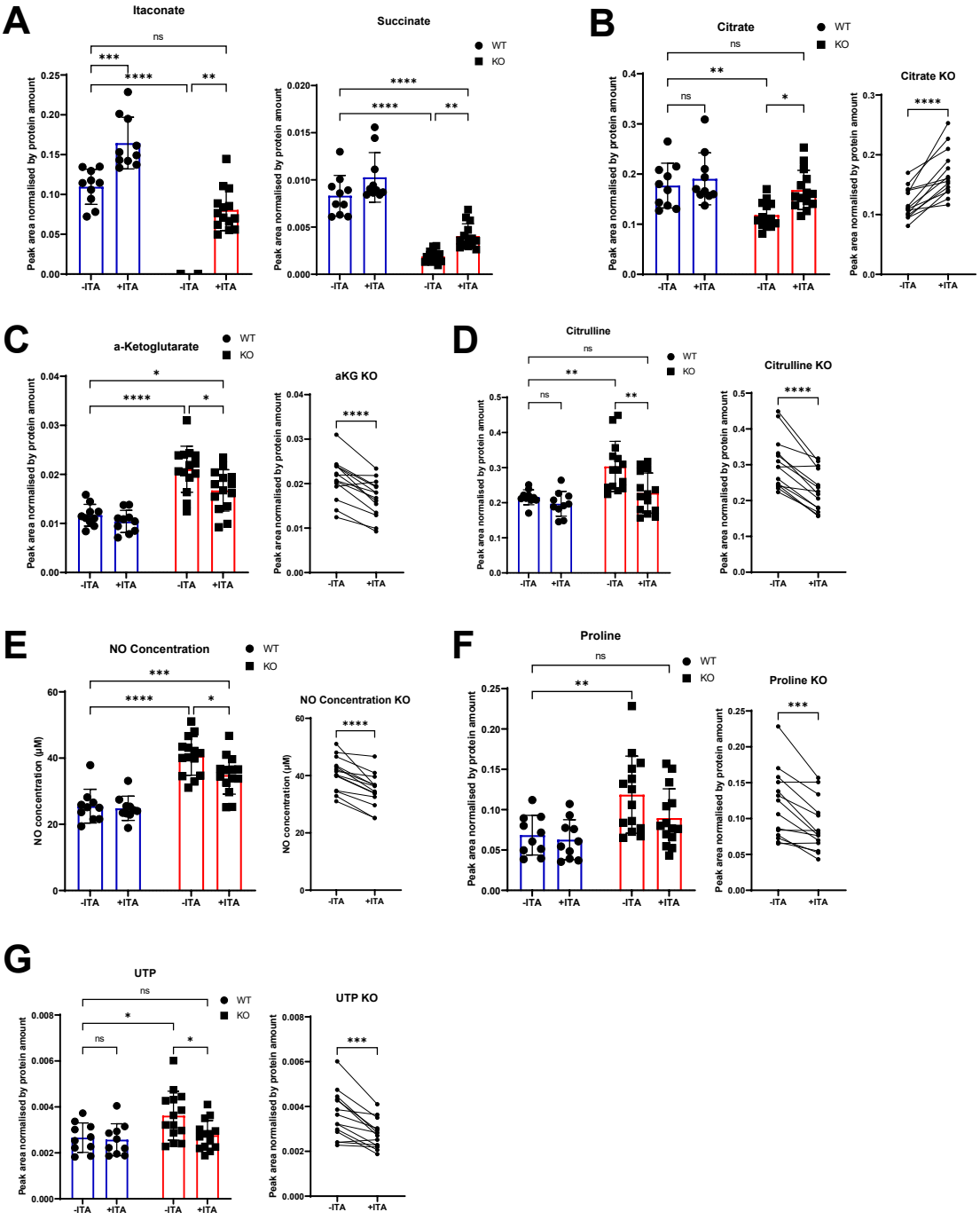

Figure 19. Exogenous itaconate can change metabolite levels of LPS-IFNγ stimulated KO cells.

Relative metabolite levels of WT (blue) and KO (red) BMDMs after 24h LPS-IFNγ double stimulation with or without itaconate. **B-G**, Relative metabolite levels of KO BMDMs treated with LPS-IFNγ with or without itaconate following each biological replicate before and after treatment (right of each plot). **A,B,C,D,F,G**, The peak area is normalised by one internal standard and by protein amount. **A-G:** Plot comparing WT and KO: *P<0.05;**P<0.01,***P<0.001,****P<0.0001 by ordinary two-way ANOVA with Sidak's multiple comparison test. **B-F**, right plot: ***P<0.001,****P<0.0001 by paired student's t-test.

5.1.11. iNOS inhibition affects itaconate levels as wells as related metabolites.

Major differences between KO and WT BMDMs are observed in the urea cycle with citrulline levels and NO production. To understand the impact of NO on macrophage metabolism and its implication in IRG1 deficient and WT cells, a specific inducible nitric oxide synthase (iNOS) inhibitor 1400w was given to BMDMs with LPS-IFNγ for 24h. The inhibitor will hinder pro-inflammatory macrophages to take the shortcut in the urea cycle enabling citrulline generation from arginine. The cells will therefore either accumulate arginine or continue the urea cycle by generating ornithine importing it into the mitochondria to produce citrulline (Figure 20, A). Aspartate is essential for the conversion of citrulline into arginine. Additionally, this metabolite can act as a connection between the TCA cycle and the Urea cycle. The aspartate levels rise after addition of 1400w especially in KO BMDMs suggesting that aspartate cannot be re-used as efficiently while its generation continues notably in KO cells (Figure 20, B).

All urea cycle metabolite levels change as expected after iNOS inhibition (Figure 20, C). Indeed, Citrulline levels drastically drop after 1400w addition, while arginine and ornithine levels increase. All the changes induced by 1400w can be observed in both genotypes. The overall increase of arginine and ornithine levels suggest that the limiting reaction could be the ornithine – citrulline reaction. Indeed, the cells would require importing ornithine into the mitochondria and use carbamoyl phosphate to generate citrulline. Moreover, the orotate labelling of Figure 17, B, strongly suggest that carbamoyl phosphate is essentially used to build pyrimidines further suggesting that BMDMs cannot produce as much citrulline from ornithine.

Overall, the results indicate that in the experimental setup, 1400w can block iNOS which is translated by the increase of arginine and ornithine levels and by the decrease of citrulline levels.

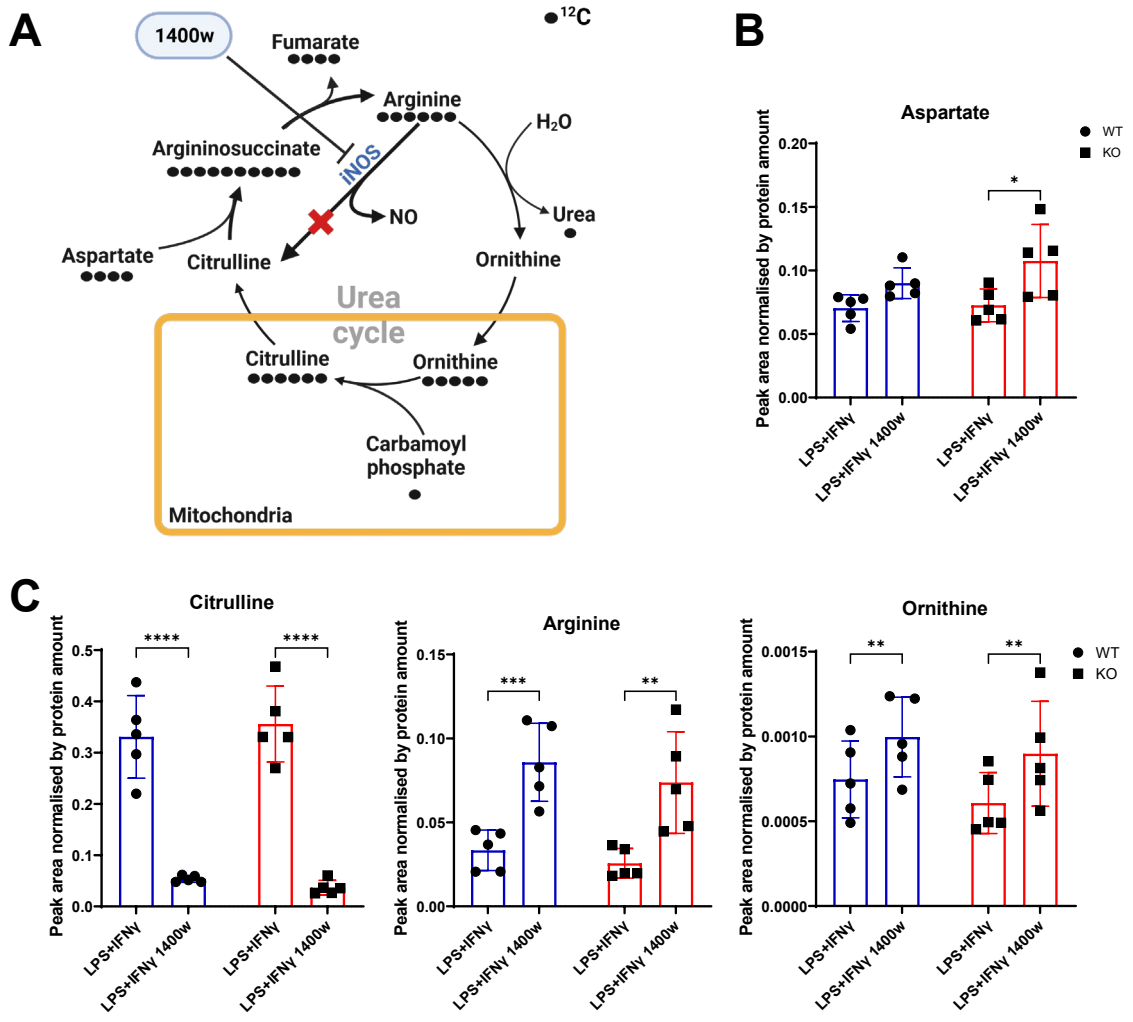

Figure 20. iNOS inhibition equally affects urea cycle metabolites of double stimulated WT and KO BMDMs

A, Schematic representation of the effects of 1400w on urea cycle metabolites. 1400w inhibits iNOS which catabolises the reaction arginine to citrulline releasing NO. Without this reaction, the cell is forced to continue the cycle by producing ornithine **B**, Relative aspartate levels of WT (blue) and KO (red) BMDMs after 24h LPS-IFNγ double stimulation with or without 1400w. **C**, Relative metabolite levels of urea cycle metabolites of WT (blue) and KO (red) BMDMs after 24h LPS-IFNγ double stimulation with or without 1400w **B,C**, The peak area is normalised by one internal standard and by protein amount. *P<0.05; **P<0.01, ***P<0.001, ****P<0.0001 by ordinary two-way ANOVA with Sidak's multiple comparison test. WT n=5, KO n=5 from one experiment

After validating the experimental conditions, TCA cycle metabolites as well as pyrimidines levels are measured. Interestingly iNOS inhibition increases itaconate levels in WT BMDMs (Figure 21, A). The succinate levels slightly rise in WT cells after 1400w addition likely due to the increased itaconate levels as no changes could be observed in KO cells. Surprisingly, the inhibition of iNOS led to a decrease in Citrate levels in WT cells, while no significant changes were observed in KO cells. This suggests that the absence of iNOS, in the presence of itaconate, is sufficient to reduce Citrate levels. Furthermore, the addition of 1400w did not alter Citrate levels in IRG1 KO cells. However, aKG levels are not significantly changed after 1400w addition in WT and KO BMDMs. A slight tendency towards a reduction in aKG levels is observed. Finally, malate and fumarate levels are significantly reduced in KO BMDMs after addition of 1400w. The inhibition of iNOS resulted in a reduction reaching comparable levels of both metabolites in WT and KO cells. Interestingly the results of malate and fumarate levels do not show the same trend as aspartate levels. While aspartate accumulates, malate and fumarate levels drop, indicating that after iNOS inhibition both metabolites might be more used without the capacity to be regenerated as efficiently.

WT BMDMs demonstrate a significant increase in UTP levels following the addition of 1400w (Figure 21, B). Furthermore, in KO BMDMs, UTP levels tend to increase, reaching a level equivalent to that observed in WT cells treated with 1400w. In WT cells, inhibition of iNOS results in a significant decrease in CTP levels (Figure 21, B). However, no significant differences in CTP levels are observed in KO cells, regardless of the presence or absence of 1400w. Interestingly, the addition of 1400w equalizes CTP levels in both WT and KO BMDMs.

Overall, the results show that iNOS inhibition reduced the differences between WT and KO BMDMs of metabolite levels from the TCA cycle and from Pyrimidines. Despite various differences between WT and KO cells without 1400w, most described metabolites changed their levels to become similar between WT and KOs after 1400w addition. Itaconate and succinate however remain different between WT and KO BMDMs even after addition of 1400w suggesting that NO could be an IRG1 regulator.

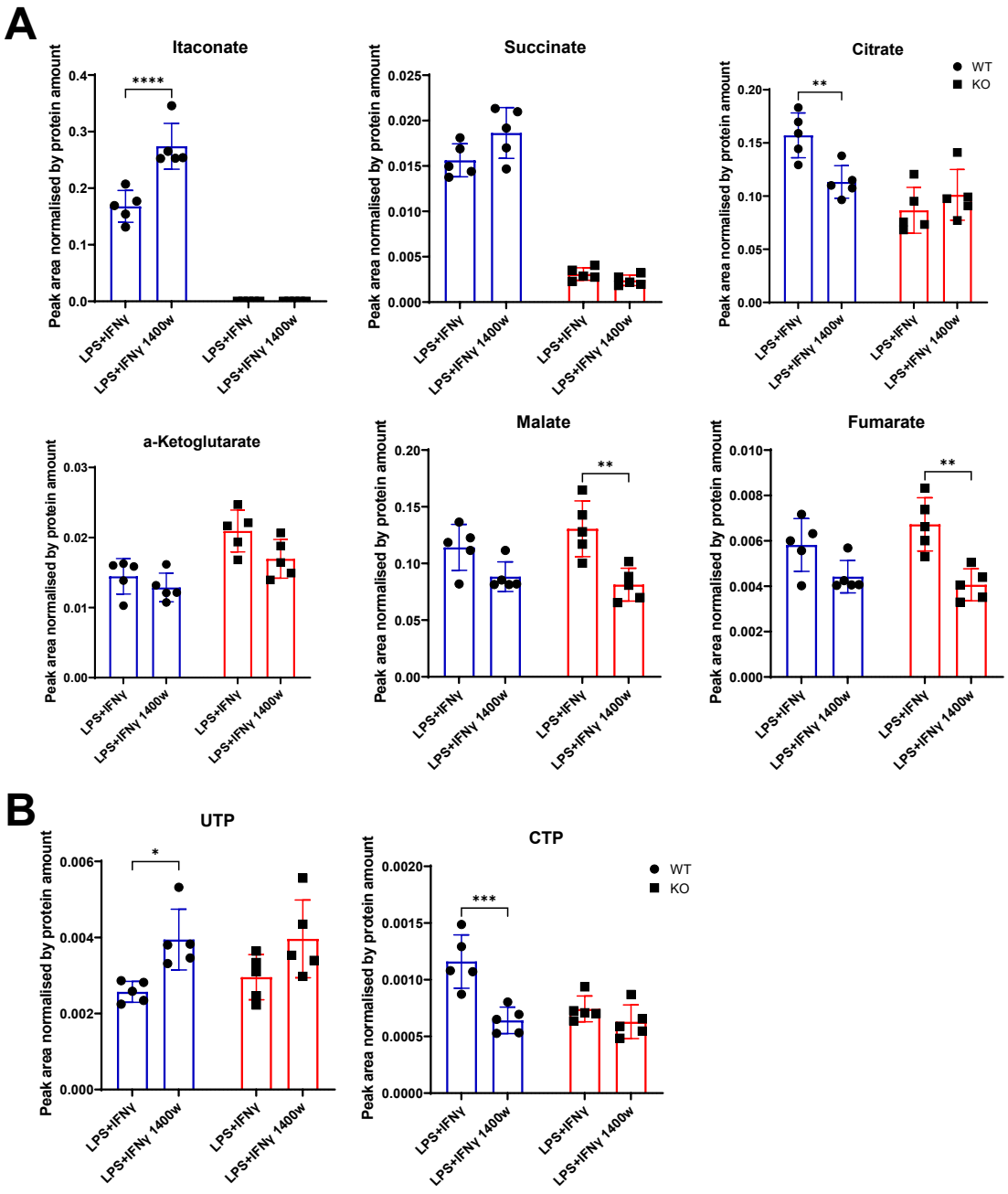

Figure 21. iNOS inhibition equalizes metabolite levels of LPS-IFNγ stimulated KO and WT BMDMs

A, B, Relative levels of TCA cycle metabolites (A) and Pyrimidines (B) of WT (blue) and KO (red) BMDMs after 24h LPS-IFNγ double stimulation with or without 1400w. The peak area is normalised by one internal standard and by protein amount. *P<0.05;**P<0.01,***P<0.001,****P<0.0001 by ordinary two-way ANOVA with Sidak's multiple comparison test. WT n=5, KO n=5 from one experiment

5.1.12. Phenotypical changes in BMDMs induced by IRG1 deletion.

The metabolic changes of LPS-IFNγ double stimulated BMDMs are extensively depicted in previous sections of the thesis. However, no associated functional implications have been described yet. To have a broader vision of potentially affected pathways induced by IRG1 deletion in pro-inflammatory macrophages, an RNA sequencing was performed in LPS-IFNγ double stimulated KO and WT BMDMs. The RNA sequencing analysis was done by Dr. Etienne Moussay.

The RNA sequencing pinpointed several differentially expressed genes between WT and KO (Figure 22, A). Interestingly, CMPK2 the enzyme catalysing UMP to UDP and CMP to CDP has a higher expression in WT BMDMs. This enzyme is essential in the pyrimidine salvage pathway suggesting that WT cells favour the salvage pathway over the *de novo* synthesis pathway to synthetise CTP. This is in line with our observations made in Figure 17, D, E. The metascape analysis indicates that leukocyte chemotaxis genes are highly downregulated in KO BMDMs (Figure 22, B). This indicates that KO macrophages might migrate slower compared to WT BMDMs. Other downregulated genes include immune function related genes like regulatory genes of immune system processes and regulatory genes of immune effector processes. Interestingly genes involved in pyrimidine deoxyribonucleotide metabolic processes are also downregulated in KO cells. This gene Ontology term (GOterm) comprises 21 genes including CMPK genes encoding for enzymes catalysing the formation of CMP and UMP. This is in line with the elevated CTP levels observed in LPS-IFNγ WT BMDMs. Upregulated genes in KO BMDMs include regulatory genes of cytokine production (Figure 22, C). This aligns with several studies showing that itaconate has a role in IL1b and IL6 production. Interestingly several GOterms involving lipid metabolism are also upregulated in KO BMDMs indicating that lipid metabolism might be altered in KO BMDMs.

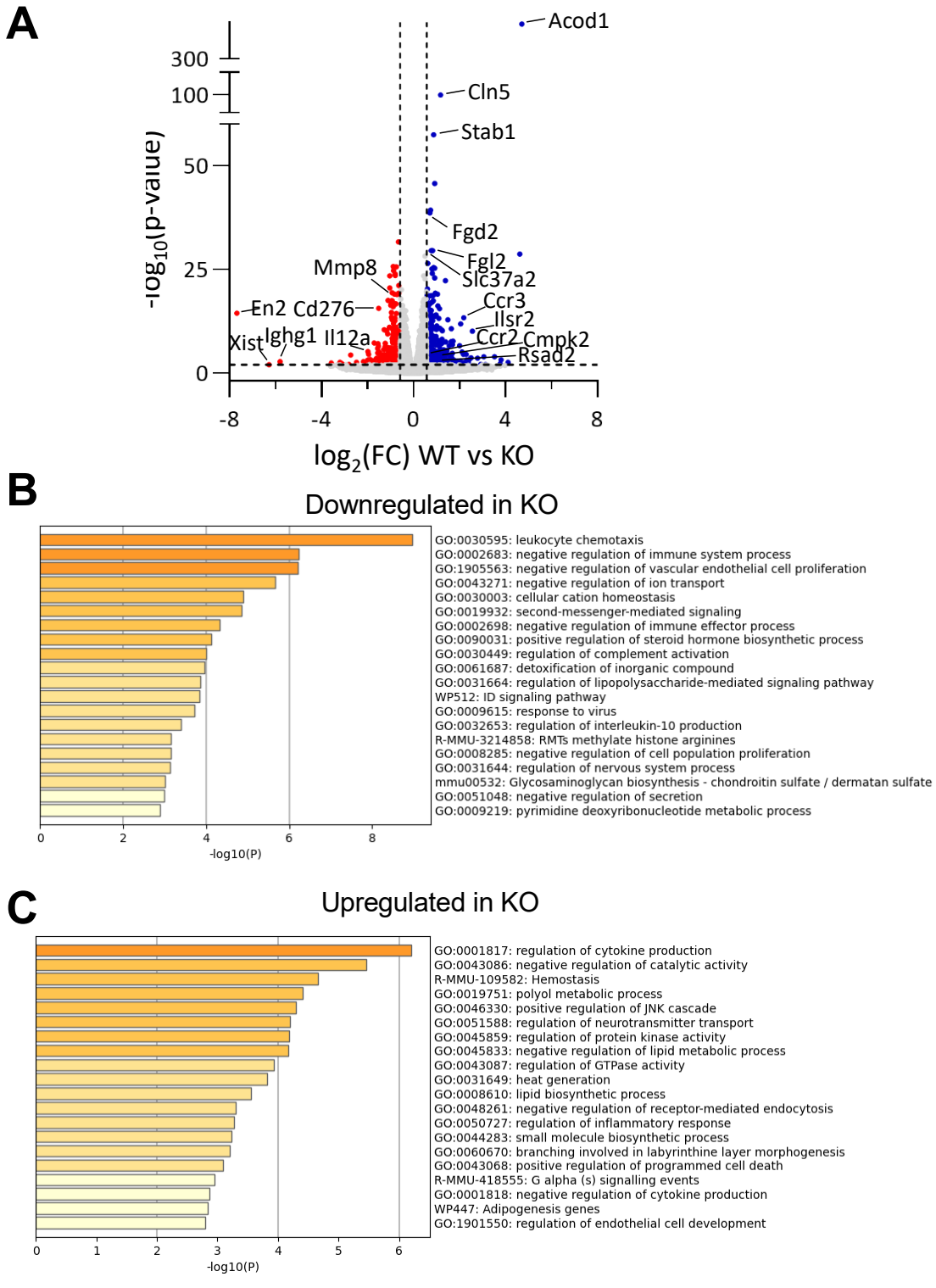

Figure 22. Differentially expressed genes in WT and KO BMDMs

A, Volcano plot of differentially expressed genes of WT (blue) and KO (red) BMDMs stimulated for 24h with LPS-IFNγ. **B, C**, Metascape analysis of downregulated (B) and upregulated (C) genes in IRG1 KO BMDMs stimulated for 24h with LPS-IFNγ compared to WT BMDMs.

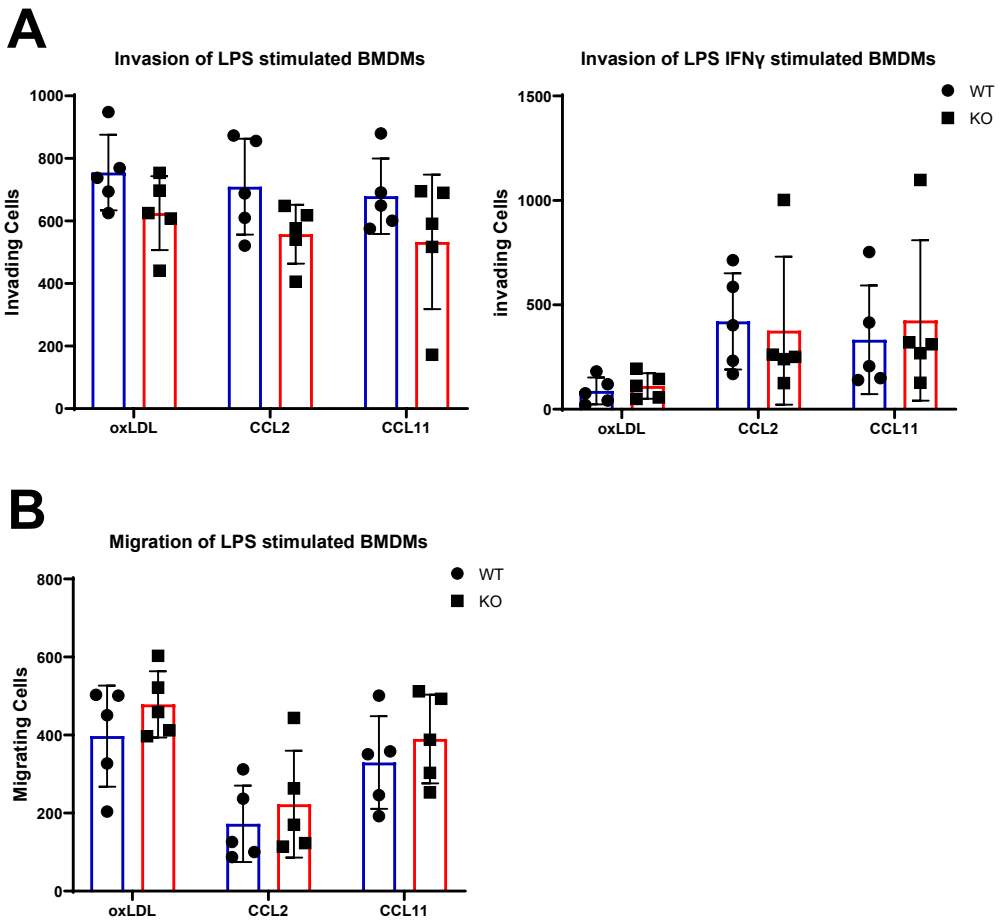

Figure 23. Macrophage chemotaxis is not affected by IRG1 deletion.

A, Transwell assay with coated inserts simulating tissue invasion of macrophages. The bottom of each well is supplement with a chemoattractant: oxLDL, CCL2 or CCL11. BMDMs from WT (blue) and KO (red) mice are seeded inside the insert without chemoattractant and are stimulated with LPS (left) or LPS-IFNγ (right) for 72h. **B,** Transwell assay without coated inserts simulating cell migration. The bottom of each well is supplement with a chemoattractant. BMDMs from WT (blue) and KO (red) mice are seeded inside the insert without chemoattractant and are stimulated with LPS for 72h. **A-B**, Five pictures are taken of the bottom from each insert. In each picture cells are counted giving a cell count per transwell. Statistics are calculated by unpaired two-tailed Student's t-test. WT n=5, KO n=5 from one experiment.

In order to validate the chemotaxis-related GOterm that showed the highest upregulation in WT BMDMs, a transwell assay was conducted. Several specific genes associated with chemotaxis, including C-C Motif Chemokine Receptor 3 (CCR3), CCR2, and CCR1, were found to be downregulated in KO cells. To assess the chemotactic response, both C-C Motif Chemokine ligand 11 (CCL11) and CCL2, which bind to CCR3 and CCR2, respectively,

were employed as chemoattractant during the assay. Additionally, oxLDL was utilized as a chemoattractant to observe the response of BMDMs when exposed to it. The transwell inserts are coated to simulate the tissue environment through which macrophages must go through to reach the danger signal. The cells from five pictures taken from the lower side of the transwell, are counted to obtain a cell count per transwell.

When oxLDL is used as chemoattractant, no significant differences are measured between WT and KO suggesting no difference of chemotaxis abilities between LPS stimulated WT and KO BMDMs (Figure 23, A). Similarly, no major differences are observed between WT and KO when CCL2 or CCL11 is employed as chemoattractant. Double stimulated BMDMs do not invade as efficiently as single stimulated LPS BMDMs with an average lower cell count. Interestingly, they exhibited increased mobility when CCL2 or CCL11 is employed a chemoattractant compared to oxLDL, while still being less mobile than the LPS-stimulated cells.

The results show that the invading capacity of BMDMs is not significantly reduced in LPS single stimulated KO BMDMs when oxLDL, CCL2 and CCL11 are used as chemoattractant. However, it is possible that the migrating capacity of BMDMs is affected by IRG1 deletion. To test this hypothesis a transwell assay was conducted in which the inserts are not coated. As double stimulated BMDMs do not move as efficiently as single stimulated BMDMs, cells were only treated with LPS.

Similar to the invasion assay, no significant differences could be detected between WT and KO cells (Figure 23, B). Overall, the results could not validate the downregulation of chemotaxis in KO BMDMs after LPS single or LPS-IFNγ double stimulation.

To further analyse the RNAseq results, a gene set enrichment analysis (GSEA) was conducted. The GSEA revealed high normalised enrichment score (NES) in several gene sets, notably in sets linked to eucaryotic translation (Figure 24, A). To confirm whether the translation is increased in double stimulated KO BMDMs, a translation assay was conducted using O-propargyl-puromycin (OPP). OPP is inserted in newly generated proteins and a click-it system can couple the OPP to a fluorochrome. Cells are then analysed by flow cytometry and the median fluorescence intensity is measured. The higher the value, the more OPP was incorporated, the more translation took place. No significant changes between WT an KO could be detected indicating that translation processed are not affected by IRG1 loss (Figure 24,B).

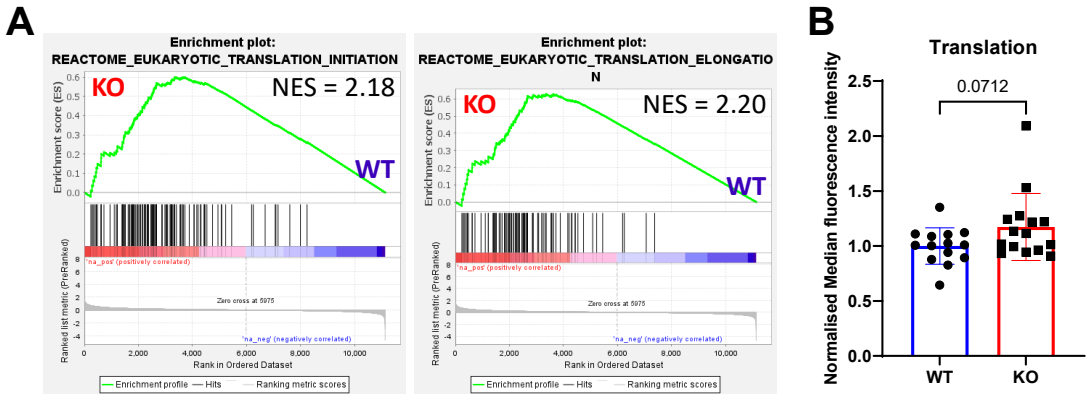

Figure 24. IRG1 deletion does not affect macrophage translation.

A, GSEA enrichment plots show enrichment of genes involved in eucaryotic translation initiation (left) and elongation (right) in KO (red) and WT (blue) BMDMs. **B**, Translation assay using the OPP click-it Kit. OPP is incorporated in newly generated proteins and is attached to a fluorescent dye with the click-it system. The median fluorescence intensity is then analysed by flow cytometry. BMDMs from WT (blue) and KO (red) were stimulated for 24h with LPS-IFNγ. OPP was added during 30min before experiment end. The median fluorescence intensity of each biological replicate is normalised to the average of WT values from the experiment. WT n=13, KO n=15 from 3 independent experiments

To assess whether the capacity of IRG1 deficient BMDMs to phagocyte oxLDL particles is impaired, a cholesterol influx assay was conducted. Cells were incubated with LPS-IFNγ as well as fluorescent oxLDL particles. After 24h the median fluorescent intensity was measured by flow cytometry. The higher the fluorescence intensity, the more fluorescent particles were phagocyted. Interestingly, the median fluorescence intensity was reduced in KO BMDMs compared to WT cells suggesting that KO phagocyted less oxLDL particles (Figure 25). As oxLDL phagocytosis is mainly mediated by SRs our results indicate that certain SRs in IRG1 deficient BMDMs might not detect oxLDL as efficiently as in WT BMDMs

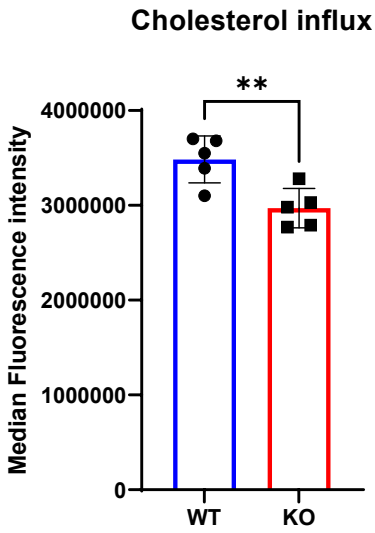

Figure 25. Cholesterol influx is reduced in IRG1 KO BMDMs

Flow cytometry analysis of LPS-IFNγ treated IRG1 WT and KO BMDMs supplemented with oxLDL complexed with a fluorescent DiI dye (DiI-oxLDL). The median fluorescence intensity was analysed by flow cytometry after 24h. Statistics are calculated by unpaired two-tailed Student's t-test. WT n=5, KO n=5 from one experiment.

5.2. The role of IRG1 in atherosclerosis

5.2.1. Plasma cholesterol levels and body weight are affected by IRG1 deletion in male mice in the LDLr model.

To study and compare the role of IRG1 in atherosclerosis in different models, the ApoE model and the LDLr model are employed. Both models promote atherosclerosis development after being given a fat enriched diet for several weeks. As the weight gain can be an atherosclerosis severity indicator (Scolaro et al., 2023), the weight of the animals was monitored over time after the start of the diet. Male IRG1 KO mice with the LDLr background tend to gain more weight over time than their IRG1 WT counterparts. Indeed, after 12 weeks HFD, male KO mice weighted on average 35g and WT mice 31g (Figure 26, A). However, in female mice of the same background no differences were observed between KO and WT. The results are further confirmed when looking at the weight gain after 12 weeks HFD. Indeed, WT males gained on average 8g while KO mice gained 11g (Figure 26, B). Female mice on the other hand gained around 5g regardless of the genotype.

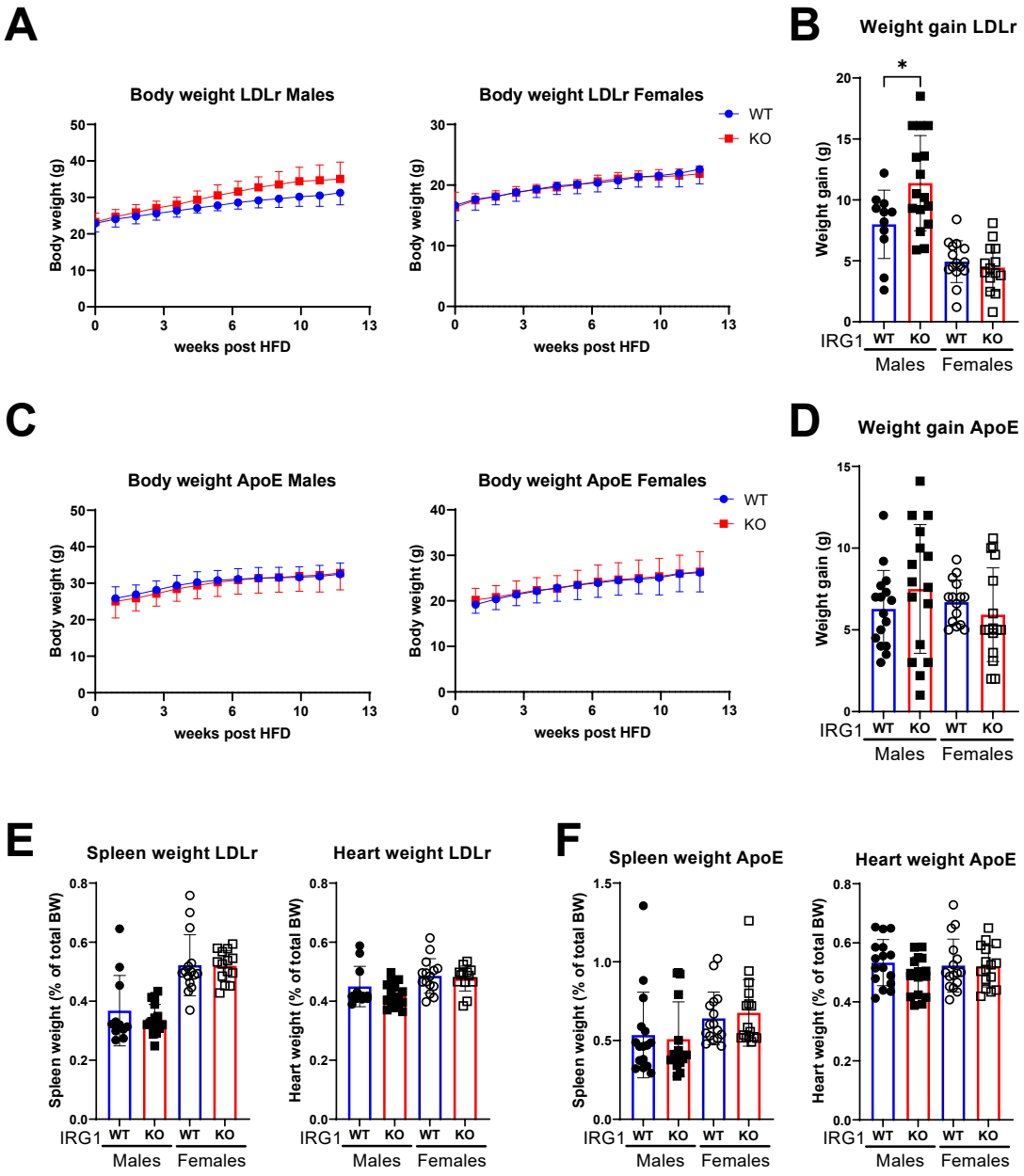

Figure 26. The body weight of male IRG1 LDLr deficient mice increases after 12 weeks HFD.

A,C, Body weight of LDLr KO (A) and ApoE KO (C) IRG1 WT (blue) and KO (red) mice over time given a HFD for 12 weeks. **B,D**, Weight gain of LDLr KO (B) and ApoE KO (D) IRG1 WT (blue) and KO (red) after 12 weeks HFD. **E,F**, Spleen weight and heart weight in percentage of total body weight of LDLr KO (E) and ApoE KO (F) IRG1 WT (blue) and KO (red) after 12 weeks HFD. *P<0.05 by unpaired two-tailed Student's t-test. LDLr Males WT n=11 KO n=16; LDLr Females WT n=15 KO=14; ApoE Males WT n=16 KO n=16; ApoE Females WT n=16 KO n=16

In the ApoE background, no differences were observed between IRG1 WT and KO males and female mice. Indeed, males weighted on average 33g after 12weeks HFD and females weighted 26g regardless of genotype (Figure 26, C). The weight gain after 12weeks HFD

is also not significant (Figure 26, D). To further investigate potential variations between IRG1 WT and KO mice, the weight of the spleen and heart was assessed. No differences were found between WT and KO mice, irrespective of their genetic background or gender (Figure 26, E, F).

The weight results show that IRG1 KO male mice in the LDLr background gain more weight after 12 weeks HFD compared to IRG1 WT male mice which suggests increased atherosclerosis severity in LDLr IRG1 KO male mice. On the other hand, female LDLr mice as well as ApoE mice do not display any difference regarding weight.

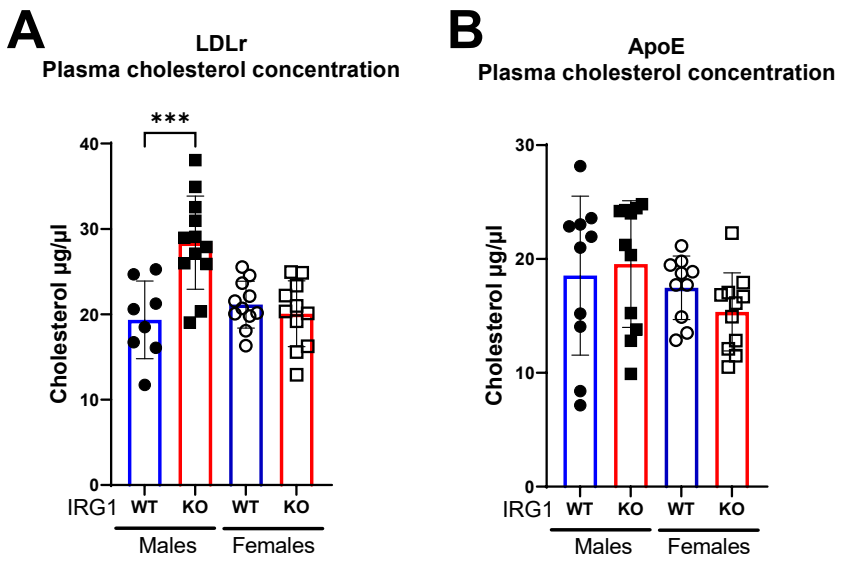

Figure 27. Plasma cholesterol concentration increases in male IRG1 LDLr deficient mice.

Cholesterol concentration in the plasma of LDLr KO (A) and ApoE KO (B) IRG1 WT (blue) and KO (red) mice after 12 weeks HFD. ***P<0.001 by unpaired two-tailed Student's t-test. LDLr Males WT n=8 KO n=12; LDLr Females WT n=11 KO=11; ApoE Males WT n=10 KO n=11; ApoE Females WT n=10 KO n=11

High plasma cholesterol levels increase the risk of atherosclerotic cardiovascular events. Therefore, the plasma cholesterol levels of the mice were measured after 12 weeks HFD. Interestingly, male IRG1 KO mice in the LDLr background had more total cholesterol than male IRG1 WT mice. In fact, the measured concentration reached 28 µg/µL in KO and 19 µg/µL in WT mice (Figure 27, A). In LDLr KO females, the cholesterol concentration was around 20 µg/µL, irrespective of the IRG1 genotype. In the ApoE model, no significant differences in total cholesterol concentration were measured between IRG1 KO and WT mice (Figure 27, B).

The results show that IRG1 KO males in the LDLr model gain more weight and have increased total plasma cholesterol levels. However, heart weight and spleen weight in relation to total body weight do not change.

5.2.2. The plaque size is reduced in the aortic arch of female IRG1 deficient mice in the ApoE model.

Measuring plaque size is important for assessing the severity of atherosclerosis. Therefore, in addition to presenting the results of weight and cholesterol concentration, plaque size and composition were analysed in the aortic root and aorta. The en face analysis of the thoracic and abdominal aorta showed no significant difference between IRG1 WT and KO male and female mice in the LDLr model (Figure 28, A). Interestingly, in male mice, the plaque area tended to be slightly increased in KO mice. In female mice, however, KO mice tended to have slightly less plaque than WT mice. Similar to the findings in the LDLr model, no significant differences between WT and KO mice were observed in the ApoE model (Figure 28, B). In male mice, IRG1 KO tended to have a smaller plaque area compared to WT, with an average area of 3.9% in KO and 8.2% in WT. A similar trend was observed in female mice, with a mean area of 5% in KO and 6.9% in WT mice.
In general, the results indicate a trend towards reduced plaque formation in the thoracic and abdominal aorta in IRG1 KO mice except in male mice in the LDLr model. This difference could be linked to the increase of weight and plasma cholesterol concentration which is only observed in males of this model.

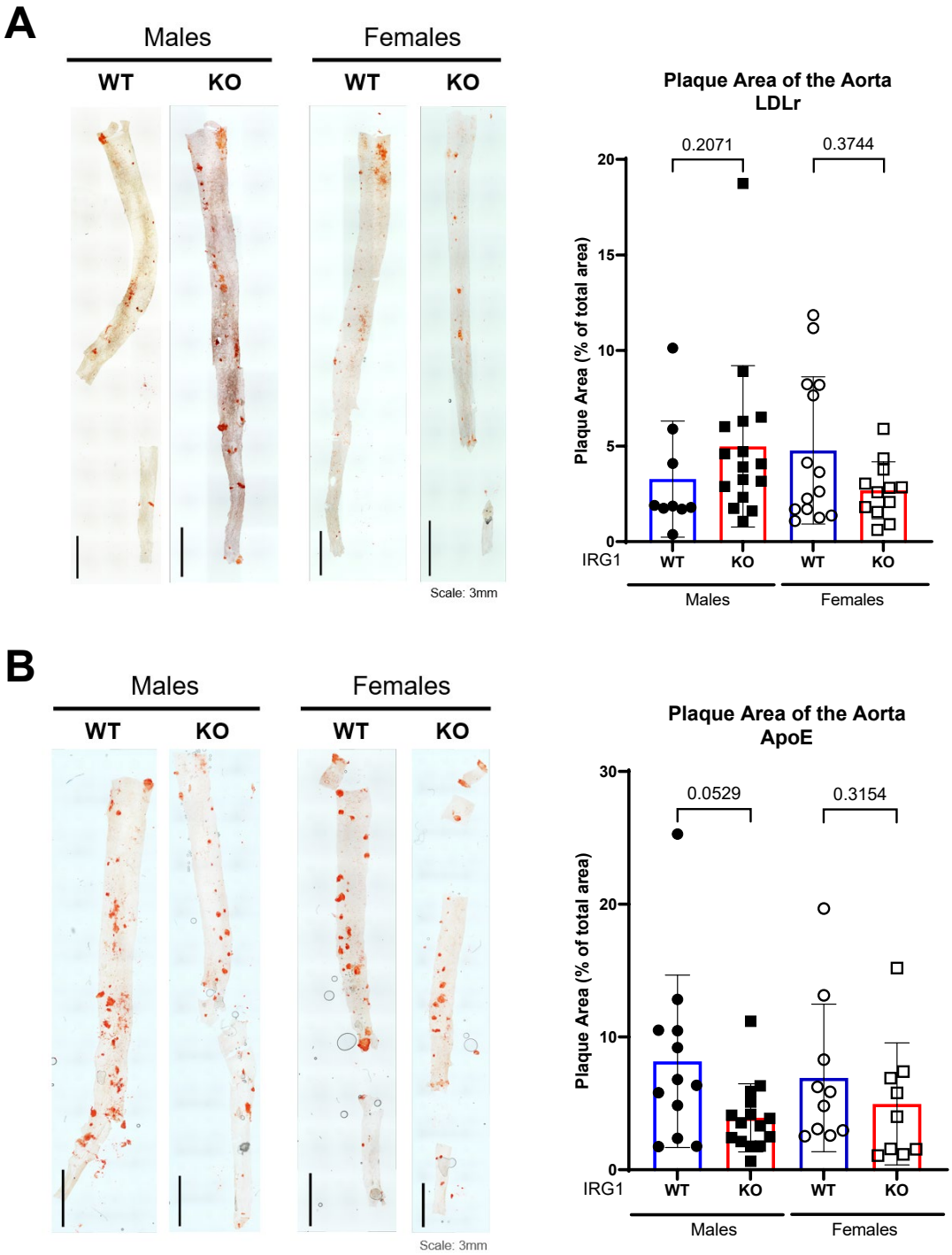

Figure 28. The plaque size of thoracic and abdominal aorta does not change in IRG1 KO mice.

En face analysis of the thoracic and abdominal aorta of LDLr KO (A) and ApoE KO (B) IRG1 WT (blue) and KO (red) mice. The aortas are stained with ORO to mark the lipids in red. Representative pictures (left), quantification (right). Scale bar: 3mm. P value calculated by non-parametric Mann-Whitney test. **A,** Males WT n=9 KO n=16; Females WT n=14 KO=13 **B,** ApoE Males WT n=11 KO n=14; ApoE Females WT n=7 KO n=6.

To further assess atherosclerosis severity, the plaque area in the aortic root was measured. No significant differences were observed between IRG1 KO and WT male and female mice in both LDLr and ApoE models. In male mice of the LDLr model, the plaque area was approximately 0.3 mm² in males and 0.45 mm² in females (Figure 29, A). In the ApoE model, the plaque area was 0.24 mm² in males regardless of IRG1 genotype, 0.42 mm² in WT females and 0.48 mm² in KO females (Figure 29, B).

Alongside plaque size, measuring the collagen composition of plaques holds significant importance as it provides insights into plaque stability. The collagen area determined by Masson's trichrome stain, was also not significantly different between IRG1 WT and KO mice in the LDLr and ApoE models. In the LDLr model, male WT mice exhibited a collagen area of 7.4% of plaque area, while in male KO mice the area was 11.1% (Figure 30, A). Among female mice in the LDLr model, WT mice had a collagen area of 19.3%, whereas KO mice had an area of 17%. In the ApoE model, both male WT and KO mice exhibited similar collagen areas, with percentages of 12.6% and 12.5%, respectively (Figure 30, B). Among female mice in the ApoE model, WT mice had a collagen area of 15.8%, while KO mice showed a slightly elevated collagen area of 18.5%.

Overall, no differences in plaque size or collagen amount were measured between IRG1 WT and KO mice in both genders and models.

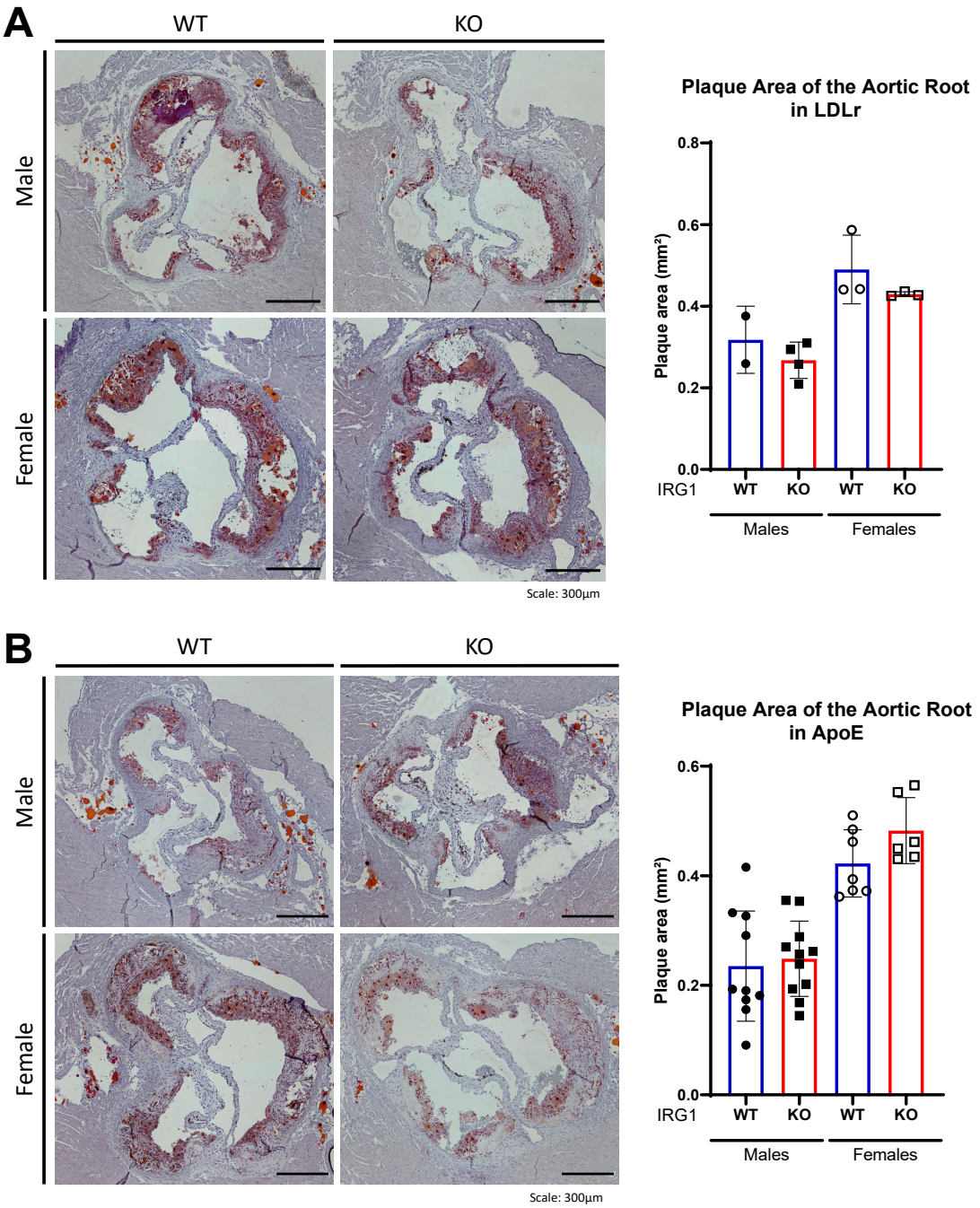

Figure 29. The plaque size does not change in the aortic root of IRG1 KO mice.

ORO staining of the aortic root of LDLr KO (A) and ApoE KO (B) IRG1 WT (blue) and KO (red) mice. Representative pictures (left), quantification (right). Scale Bar: 300µm. P value calculated by non-parametric Mann-Whitney test. **A,** Males WT n=2 KO n=4; Females WT n=3 KO=3 **B,** Males WT n=10 KO n=11; Females WT n=7 KO n=6.

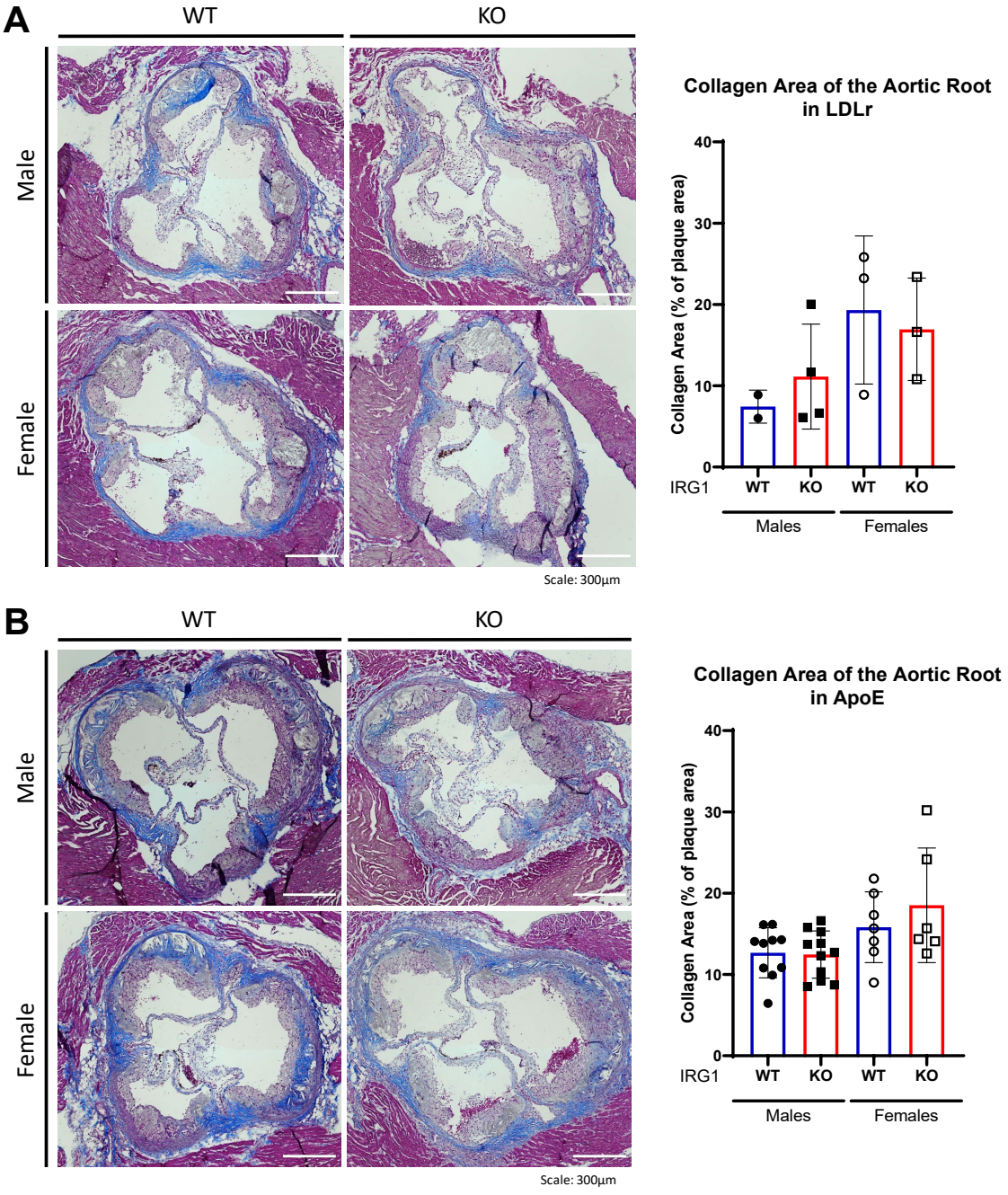

Figure 30. The collagen amount does not change in the aortic root of IRG1 KO mice.

Masson's trichrome staining of the aortic root of LDLr KO (A) and ApoE KO (B) IRG1 WT (blue) and KO (red) mice. Collagen is stained in blue and muscle in purple. Representative pictures (left), quantification (right). Scale Bar: 300µm. P value calculated by non-parametric Mann-Whitney test. **A,** Males WT n=2 KO n=4; Females WT n=3 KO=3 **B,** Males WT n=10 KO n=11; Females WT n=7 KO n=6.

Both models develop atherosclerotic plaques in the aortic root and in the aortic arch first (Ma et al., 2012; Nakashima et al., 1994). However, previous results showed increased

differences in the descending aorta in the ApoE model. The aortic arch of ApoE deficient mice was therefore stained with H&E and the plaque size was determined in the arch, and in all three connecting arteries (Figure 31, A). In both male and females, the most affected zone of the aortic arch is the brachiocephalic artery (Figure 31, B). Indeed, 0.2mm² plaques were measured in male WT mice in the brachiocephalic artery, compared to 0.1mm² in the other parts of the aortic arch. In male KO mice, the plaque area decreased to 0.12mm² in the brachiocephalic artery and was further reduced to 0.04-0.07mm² in the other parts of the aortic arch. In female mice a similar trend can be observed. Indeed, 0.34mm² are measured on average in female WT mice in the brachiocephalic artery while 0.2mm² are measured in KO mice representing a difference of 0.14mm² between IRG1 WT an KO mice. Overall, the results indicate a tendency for IRG1 deficient mice to exhibit reduced plaque development compared to WT mice, particularly in the brachiocephalic artery. The difference between WT and KO is further emphasized when the plaque area of all four zones described above is added together (Figure 31, C). In male WT mice, the total plaque area reaches 0.5mm² and it is decreased to 0.3mm² in KO mice. In female mice the total plaque area reaches 0.7mm² in WT and decreases to 0.4mm² in KO. This represents a total difference of 0.2mm² in males and 0.3mm² in females.

To further analyse the plaques, the foam cell area and collagen rich area was measured as described in the method section 4.6.4. The area without normalization is shown in Figure 31,C. However, as differences in plaque size could be measured between WT and KO mice, foam cell and collagen area are normalized to plaque size and is presented as a percentage of plaque area (Figure 31,D). No significant differences in plaque composition were measured between WT and KO in either sex. In male mice the plaques were almost equally composed of foam cells as well as collagen rich areas accounting from 40% to 47% in WT and KO. In females however, the foam cell area was slightly reduced to increase the proportion of other events like cholesterol crystal or necrotic core formation. The foam cell area accounted for 30%, and the collagen rich area for 46% regardless of genotype.

Overall, the results showed that the plaque size in the aortic arch was significantly reduced in female KO mice however, the plaques do not differ in their composition.

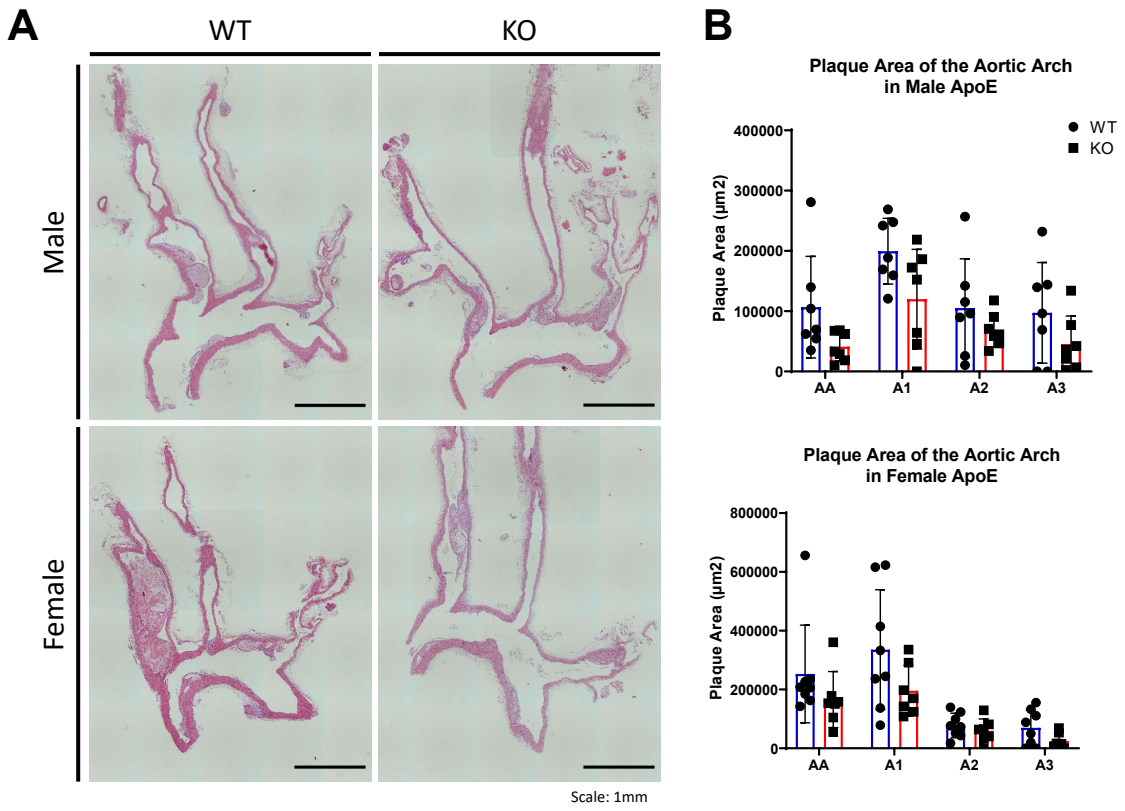
A
WT
KO
Male
Female
Scale: 1mm
B
Plaque Area of the Aortic Arch in Male ApoE
Plaque Area (µm2)
400000
300000
200000
100000
0
AA
A1
A2
A3
WT
KO
Plaque Area of the Aortic Arch in Female ApoE
Plaque Area (µm2)
800000
600000
400000
200000
0
AA
A1
A2
A3

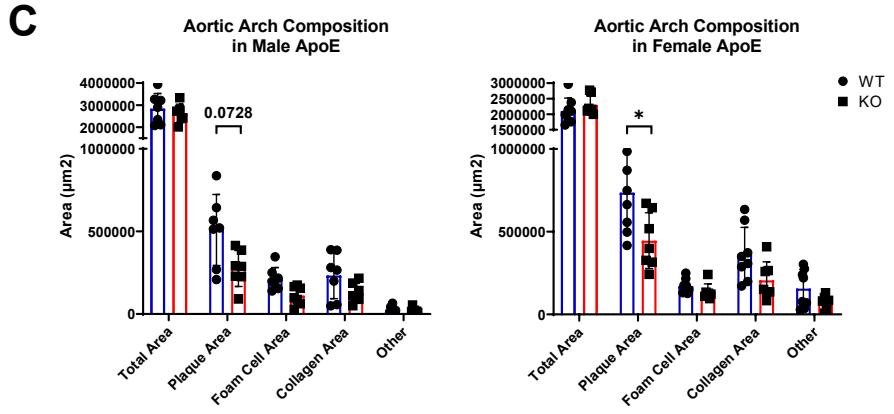
C
Aortic Arch Composition in Male ApoE
Area (µm2)
4000000
3000000
2000000
1000000
500000
0
0.0728
Total Area
Plaque Area
Foam Cell Area
Collagen Area
Other
Aortic Arch Composition in Female ApoE
Area (µm2)
3000000
2500000
2000000
1500000
1000000
500000
0
*
WT
KO
Total Area
Plaque Area
Foam Cell Area
Collagen Area
Other

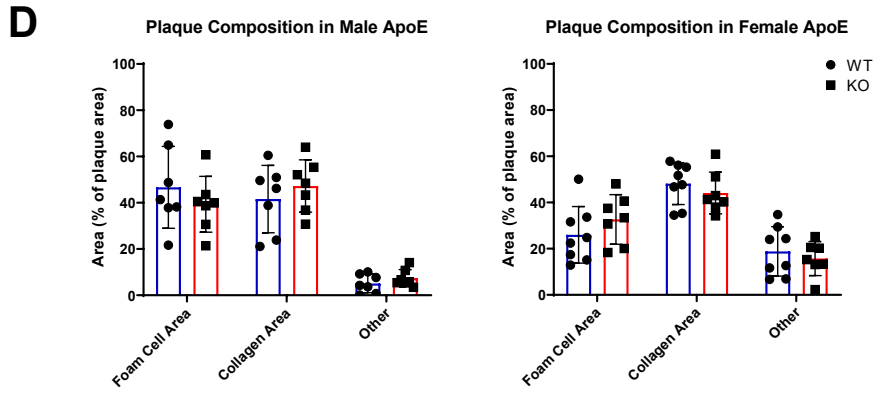
D
Plaque Composition in Male ApoE
Area (% of plaque area)
100
80
60
40
20
0
Foam Cell Area
Collagen Area
Other
Plaque Composition in Female ApoE
Area (% of plaque area)
100
80
60
40
20
0
WT
KO
Foam Cell Area
Collagen Area
Other

Figure 31. The plaque area is reduced in the aortic arch of female IRG1 ApoE deficient mice.

A, representative pictures of the H&E staining of the aortic arch of ApoE deficient IRG1 WT and KO mice fed during 12weeks a HFD. Scale bar: 1mm. **B**, Plaque area measurement in the aortic arch (AA), brachiocephalic artery (A1), left common carotid artery (A2) and left subclavian artery (A3) in IRG1 WT (blue) and KO (red) ApoE deficient mice. **C**, Area of the aortic arch, plaques, foam cells and collagen in IRG1 WT (blue) and KO (red). The category named other includes cholesterol crystals, necrotic core areas if present. **D,** Composition of plaques in the aortic arch categorised into foam cell, collagen and "other" including cholesterol crystals, necrotic core areas. **B-D**: P value calculated by non-parametric Mann-Whitney test. Males WT n=7 KO n=7; Females WT n=8 KO n=7

5.2.3. Circulating T cells are affected by IRG1 deficiency.

To further analyse potential systemic changes induced by IRG1 deletion in an inflammatory context, the immune cell landscape of IRG1 WT and KO mice has been analysed in atherosclerotic mice. The following experiments were performed with the help of Dr. Nicole Kiweler and Laura Neises.

In the LDLr model, circulating T cells represented 26% of the total CD45+ cells in male mice. Female mice showed a slightly higher percentage, with T cells representing 29% of the total CD45+ cells. No differences were measured in the proportion of CD4+ and CD8+ T cells within the total T cell population with around 50% CD4+ and 45% CD8+ in males and females of both genotypes. Interestingly a significant difference in the proportion of naïve and effector CD4+ T cells could be measured in female mice. The proportion of naïve CD4+ T cells is consistent with previous results showing a decrease in KO mice. Male mice followed a similar trend that was however not significant. No significant differences could be measured between WT an KO mice regarding the proportion of CD8+ effector and naïve cells.

Interestingly, in the ApoE model a significant difference in the proportion of circulating T cells between female WT an KO mice could be observed. In male mice a similar trend was observed. Like in the LDLr model, in the ApoE model, the proportion of CD4+ and CD8+ T cells within the total T cell population was similar between WT and KO with around 50% CD4+ cells and 35% CD8+ cells in both genders and genotypes. No significant differences could be observed between the proportion of effector and naïve CD4+ and CD8+ cells in males and females regardless of genotype.

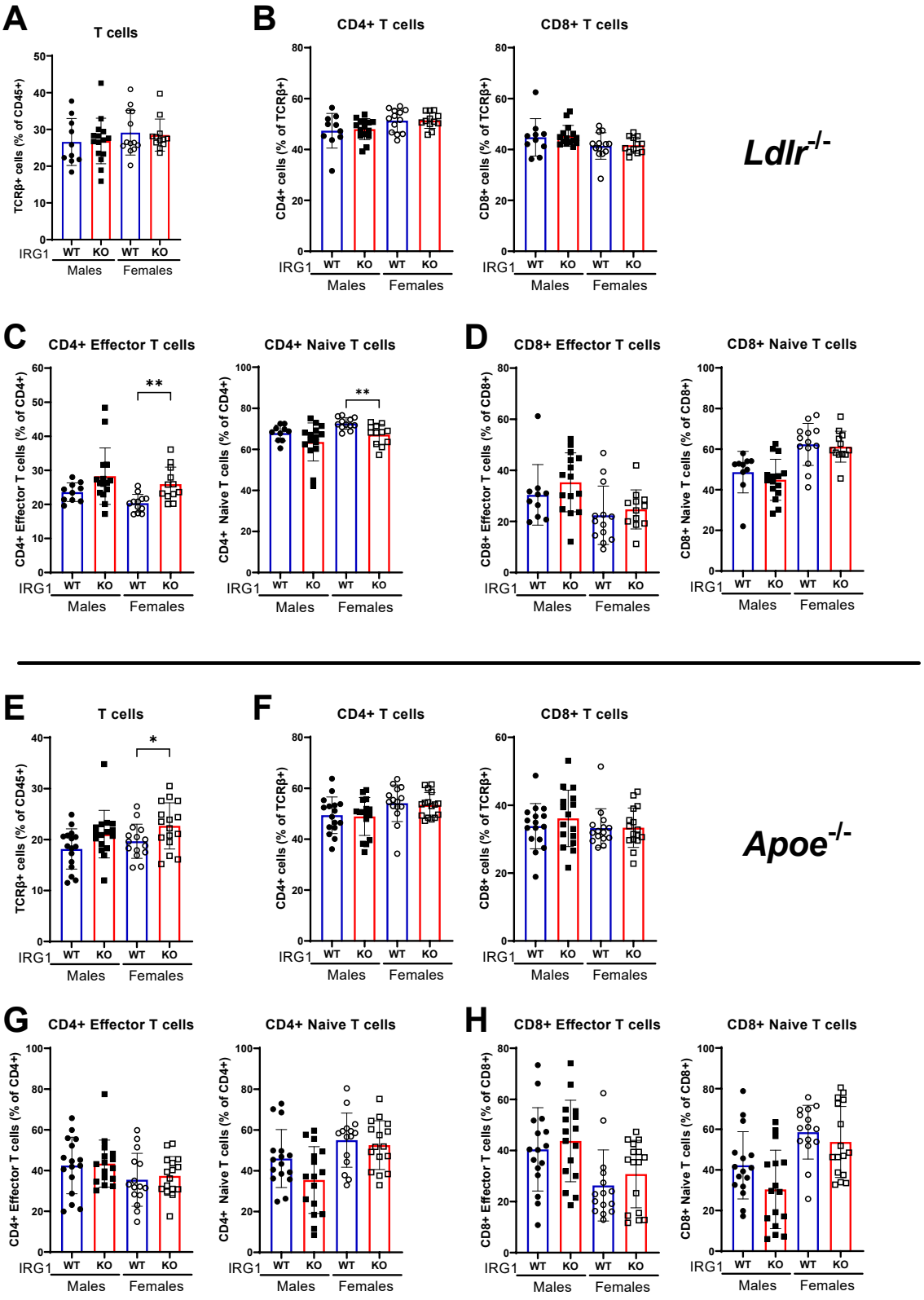

Figure 32. IRG1 deletion influences circulating T cells in female mice.

A,E, Flow cytometry analysis of the frequency of circulating T cells in the blood of LDLr KO (A), ApoE KO (E) of male and female IRG1 WT (blue) and KO (red) mice

fed for 12 weeks a HFD. **B,F,** Flow cytometry analysis of the frequency of CD4+ and CD8+ T cells within the total T cells population in the blood of LDLr KO (B), ApoE KO (F) of male and female IRG1 WT (blue) and KO (red) mice. **C,G,** Flow cytometry analysis of the frequency of CD4+ effector and naive T cells within the total T CD4+ cell population in the blood of LDLr KO (C), ApoE KO (G) of male and female IRG1 WT (blue) and KO (red) mice. **D,H,** Flow cytometry analysis of the frequency of CD8+ effector and naive T cells within the total T CD8+ cell population in the blood of LDLr KO (D), ApoE KO (H) of male and female IRG1 WT (blue) and KO (red) mice. **A-D**, Males WT n=10 KO n=15; Females WT n=13 KO n=12. **E-H,** Males WT n=16 KO n=16; Females WT n=15 KO n=16. **A-H**, *P<0.05; **P<0.01, by unpaired two-tailed Student's t-test.

The lymphocyte population was also measured in the spleen. However, no significant differences could be measured between WT and KO in both genders and models (Supplementary Figure 3 and 4).

Overall, the results show that IRG1 deletion has an impact on circulating T cells in both atherosclerosis models.

6. DISCUSSION

In this study we aimed to elucidate the function or IRG1 in atherosclerosis by assessing plaque size and severity as well as investigating the metabolic rewiring of macrophages in an inflammatory environment. Atherosclerosis is characterised by the infiltration of lipids and immune cells promoting inflammation in the plaque environment. Since macrophage metabolism can affect immune functions such as cytokine secretion, exploring the metabolic consequences of *Irg1* loss can provide insights on its role in plaques and may offer a novel entry point for potential therapeutic interventions.
Following our *ex vivo* analysis, we found new insights regarding the role of itaconate in proline and pyrimidine synthesis and we confirmed previous findings linking itaconate to NO and isocitrate dehydrogenase (IDH). Our in vivo work underlines differences between models and genders highlighting different aspects of *Irg1* loss related to cholesterol metabolism and plaque size. The major findings will be discussed in the following sections.

6.1. IFNγ changes the LPS induced metabolic rewiring.

Under inflammatory conditions, macrophages become activated and undergo a metabolic rewiring inducing a glycolytic rate, contributing to the macrophage inflammatory response. This metabolic switch is accompanied by the production of itaconate, which can dampen cytokine production and reduce ROS. By studying TLR4 and IFNGR activation, both of which are implicated in the progression of atherosclerosis (Roshan et al., 2016; Voloshyna et al., 2014), this work shows that the synergy of both stimuli induces major metabolic changes in multiple pathways.

We showed that in particular, double stimulation increases the proportion of glutamine entering the TCA cycle compared to glucose indicating that glutamine anaplerosis increases. This observation could be explained by inhibition of IDH, which catalyses the step between isocitrate and aKG in both directions (Jha et al., 2015). This inhibition partially blocks the TCA cycle, forcing citrate either to become itaconate or to be exported to the cytosol to re-enter the TCA cycle by cytosolic conversion to oxaloacetate and malate. Our D-[4-^{2}H]Glc tracing also shows that cytosolic conversion is significantly increased in double stimulated macrophages. Due to the potential IDH inhibition, macrophages use aKG as an entry point via glutamate to synthesise subsequent TCA cycle metabolites. In addition, the levels of certain TCA cycle metabolites support the IDH inhibition hypothesis: citrate levels are increased while aKG and succinate levels are decreased in double stimulated macrophages.

Another important altered pathway in double stimulated macrophages is the urea cycle. Our data demonstrate that double stimulated macrophages show increased intracellular citrulline levels compared to the single stimulated ones.

After stimulation, iNOS is expressed and leads to the production of citrulline. However, the enzyme ASS1 catalysing the citrulline to argininosuccinate reaction is expressed over time after stimulation (Qualls et al., 2012). At first, the absence of ASS1 will force the cells to use the extracellular arginine pool to sustain the NO production. Over time the newly produced citrulline can be recycle to arginine via ASS1 and ASL. In addition, more citrulline is present in the medium of double stimulated macrophages compared to single-stimulated macrophages (Benninghoff et al., 1991). This observation may be related to the intracellular citrulline levels observed in this study: LPS and IFNγ could stimulate the arginine-citrulline reaction, leading to a rapid increase in extracellular citrulline and a depletion of extracellular arginine, forcing the cell to synthesise arginine from citrulline. Interestingly, a recent study shows that citrulline regulates the Jak2-Stat1 pathway, which regulates ASS1 function. However, the same study shows that citrulline levels are depleted upon stimulation with LPS and IFNγ in BMDMs despite stable ASL and increased iNOS protein levels (Mao et al., 2022). These observations contradict those of Qualls et al. and Seim et al. showing an increase in the relative amount of citrulline in BMDMs stimulated with LPS and IFNγ compared to untreated macrophages (Qualls et al., 2012; Seim et al., 2019). The preference of macrophages to export citrulline could be explained by the energetic cost of one ATP of the citrulline-argininosuccinate reaction. Furthermore, elevated extracellular citrulline levels have been reported to have anti-inflammatory effects on macrophages and synovial fibroblasts, suggesting a potential complementary role of citrulline (Breuillard et al., 2015; Mao et al., 2022; Yamagishi et al., 2020).

Further experiments should be performed to understand how IFNγ and LPS modulate the arginine-citrulline metabolism to maintain NO production while potentially creating an anti-inflammatory environment.

6.2. Itaconate and IDH

As previously shown, IFNγ inhibits the feedback control of TLR4 signalling (Kang et al., 2019), affecting both the TCA and urea cycles. While itaconate studies have mostly been conducted in LPS stimulated macrophages, this work focuses on the effects of itaconate in LPS-IFNγ activated macrophages.

The potentially increased IDH inhibition in LPS-IFNγ macrophages has already been discussed in the previous section. Interestingly, deletion of *Irg1* appears to abolish the effects of IDH inhibition. Indeed, we showed that in the absence of IRG1, citrate does not accumulate and aKG levels increase. Furthermore, glucose labelling indicates that in KO macrophages citrate is converted to aKG and is less exported to the cytosol. The link between IDH and itaconate is further confirmed by the increase in reductive carboxylation in IRG1 KO BMDMs, indicating that aKG can be directly converted to (iso)citrate in the absence of IRG1. These observations are in line with previous studies showing that itaconate attenuates reductive carboxylation, thereby limiting its own production (Heinz et al., 2022).

In the absence of IRG1, succinate levels are reduced while aKG and fumarate levels are increased compared to WT macrophages. Low succinate levels indicate that succinate quickly converts into fumarate. Moreover, total aKG labelling from glutamine in KO and WT cells shows that glutamine anaplerosis is similar with higher cycling in KO. Thereby aKG accumulation might indicate that a-Ketoglutarate dehydrogenase or succinate thiokinase are limiting factors in the aKG-fumarate reaction. Interestingly, our data showed that the [amide-^{15}N]Gln tracer could only label glutamate in WT macrophages suggesting that the aKG to glutamate reaction catalysed by glutamate dehydrogenase mostly takes place in WT macrophages. It is believed that *in vivo*, the glutamate dehydrogenase reaction primarily proceeds in the direction of oxidative glutamate deamination, resulting in the production of aKG and free ammonium ions. However, an elevated concentration of ammonium ions and aKG within the mitochondria could potentially stimulate the biosynthesis of glutamate by the enzyme glutamate dehydrogenase (Adeva et al., 2012). Surprisingly, aKG levels are more elevated in KO BMDMs suggesting that the amount of produced ammonium inside the cell might be lower than in WT BMDMs. Another important aspect of the reaction is the necessity of NADPH which is produced by the nicotinamide nucleotide transhydrogenase (NNT). Interestingly, NNT has been described as a macrophage inflammation modulator (Ripoll et al., 2012). Aside from NNT, malic enzyme can also be a NADPH producer in the mitochondria.

Interestingly, our data underlines a different usage of NADPH between WT and IRG1 KO macrophages. Indeed, we demonstrated that WT cells use NADPH to fuel the reaction aKG to glutamate via glutamate dehydrogenase. In the absence of IRG1 however, IDH is still expressed which leads to the reductive carboxylation of aKG using NADPH (Heinz et al., 2022; Mullen et al., 2011). IRG1 deficient BMDMs can therefore use NADPH to fuel the reductive carboxylation of aKG thereby limiting NADPH availability to glutamate dehydrogenase.

6.3. LPS-IFNγ stimulation underlines the tight link between itaconate and NO

Surprisingly, while LPS and IFNγ induce enhanced changes in the TCA cycle, itaconate levels initially increase similarly in both LPS and LPS-IFNγ stimulated macrophages, but after 24 hours itaconate levels slightly decrease despite early elevated IRG1 protein levels in the double stimulated cells. This observation indicates that the IFNγ induced changes lead to a reduced flux towards itaconate. Indeed, after LPS-IFNγ stimulation, NO is produced by macrophages, which is an important metabolic regulator. NO can inhibit aconitase 2 (ACO2), the enzyme that catalyses the citrate-cis-aconitate isocitrate reaction in the mitochondria which is therefore a key enzyme in the regulation of itaconate production (Palmieri et al., 2020). The NO-induced reduction of ACO2 reduces the availability of cis-aconitate, which could be compensated by the cell by inducing higher IRG1 protein levels while limiting itaconate production. However, to test this hypothesis further experiments are required such as measuring secreted NO in LPS stimulated macrophages as well as iNOS and ACO2 protein levels. The results presented in this thesis further consolidate previous findings linking itaconate to NO and vice versa (Bailey et al., 2019). IRG1 deletion induces increased NO production and itaconate addition reduce it, showing that itaconate itself acts as an NO regulator. Due to increased NO production, citrulline levels also rise in KO macrophages and are reduced by the addition of itaconate. Furthermore, chemical iNOS blockade in WT BMDMs decreases citrate levels while increasing itaconate levels indicating that citrate is further processed to cis-aconitate by ACO2 and later itaconate.

It is important to note that iNOS blockade experiments were only performed once. In this experiment citrulline, malate, fumarate, and aspartate levels were comparable between WT and KO. As the four metabolites are closely linked to each other, changes should affect the abundancy of all four metabolites. When iNOS is inhibited, the equilibrium between the four metabolites is disrupted leading to aspartate accumulation, citrulline depletion and malate, fumarate reduction. The experiment should be repeated to strengthen the initial findings.

6.4. Itaconate remodulation of CTP synthesis and its potential links to atherosclerosis.

A novel aspect of itaconate function in macrophage metabolism described in this thesis concerns pyrimidine synthesis. Interestingly in LPS-IFNγ stimulated macrophages, WT

have increased CTP levels compared to KO macrophages. In contrast, tracing experiments show an increased *de novo* CTP synthesis in KO macrophages. The enzyme CTP synthetase (CTPS) catalysing the UTP to CTP reaction finalising the *de novo* pyrimidine pathway plays an essential role in the regulation of CTP synthesis. Our tracing data suggests that CTPS activity is possibly enhanced in KO macrophages. This enzyme is feedback inhibited by CTP itself which point towards the potential reduced activity in WT BMDMs.

Aside from the *de novo* pyrimidine pathway, cells use the salvage pathway where cytidine or uridine is re-used to make CMP or UMP. Despite the reduced CTP *de novo* synthesis WT macrophages show increased CTP levels when stimulated with LPS-IFNγ, indicating that WT rely on the salvage pathway rather than the CTP *de novo* synthesis. The enzyme catalysing UMP to UDP and CMP to CDP called CMPK2 which is essential in the salvage pathway, is a regulator of macrophages homeostasis (Arumugam et al., 2022). Interestingly, the gene encoding for CMPK2 is adjacent to the one coding for viperin (also called RSAD2). Due to their proximity in the genome, the transcription of CMPK2 induces the transcription of viperin. Viperin is induced by IFNγ in macrophages and is therefore also possibly synthetised in LPS-IFNγ macrophages (Chin and Cresswell, 2001; Hinson et al., 2010). Furthermore, a recent study shows that viperin catalyses the reaction from CTP to 3′-Deoxy-3′,4′-didehydro-cytidine triphosphate (ddhCTP) which has an antiviral activity (Lee et al., 2023). Along this line, our RNA sequencing data indicates that both CMPK2 and viperin are less expressed in KO compared to WT. This finding suggests that CTP synthesis relies more on the pyrimidine salvage pathway in the presence of itaconate, which could also lead to an increased antiviral activity via ddhCTP.

As differentiated BMDMs are not proliferating, DNA synthesis unlikely represents a CTP sink. The numerous activated transcription factors during stimulation induce RNA synthesis which also requires CTP. However, the labelling pattern as well as levels of other purines and pyrimidines is comparable between WT and KO suggesting the CTP differences between WT and KO BMDMs are not solely explainable by transcriptional changes.

CTP also serves as a cofactor in essential biochemical pathways, such as phospholipid biosynthesis, where it contributes to the formation of the intermediate molecule CDP-choline an important precursor for the phosphatidylcholine (PC) biosynthesis (Vance, 2015). A previous publication showed that inhibition of PC synthesis prevents saturated fatty acid mediated NLRP3 activation in human macrophages (Gianfrancesco et al., 2019). Moreover, as NLRP3 contributes to the progression of atherosclerosis, a reduced PC synthesis might reduce atherosclerotic plaques (Duewell et al., 2010). Studies linking PC to atherosclerosis have already been conducted on a systemic level. Indeed, impaired PC biosynthesis from

phosphatidylethanolamine, which primarily takes place in the liver, reduces atherosclerosis in ApoE$^{-/-}$ mice (Cole et al., 2011). In contrast, in LDLr$^{-/-}$ male mice dietary PC supplementation reduces atherosclerosis (Aldana-Hernández et al., 2021).
The link between itaconate, CTP and PC synthesis represents interesting starting point for future studies. Moreover, the preference for the *de novo* or salvage pathway to synthetise CTP between different cell types have already been suggested as therapeutic approach in atherosclerosis (Tanaka and Sata, 2013).
However, further experiments are required to understand how itaconate acts on CTP synthesis and if macrophages rely on PC synthesis after LPS-IFNγ stimulation.

6.5. Itaconate and Proline

Another aspect of IRG1 deletion described in this thesis are the increased proline levels. Glutamine tracing experiments showed that proline is more synthesised in KO than in WT BMDMs. However, RNA sequencing data revealed no differences in the expression of genes related to proline synthesis. In the future it should be clarified whether any changes in the protein level are observable in the proline synthesis pathway in the absence of IRG1
Aside from the upstream proline pathway, certain downstream uses could be altered due to proline accumulation. Proline is also used by cells to fuel the urea cycle. However, the absence of ornithine labelling indicates that it is not the case in inflammatory macrophages. Alternatively, proline is a constituent of several proteins such as collagen, its increased synthesis could be explained by an elevated translation in KO cells. While the RNA sequencing also shows an enrichment of genes involved in translation, the OPP assay does not reveal any differences between WT an KO cells. However, in this study OPP was only added for 30min due to its high toxicity which might prevent the measurement of long-term translation.
Interestingly, proline is one of the major constituents of collagen, which plays a crucial role in atherosclerosis (Karna et al., 2020; Rekhter, 1999). While fibroblasts produce a majority of collagen in the heart, a published study shows that macrophages can directly contribute to collagen production during heart repair (Simões et al., 2020). However, in both ApoE and LDLr models, no significant differences regarding collagen quantity in plaques could be measured, suggesting that IRG1 deletion has no impact on collagen synthesis in atherosclerosis.
Due to their collagen rich domain, certain SRs such as SR-AI or MARCO could also be affected by impaired proline metabolism. When measuring the oxLDL uptake in LPS-IFNγ stimulated macrophages a slight reduction is visible in KO BMDMs. This observation might

be induced by a lower capacity of the cells to phagocyte oxLDL due to certain oxLDL receptors such as SRs.
Finally, other proline-rich proteins impact atherosclerosis. Indeed, the proline/serine-rich coiled-coil protein 1 inhibits inflammation in macrophages and therefore delays atherosclerotic progression (Guo et al., 2018; Pan et al., 2023)

6.6. Itaconate and cholesterol metabolism

This thesis highlights a significant, total plasma cholesterol accumulation in IRG1 deficient male mice in the LDLr model accompanied by an increased weight gain. As lipoproteins are mainly metabolized by the liver, elevated plasma cholesterol levels in IRG1 KO mice could indicate that itaconate acts on hepatocytes, helping the clearance of lipids. Interestingly, Weiss and colleagues show that itaconate treatment of primary hepatocytes reduces lipid accumulation and increases their OXPHOS depending on fatty acid oxidation in a non-alcoholic fatty liver disease model (Weiss et al., 2023).
Feeding male WT mice for 12 weeks with a Western type diet composed of 40 kcal% fat, 20 kcal% fructose, 2% cholesterol, and 0.05% choline induces a non-alcoholic steatohepatitis as well as increased plasma cholesterol levels (Yang et al., 2023). The diet used in this thesis is also composed of 40 kcal% fat but lower amounts of cholesterol (0.2%) and is not composed of fructose and choline. However, as fatty acids are stored as triglycerides, the plasma triglyceride levels should be measured to further assess the lipid profile of IRG1 KO mice. Additionally, a previous study conducted on IRG1 deficient male mice in an obesity induced model also showed that KO mice were heavier after 12 weeks HFD than the WT littermates. Although, cholesterol was not measured in this study a glucose tolerance test showed that KO mice had significantly elevated blood glucose levels highlighting that IRG1 is critical for the maintenance of body weight and glucose control (Frieler et al., 2022).

Interestingly the increased plasma cholesterol phenotype observed in male LDLr IRG1 KO was not visible in the ApoE mice. ApoE is involved in the efficient hepatic uptake of lipoprotein particles by binding the LDLr or LDLr-related protein (LRP) (Mahley and Rall, 2000). ApoE deficiency results in VLDL accumulation in the blood which mostly contains triglycerides compared to cholesterol (Gisterå et al., 2022). In contrast, LDLr deficiency results in the accumulation of LDL which mostly contains cholesterol (Gisterå et al., 2022). The different lipid profiles of both models presumably explain why a cholesterol increase was only observed in the LDLr model.

The elevated plasma cholesterol levels in male LDLr IRG1 KO mice suggests that downstream cholesterol metabolism is impaired. Indeed, cholesterol is also used to synthetise bile acids which is a possibility for the body to excrete cholesterol (Craig et al., 2023). An impaired bile acid synthesis under IRG1 deficiency could also explain the elevated plasma cholesterol levels. However, our data does not explain why this phenotype is only observed in male mice.
As steroid hormones and sex hormones are cholesterol derivatives the differences between male and female mice are probably induced by a different hormonal balance (Craig et al., 2023). Interestingly certain hormones have been linked to atherosclerosis such as the dehydroepiandrosterone or testosterone (Hayashi et al., 2000; Thirumalai et al., 2015). Nevertheless, several studies showed that the addition of these hormones does not affect LDL levels (Gordon et al., 1988; Qin et al., 2020; Srinivasan et al., 2010). However, Another study showed that dehydroepiandrosterone reduces the amount of total cholesterol in rhesus monkeys (Christopher-Hennings et al., 1995).

No differences between genders are observed in WT animals regarding the total plasma concentration of cholesterol. However, the plaque size is increased in the aortic root of female mice in the ApoE and LDLr models. While certain studies showed elevated cholesterol levels in the plasma or serum of female mice (Ishibashi et al., 1993; Mansukhani et al., 2017), other studies did not show any differences between males and females (Schile, 2016; Teupser et al., 2003). These differences are probably explainable by changes in the diet composition as well as diet duration amongst the different studies. Interestingly, Teupser and colleagues used a low fat (4.3%) diet with variable cholesterol percentages and showed that the addition of 0.15% cholesterol, lead to similar elevated cholesterol levels in the plasma and development of plaques in the aortic arch, aortic root, thoracic and abdominal aorta of male and female $LDLr^{-/-}$ mice (Teupser et al., 2003). The Western diet used in this thesis contains 0.2% cholesterol which could already promote an increase in plasma cholesterol levels and plaque formation.

6.7. Itaconate and atherosclerotic plaques

Overall, no significant differences were measured regarding the plaque size in the aortic root, thoracic and abdominal aorta. However, in the aortic arch of female ApoE a significantly reduced plaque size in KO mice was measured. In males the difference was not significant, but KO mice had a slightly reduced plaque size. The results suggest that the development of atherosclerotic plaque in the aortic arch is slower when IRG1 is absent. As

a previous study showed that the lack of IL1β decreases atherosclerotic plaque size in ApoE mice (Kirii et al., 2003) and that targeting IL1β as well as NLRP3 reduces major cardiovascular risks in humans (Everett et al., 2020; Tardif et al., 2019), we presumed that itaconate promoted IL1β and NLRP3 dampening effects would be beneficial in atherosclerosis. We therefore supposed that IRG1 deficiency would increase the plaque size in mice. However, the opposite effect was observed in the aortic arch indicating that other itaconate dependent effects play an important role in atherosclerotic development. Indeed, as specified in section 6.5, oxLDL uptake in LPS-IFNγ stimulated macrophages was slightly reduced in KO BMDMs which is probably linked to the expression of certain SRs. However, the overall plaque composition in the aortic arch remained unchanged in WT and KO. By measuring cholesterol efflux, it should be clarified if itaconate influences the reverse cholesterol transport in macrophages which prevents atherosclerosis (Ohashi et al., 2005).

Since the lipidic profile of male LDLr IRG1 KO mice is elevated compared to WT mice, the plaque size in the aortic arch might be increased and not reduced in this model. Measuring the plaque size in the aortic arch of this model would clarify if the increased plasma cholesterol levels have an incidence on the plaque size. No differences were measured in the thoracic and abdominal aorta between WT and KO LDLr mice. However, the difference between WT and KO in male mice in the ApoE model is higher than in the LDLr model indicating that IRG1 deletion might have different effects on atherosclerosis in LDLr male mice compared to the ApoE deficient mice. These observation underline that the study of certain genes can result in different observation depending on the atherosclerosis mouse model and gender.

6.8. Interaction between itaconate and other immune cell types

Mainly pro-inflammatory macrophages and monocyte produce itaconate which modulates their metabolism. Interestingly, recent studies show that secreted itaconate also influences other cell types such as hepatocytes, or CD8+ T cells (Weiss et al., 2023; Zhao et al., 2022). Our data suggests that itaconate modulate the proportion of different cell populations. For example, IRG1 deficiency increases the proportion of circulating T cells in ApoE female mice. In male mice a slight but non-significant increase was also detectable. In the LDLr model, the overall proportion of T cells does not change. However, an increase in the proportion of circulating effector T CD4+ cells as well as a decrease of naïve T CD4+ cells is seen in our Flow cytometry measurement. Similarly, to the ApoE model, no significant differences are observed in male LDLr mice. As the plaque size is increased in female mice compared to male mice in both models, it is possible that inflammation is exacerbated in

females which could explain the visible immune differences in females compared to male mice.

Further experiments should be conducted to analyse the different T cell populations within the atherosclerotic plaques of IRG1 WT and KO mice. Uncovering the T cell landscape in these plaques will improve our understanding whether IRG1 deficiency induces a pro-or anti- atherogenic phenotype. According to recent studies itaconate indirectly attenuates the proliferation of T CD8+ cells by targeting aspartate and glycine/serine metabolism (Schofield et al., 2023; Zhao et al., 2022). Moreover, itaconate promotes Treg cell differentiation while inhibiting Th17 cell differentiation by inducing chromatin changes (Aso et al., 2023). In a model of vaccine induced immunity increased numbers and effector function of $CD4^+$ and $CD8^+$ T cells in IRG1 KO mice are detectable after the second challenge with the bacteria *F.tularensis* (Roberts et al., 2022). Roberts and colleagues suggest that the antigen presentation capacity of macrophages or DCs might be altered in IRG1 deficient mice. Indeed, both macrophage and DCs are antigen presenting cells and are a bridge between the innate and adaptive immune system. Interestingly a previous study linked itaconate to the immune priming function of DCs in an allergic asthma mouse model (Jaiswal et al., 2022). IRG1 KO mice presented an elevated Th2 response indicating the antigen presenting capacity of DCs is impaired in KO mice.

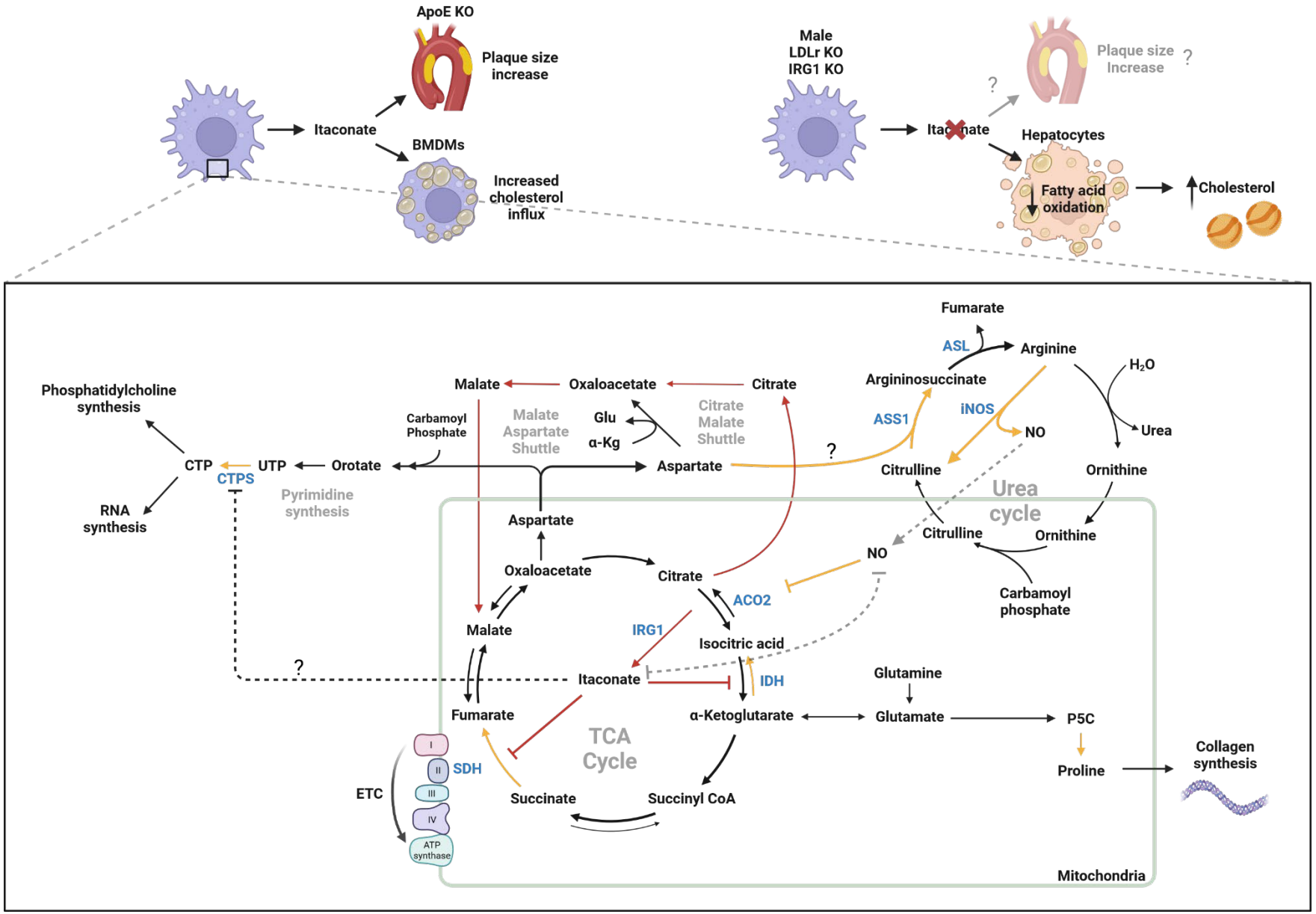
ApoE KO
Plaque size increase
Itaconate
BMDMs
Increased cholesterol influx
Male LDLr KO IRG1 KO
Plaque size Increase
Hepatocytes
Fatty acid oxidation
Cholesterol
Fumarate
ASL
Arginine
Argininosuccinate
H2O
Urea
ASS1
iNOS
NO
Citrulline
Ornithine
Urea cycle
Malate
Oxaloacetate
Citrate
Phosphatidylcholine synthesis
Carbamoyl Phosphate
Malate Aspartate Shuttle
Glu
α-Kg
Citrate Malate Shuttle
CTP
UTP
Orotate
Aspartate
CTPS
Pyrimidine synthesis
RNA synthesis
Aspartate
Oxaloacetate
Citrate
ACO2
Malate
IRG1
Isocitric acid
Itaconate
IDH
Glutamine
Fumarate
α-Ketoglutarate
Glutamate
P5C
Proline
Collagen synthesis
TCA Cycle
SDH
ETC
Succinate
Succinyl CoA
ATP synthase
Mitochondria

Figure 33. Graphical summary.

After LPS-IFNγ stimulation, itaconate promotes citrate export to the cytosol which re-enters the TCA cycle via malate. Itaconate mediated IDH inhibition reduces the reductive carboxylation route in the TCA cycle thereby limiting its own synthesis. Itaconate also slightly reduces NO synthesis which inhibits ACO2 and therefore itaconate production. The absence of itaconate in IRG1 deficient cells promotes proline synthesis as well as CTP de novo synthesis. Both metabolites have important roles in atherosclerosis as they contribute to collagen and phosphatidylcholine synthesis respectively. Certain aspects need to be further assessed such as the potential itaconate-induced CTPS or ASS1 inhibition. Itaconate seems to promotes atherosclerosis *in vivo* in the ApoE model and increases cholesterol influx *in vitro*. In male LDLr KO mice itaconate maintains cholesterol levels by potentially increasing the fatty acid oxidation of hepatic cells. Interestingly, in this model itaconate probably promotes a plaque size decrease. The red lines represent upregulated reactions in IRG1 WT mice and yellow lines represent upregulated reactions in IRG1 KO mice. Enzymes are written in blue.

7. CONCLUSION AND PERSPECTIVES

My thesis shows that the LPS-IFNγ stimulation amplifies itaconate driven metabolic changes in BMDMs, consolidating previous findings linking itaconate to NO and IDH. Moreover, new insights are gained regarding the role of itaconate in proline as well as in pyrimidine synthesis. Our *in vivo* data shows that IRG1 has little to no impact on plaque size in atherosclerosis. However, we could show that cholesterol metabolism is affected by *irg1* deficiency confirming that itaconate influences lipid metabolism where it could have atheroprotective effects. Indeed, itaconate interacts with hepatocytes and promotes fatty acid clearance which positively influences conditions such as fatty liver disease (Weiss et al., 2023). Overall, this work underscores the importance to study the effects of a gene of interest in both genders as certain observed phenotypes are gender specific. Such observations are critical when extrapolating findings to a broader context, as gender-related differences in lipid metabolism, as seen in humans, should not be overlooked (Mittendorfer, 2005; Palmisano et al., 2018; Williams, 2004).

LPS-IFNγ stimulation models the proinflammatory environment of plaques containing IFNγ-secreting Th1 cells and reflects the observed TLR4 activation of macrophages in plaques. However, this work focused on early time points (24 h) after stimulation, whereas the metabolic landscape of macrophages changes drastically after long-term exposure (Seim et al., 2019). Therefore, studying the long-term stimulation or priming effects would provide deeper insights into the impact of IRG1 on macrophage metabolism, especially in the context of chronic inflammation or trained immunity. Furthermore, studying the effect of other pro-atherogenic stimuli, such as modified LDL and saturated fatty acids, on macrophages could help us to decipher other affected pathways and point towards other functions of IRG1.

In this work, we investigated the foam cell area, collagen content and the plaque size of atherosclerotic mice. Further experiments measuring macrophage plaque infiltration, T cell infiltration or necrotic core size should be conducted to give more insights on plaque composition and therefore on plaque stage or stability. Moreover, the observed difference in circulating T cells point towards a role of IRG1 in the antigen presentation. As DCs are major APCs and as they can derive from monocytes which can express *Irg1*, investigating their antigen present functions towards T cell in the presence or absence of IRG1 could be of high interest.

Even though our results on plaque size indicate that itaconate could be pro-atherogenic, the itaconate derivatives DI or 4OI are known to have additional effects compared to itaconate. For example DI reduces the IL-6 secretion of cells via the ATF3-IκBζ pathway (Bambouskova et al., 2018; Swain et al., 2020). Injection of itaconate derivatives such as 4OI or DI in atherosclerotic mice could therefore have other effects than physiologic itaconate and may indicate whether itaconate derivative can serve as therapeutic agent in atherosclerosis.

Investigating the implications of itaconate in disorders associated with metabolic alterations, such as obesity and diabetes, may offer further insights into the role of itaconate in lipid metabolism and inflammation. Additionally, investigating the role of itaconate in macrophage related autoimmune disease such as Systemic Lupus Erythematosus, systemic sclerosis, rheumatoid arthritis, or primary biliary cholangitis will further elucidate potential new therapeutic aspects of itaconate. Interestingly, the presence of itaconate was measured in the plasma of rheumatoid arthritis patients after treatment with conventional disease-modifying anti-rheumatic drug linking physiologic itaconate production to the resolution of an inflammatory disease in humans (Daly et al., 2020). Targeting the immune system with itaconate could therefore be beneficial in rheumatoid arthritis which is also linked to an elevated risk of CAD development (Crowson et al., 2013).

Collectively, these multifaceted findings contribute to our expanding knowledge of the role of itaconate in immunometabolism and its potential therapeutic applications in various diseases.

8. REFERENCES

Adeva, M.M., Souto, G., Blanco, N., Donapetry, C., 2012. Ammonium metabolism in humans. Metabolism. 61, 1495–1511. https://doi.org/10.1016/j.metabol.2012.07.007

Aldana-Hernández, P., Azarcoya-Barrera, J., van der Veen, J.N., Leonard, K.-A., Zhao, Y.-Y., Nelson, R., Goruk, S., Field, C.J., Curtis, J.M., Richard, C., Jacobs, R.L., 2021. Dietary phosphatidylcholine supplementation reduces atherosclerosis in Ldlr-/- male mice2. J. Nutr. Biochem. 92, 108617. https://doi.org/10.1016/j.jnutbio.2021.108617

Alfaddagh, A., Martin, S.S., Leucker, T.M., Michos, E.D., Blaha, M.J., Lowenstein, C.J., Jones, S.R., Toth, P.P., 2020. Inflammation and cardiovascular disease: From mechanisms to therapeutics. Am. J. Prev. Cardiol. 4, 100130. https://doi.org/10.1016/j.ajpc.2020.100130

Alquraini, A., El Khoury, J., 2020. Scavenger receptors. Curr. Biol. CB 30, R790–R795. https://doi.org/10.1016/j.cub.2020.05.051

Amento, E.P., Ehsani, N., Palmer, H., Libby, P., 1991. Cytokines and growth factors positively and negatively regulate interstitial collagen gene expression in human vascular smooth muscle cells. Arterioscler. Thromb. J. Vasc. Biol. 11, 1223–1230. https://doi.org/10.1161/01.atv.11.5.1223

Anderson, K.V., Bokla, L., Nüsslein-Volhard, C., 1985. Establishment of dorsal-ventral polarity in the Drosophila embryo: the induction of polarity by the Toll gene product. Cell 42, 791–798. https://doi.org/10.1016/0092-8674(85)90275-2

Anichkov, N.M., Chalatov, S.S., 1983. Classics in arteriosclerosis research: On experimental cholesterin steatosis and its significance in the origin of some pathological processes by N. Anitschkow and S. Chalatow, translated by Mary Z. Pelias, 1913. Arterioscler. Dallas Tex 3, 178–182.

Arango Duque, G., Descoteaux, A., 2014. Macrophage cytokines: involvement in immunity and infectious diseases. Front. Immunol. 5, 491. https://doi.org/10.3389/fimmu.2014.00491

Aras, S., Zaidi, M.R., 2017. TAMeless traitors: macrophages in cancer progression and metastasis. Br. J. Cancer 117, 1583–1591. https://doi.org/10.1038/bjc.2017.356

Areschoug, T., Gordon, S., 2009. Scavenger receptors: role in innate immunity and microbial pathogenesis. Cell. Microbiol. 11, 1160–1169. https://doi.org/10.1111/j.1462-5822.2009.01326.x

Arumugam, P., Chauhan, M., Rajeev, T., Chakraborty, R., Bisht, K., Madan, M., Shankaran, D., Ramalingam, S., Gandotra, S., Rao, V., 2022. The mitochondrial gene-CMPK2 functions as a rheostat for macrophage homeostasis. Front. Immunol. 13, 935710. https://doi.org/10.3389/fimmu.2022.935710

Aso, K., Kono, M., Kanda, M., Kudo, Y., Sakiyama, K., Hisada, R., Karino, K., Ueda, Y., Nakazawa, D., Fujieda, Y., Kato, M., Amengual, O., Atsumi, T., 2023. Itaconate ameliorates autoimmunity by modulating T cell imbalance via metabolic and epigenetic reprogramming. Nat. Commun. 14, 984. https://doi.org/10.1038/s41467-023-36594-x

Bailey, J.D., Diotallevi, M., Nicol, T., McNeill, E., Shaw, A., Chuaiphichai, S., Hale, A., Starr, A., Nandi, M., Stylianou, E., McShane, H., Davis, S., Fischer, R., Kessler, B.M., McCullagh, J., Channon, K.M., Crabtree, M.J., 2019. Nitric Oxide Modulates Metabolic Remodeling in Inflammatory Macrophages through TCA Cycle Regulation and Itaconate Accumulation. Cell Rep. 28, 218-230.e7. https://doi.org/10.1016/j.celrep.2019.06.018

Bambouskova, M., Gorvel, L., Lampropoulou, V., Sergushichev, A., Loginicheva, E., Johnson, K., Korenfeld, D., Mathyer, M.E., Kim, H., Huang, L.-H., Duncan, D., Bregman, H., Keskin, A., Santeford, A., Apte, R.S., Sehgal, R., Johnson, B., Amarasinghe, G.K., Soares, M.P., Satoh, T., Akira, S., Hai, T., de Guzman Strong,

C., Auclair, K., Roddy, T.P., Biller, S.A., Jovanovic, M., Klechevsky, E., Stewart, K.M., Randolph, G.J., Artyomov, M.N., 2018. Electrophilic properties of itaconate and derivatives regulate the IκBζ-ATF3 inflammatory axis. Nature 556, 501–504. https://doi.org/10.1038/s41586-018-0052-z

Baup, S., 1836. Ueber eine neue Pyrogen-Citronensäure, und über Benennung der Pyrogen-Säuren überhaupt. Ann. Pharm. 19, 29–38. https://doi.org/10.1002/jlac.18360190107

Benninghoff, B., Lehmann, V., Eck, H.P., Dröge, W., 1991. Production of citrulline and ornithine by interferon-gamma treated macrophages. Int. Immunol. 3, 413–417. https://doi.org/10.1093/intimm/3.5.413

Blessing, E., Campbell, L.A., Rosenfeld, M.E., Chough, N., Kuo, C.C., 2001. Chlamydia pneumoniae infection accelerates hyperlipidemia induced atherosclerotic lesion development in C57BL/6J mice. Atherosclerosis 158, 13–17. https://doi.org/10.1016/s0021-9150(00)00758-9

Botts, S.R., Fish, J.E., Howe, K.L., 2021. Dysfunctional Vascular Endothelium as a Driver of Atherosclerosis: Emerging Insights Into Pathogenesis and Treatment. Front. Pharmacol. 12, 787541. https://doi.org/10.3389/fphar.2021.787541

Braun, A., Trigatti, B.L., Post, M.J., Sato, K., Simons, M., Edelberg, J.M., Rosenberg, R.D., Schrenzel, M., Krieger, M., 2002. Loss of SR-BI expression leads to the early onset of occlusive atherosclerotic coronary artery disease, spontaneous myocardial infarctions, severe cardiac dysfunction, and premature death in apolipoprotein E-deficient mice. Circ. Res. 90, 270–276. https://doi.org/10.1161/hh0302.104462

Breslow, J.L., 1996. Mouse models of atherosclerosis. Science 272, 685–688. https://doi.org/10.1126/science.272.5262.685

Breuillard, C., Bonhomme, S., Couderc, R., Cynober, L., De Bandt, J.-P., 2015. In vitro anti-inflammatory effects of citrulline on peritoneal macrophages in Zucker diabetic fatty rats. Br. J. Nutr. 113, 120–124. https://doi.org/10.1017/S0007114514002086

Brown, M.S., Goldstein, J.L., 1983. Lipoprotein metabolism in the macrophage: implications for cholesterol deposition in atherosclerosis. Annu. Rev. Biochem. 52, 223–261. https://doi.org/10.1146/annurev.bi.52.070183.001255

Cahill, P.A., Redmond, E.M., 2016. Vascular endothelium - Gatekeeper of vessel health. Atherosclerosis 248, 97–109. https://doi.org/10.1016/j.atherosclerosis.2016.03.007

Campbell, L.A., Rosenfeld, M.E., 2015. Infection and Atherosclerosis Development. Arch. Med. Res. 46, 339–350. https://doi.org/10.1016/j.arcmed.2015.05.006

Caruso, R., Warner, N., Inohara, N., Núñez, G., 2014. NOD1 and NOD2: signaling, host defense, and inflammatory disease. Immunity 41, 898–908. https://doi.org/10.1016/j.immuni.2014.12.010

Castelli, W.P., Anderson, K., Wilson, P.W., Levy, D., 1992. Lipids and risk of coronary heart disease. The Framingham Study. Ann. Epidemiol. 2, 23–28. https://doi.org/10.1016/1047-2797(92)90033-m

Chavakis, T., 2022. Immunometabolism: Where Immunology and Metabolism Meet. J. Innate Immun. 14, 1–3. https://doi.org/10.1159/000521305

Chen, J., Xiang, X., Nie, L., Guo, X., Zhang, F., Wen, C., Xia, Y., Mao, L., 2022. The emerging role of Th1 cells in atherosclerosis and its implications for therapy. Front. Immunol. 13, 1079668. https://doi.org/10.3389/fimmu.2022.1079668

Chen, L., Deng, H., Cui, H., Fang, J., Zuo, Z., Deng, J., Li, Y., Wang, X., Zhao, L., 2018. Inflammatory responses and inflammation-associated diseases in organs. Oncotarget 9, 7204–7218. https://doi.org/10.18632/oncotarget.23208

Chin, K.C., Cresswell, P., 2001. Viperin (cig5), an IFN-inducible antiviral protein directly induced by human cytomegalovirus. Proc. Natl. Acad. Sci. U. S. A. 98, 15125–15130. https://doi.org/10.1073/pnas.011593298

Chinetti-Gbaguidi, G., Colin, S., Staels, B., 2015. Macrophage subsets in atherosclerosis. Nat. Rev. Cardiol. 12, 10–17. https://doi.org/10.1038/nrcardio.2014.173

Chistiakov, D.A., Killingsworth, M.C., Myasoedova, V.A., Orekhov, A.N., Bobryshev, Y.V., 2017. CD68/macrosialin: not just a histochemical marker. Lab. Investig. J. Tech. Methods Pathol. 97, 4–13. https://doi.org/10.1038/labinvest.2016.116

Christopher-Hennings, J., Kurzman, I.D., Haffa, A.L., Kemnitz, J.W., Macewen, E.G., 1995. The effect of high fat diet and dehydroepiandrosterone (DHEA) administration in the rhesus monkey. Vivo Athens Greece 9, 415–420.

Cole, L.K., Dolinsky, V.W., Dyck, J.R.B., Vance, D.E., 2011. Impaired phosphatidylcholine biosynthesis reduces atherosclerosis and prevents lipotoxic cardiac dysfunction in ApoE-/- Mice. Circ. Res. 108, 686–694. https://doi.org/10.1161/CIRCRESAHA.110.238691

Cooper, G.M., 2000. The Mechanism of Oxidative Phosphorylation, in: The Cell: A Molecular Approach. 2nd Edition. Sinauer Associates.

Cordes, T., Wallace, M., Michelucci, A., Divakaruni, A.S., Sapcariu, S.C., Sousa, C., Koseki, H., Cabrales, P., Murphy, A.N., Hiller, K., Metallo, C.M., 2016. Immunoresponsive Gene 1 and Itaconate Inhibit Succinate Dehydrogenase to Modulate Intracellular Succinate Levels. J. Biol. Chem. 291, 14274–14284. https://doi.org/10.1074/jbc.M115.685792

Craig, M., Yarrarapu, S.N.S., Dimri, M., 2023. Biochemistry, Cholesterol, in: StatPearls. StatPearls Publishing, Treasure Island (FL).

Crasso, Gust.Ludw., 1840. Untersuchungen über das Verhalten der Citronsäure in höherer Temperatur und die daraus hervorgehenden Produkte. Justus Liebigs Ann. Chem. 34, 53–84. https://doi.org/10.1002/jlac.18400340104

Crowson, C.S., Liao, K.P., Davis, J.M., Solomon, D.H., Matteson, E.L., Knutson, K.L., Hlatky, M.A., Gabriel, S.E., 2013. Rheumatoid arthritis and cardiovascular disease. Am. Heart J. 166, 622-628.e1. https://doi.org/10.1016/j.ahj.2013.07.010

Daly, R., Blackburn, G., Best, C., Goodyear, C.S., Mudaliar, M., Burgess, K., Stirling, A., Porter, D., McInnes, I.B., Barrett, M.P., Dale, J., 2020. Changes in Plasma Itaconate Elevation in Early Rheumatoid Arthritis Patients Elucidates Disease Activity Associated Macrophage Activation. Metabolites 10, 241. https://doi.org/10.3390/metabo10060241

Davies, M.J., Gordon, J.L., Gearing, A.J., Pigott, R., Woolf, N., Katz, D., Kyriakopoulos, A., 1993. The expression of the adhesion molecules ICAM-1, VCAM-1, PECAM, and E-selectin in human atherosclerosis. J. Pathol. 171, 223–229. https://doi.org/10.1002/path.1711710311

De Caterina, R., Libby, P., Peng, H.B., Thannickal, V.J., Rajavashisth, T.B., Gimbrone, M.A., Shin, W.S., Liao, J.K., 1995. Nitric oxide decreases cytokine-induced endothelial activation. Nitric oxide selectively reduces endothelial expression of adhesion molecules and proinflammatory cytokines. J. Clin. Invest. 96, 60–68. https://doi.org/10.1172/JCI118074

Delbrouck, C., Kiweler, N., Chen, O., Pozdeev, V.I., Haase, L., Neises, L., Oudin, A., Fouquier d'Hérouël, A., Shen, R., Schlicker, L., Halder, R., Lesur, A., Schuster, A., Lorenz, N.I., Jaeger, C., Feucherolles, M., Frache, G., Szpakowska, M., Chevigne, A., Ronellenfitsch, M.W., Moussay, E., Piraud, M., Skupin, A., Schulze, A., Niclou, S.P., Letellier, E., Meiser, J., 2023. Formate promotes invasion and metastasis in reliance on lipid metabolism. Cell Rep. 42, 113034. https://doi.org/10.1016/j.celrep.2023.113034

Duewell, P., Kono, H., Rayner, K.J., Sirois, C.M., Vladimer, G., Bauernfeind, F.G., Abela, G.S., Franchi, L., Nuñez, G., Schnurr, M., Espevik, T., Lien, E., Fitzgerald, K.A., Rock, K.L., Moore, K.J., Wright, S.D., Hornung, V., Latz, E., 2010. NLRP3 inflammasomes are required for atherogenesis and activated by cholesterol crystals. Nature 464, 1357–1361. https://doi.org/10.1038/nature08938

Eberhardt, N., Giannarelli, C., 2022. How Single-Cell Technologies Have Provided New Insights Into Atherosclerosis. Arterioscler. Thromb. Vasc. Biol. 42, 243–252. https://doi.org/10.1161/ATVBAHA.121.315849

ElAzzouny, M., Tom, C.T.M.B., Evans, C.R., Olson, L.L., Tanga, M.J., Gallagher, K.A., Martin, B.R., Burant, C.F., 2017. Dimethyl Itaconate Is Not Metabolized into Itaconate Intracellularly. J. Biol. Chem. 292, 4766–4769. https://doi.org/10.1074/jbc.C117.775270

Eligini, S., Gianazza, E., Mallia, A., Ghilardi, S., Banfi, C., 2023. Macrophage Phenotyping in Atherosclerosis by Proteomics. Int. J. Mol. Sci. 24, 2613. https://doi.org/10.3390/ijms24032613

El-Zayat, S.R., Sibaii, H., Mannaa, F.A., 2019. Toll-like receptors activation, signaling, and targeting: an overview. Bull. Natl. Res. Cent. 43. https://doi.org/10.1186/s42269-019-0227-2

Emini Veseli, B., Perrotta, P., De Meyer, G.R.A., Roth, L., Van der Donckt, C., Martinet, W., De Meyer, G.R.Y., 2017. Animal models of atherosclerosis. Eur. J. Pharmacol. 816, 3–13. https://doi.org/10.1016/j.ejphar.2017.05.010

Everett, B.M., MacFadyen, J.G., Thuren, T., Libby, P., Glynn, R.J., Ridker, P.M., 2020. Inhibition of Interleukin-1β and Reduction in Atherothrombotic Cardiovascular Events in the CANTOS Trial. J. Am. Coll. Cardiol. 76, 1660–1670. https://doi.org/10.1016/j.jacc.2020.08.011

Fatkhullina, A.R., Peshkova, I.O., Koltsova, E.K., 2016. The Role of Cytokines in the Development of Atherosclerosis. Biochem. Biokhimiia 81, 1358–1370. https://doi.org/10.1134/S0006297916110134

Fernandez, D.M., Rahman, A.H., Fernandez, N.F., Chudnovskiy, A., Amir, E.-A.D., Amadori, L., Khan, N.S., Wong, C.K., Shamailova, R., Hill, C.A., Wang, Z., Remark, R., Li, J.R., Pina, C., Faries, C., Awad, A.J., Moss, N., Bjorkegren, J.L.M., Kim-Schulze, S., Gnjatic, S., Ma'ayan, A., Mocco, J., Faries, P., Merad, M., Giannarelli, C., 2019. Single-cell immune landscape of human atherosclerotic plaques. Nat. Med. https://doi.org/10.1038/s41591-019-0590-4

Frieler, R.A., Vigil, T.M., Song, J., Leung, C., Goldstein, D.R., Lumeng, C.N., Mortensen, R.M., 2022. Aconitate decarboxylase 1 regulates glucose homeostasis and obesity in mice. Obes. Silver Spring Md 30, 1818–1830. https://doi.org/10.1002/oby.23509

Galkina, E., Ley, K., 2007. Vascular adhesion molecules in atherosclerosis. Arterioscler. Thromb. Vasc. Biol. 27, 2292–2301. https://doi.org/10.1161/ATVBAHA.107.149179

Geeraerts, X., Bolli, E., Fendt, S.-M., Van Ginderachter, J.A., 2017. Macrophage Metabolism As Therapeutic Target for Cancer, Atherosclerosis, and Obesity. Front. Immunol. 8, 289. https://doi.org/10.3389/fimmu.2017.00289

Getz, G.S., Reardon, C.A., 2012. Animal models of atherosclerosis. Arterioscler. Thromb. Vasc. Biol. 32, 1104–1115. https://doi.org/10.1161/ATVBAHA.111.237693

Gianfrancesco, M.A., Dehairs, J., L'homme, L., Herinckx, G., Esser, N., Jansen, O., Habraken, Y., Lassence, C., Swinnen, J.V., Rider, M.H., Piette, J., Paquot, N., Legrand-Poels, S., 2019. Saturated fatty acids induce NLRP3 activation in human macrophages through K+ efflux resulting from phospholipid saturation and Na, K-ATPase disruption. Biochim. Biophys. Acta Mol. Cell Biol. Lipids 1864, 1017–1030. https://doi.org/10.1016/j.bbalip.2019.04.001

Gisterå, A., Ketelhuth, D.F.J., Malin, S.G., Hansson, G.K., 2022. Animal Models of Atherosclerosis-Supportive Notes and Tricks of the Trade. Circ. Res. 130, 1869–1887. https://doi.org/10.1161/CIRCRESAHA.122.320263

Global Health Estimates, W., 2020. Global Health Estimates 2020: Deaths by Cause, Age, Sex, by Country and by Region, 2000-2019. Geneva, World Health Organization; 2020.

Go, G.-W., Mani, A., 2012. Low-density lipoprotein receptor (LDLR) family orchestrates cholesterol homeostasis. Yale J. Biol. Med. 85, 19–28.

Goettsch, C., Hutcheson, J.D., Hagita, S., Rogers, M.A., Creager, M.D., Pham, T., Choi, J., Mlynarchik, A.K., Pieper, B., Kjolby, M., Aikawa, M., Aikawa, E., 2016. A single injection of gain-of-function mutant PCSK9 adeno-associated virus vector induces cardiovascular calcification in mice with no genetic modification. Atherosclerosis 251, 109–118. https://doi.org/10.1016/j.atherosclerosis.2016.06.011

Goldstein, J.L., Brown, M.S., 2009. The LDL receptor. Arterioscler. Thromb. Vasc. Biol. 29, 431–438. https://doi.org/10.1161/ATVBAHA.108.179564
Goldstein, J.L., Ho, Y.K., Basu, S.K., Brown, M.S., 1979. Binding site on macrophages that mediates uptake and degradation of acetylated low density lipoprotein, producing massive cholesterol deposition. Proc. Natl. Acad. Sci. U. S. A. 76, 333–337. https://doi.org/10.1073/pnas.76.1.333
Gordon, G.B., Bush, D.E., Weisman, H.F., 1988. Reduction of atherosclerosis by administration of dehydroepiandrosterone. A study in the hypercholesterolemic New Zealand white rabbit with aortic intimal injury. J. Clin. Invest. 82, 712–720. https://doi.org/10.1172/JCI113652
Gordon, T., Castelli, W.P., Hjortland, M.C., Kannel, W.B., Dawber, T.R., 1977. High density lipoprotein as a protective factor against coronary heart disease. The Framingham Study. Am. J. Med. 62, 707–714. https://doi.org/10.1016/0002-9343(77)90874-9
Granger, D.N., Senchenkova, E., 2010. Historical Perspectives, in: Inflammation and the Microcirculation. Morgan & Claypool Life Sciences.
Guo, K., Hu, L., Xi, D., Zhao, J., Liu, J., Luo, T., Ma, Y., Lai, W., Guo, Z., 2018. PSRC1 overexpression attenuates atherosclerosis progression in apoE-/- mice by modulating cholesterol transportation and inflammation. J. Mol. Cell. Cardiol. 116, 69–80. https://doi.org/10.1016/j.yjmcc.2018.01.013
Hamamdzic, D., Wilensky, R.L., 2013. Porcine models of accelerated coronary atherosclerosis: role of diabetes mellitus and hypercholesterolemia. J. Diabetes Res. 2013, 761415. https://doi.org/10.1155/2013/761415
Harris, T.A., Yamakuchi, M., Ferlito, M., Mendell, J.T., Lowenstein, C.J., 2008. MicroRNA-126 regulates endothelial expression of vascular cell adhesion molecule 1. Proc. Natl. Acad. Sci. U. S. A. 105, 1516–1521. https://doi.org/10.1073/pnas.0707493105
Hayashi, T., Esaki, T., Muto, E., Kano, H., Asai, Y., Thakur, N.K., Sumi, D., Jayachandran, M., Iguchi, A., 2000. Dehydroepiandrosterone retards atherosclerosis formation through its conversion to estrogen: the possible role of nitric oxide. Arterioscler. Thromb. Vasc. Biol. 20, 782–792. https://doi.org/10.1161/01.atv.20.3.782
Heinz, A., Nonnenmacher, Y., Henne, A., Khalil, M.-A., Bejkollari, K., Dostert, C., Hosseini, S., Goldmann, O., He, W., Palorini, R., Verschueren, C., Korte, M., Chiaradonna, F., Medina, E., Brenner, D., Hiller, K., 2022. Itaconate controls its own synthesis via feedback-inhibition of reverse TCA cycle activity at IDH2. Biochim. Biophys. Acta Mol. Basis Dis. 1868, 166530. https://doi.org/10.1016/j.bbadis.2022.166530
Henriksen, T., Mahoney, E.M., Steinberg, D., 1981. Enhanced macrophage degradation of low density lipoprotein previously incubated with cultured endothelial cells: recognition by receptors for acetylated low density lipoproteins. Proc. Natl. Acad. Sci. U. S. A. 78, 6499–6503. https://doi.org/10.1073/pnas.78.10.6499
Hinson, E.R., Joshi, N.S., Chen, J.H., Rahner, C., Jung, Y.W., Wang, X., Kaech, S.M., Cresswell, P., 2010. Viperin is highly induced in neutrophils and macrophages during acute and chronic lymphocytic choriomeningitis virus infection. J. Immunol. Baltim. Md 1950 184, 5723–5731. https://doi.org/10.4049/jimmunol.0903752
Hogarth, C.A., Roy, A., Ebert, D.L., 2003. Genomic evidence for the absence of a functional cholesteryl ester transfer protein gene in mice and rats. Comp. Biochem. Physiol. B Biochem. Mol. Biol. 135, 219–229. https://doi.org/10.1016/s1096-4959(03)00046-0
Hong, Y.M., 2010. Atherosclerotic cardiovascular disease beginning in childhood. Korean Circ. J. 40, 1–9. https://doi.org/10.4070/kcj.2010.40.1.1
Hooftman, A., Angiari, S., Hester, S., Corcoran, S.E., Runtsch, M.C., Ling, C., Ruzek, M.C., Slivka, P.F., McGettrick, A.F., Banahan, K., Hughes, M.M., Irvine, A.D., Fischer, R., O'Neill, L.A.J., 2020. The Immunomodulatory Metabolite Itaconate Modifies NLRP3 and Inhibits Inflammasome Activation. Cell Metab. https://doi.org/10.1016/j.cmet.2020.07.016
Hosen, M.R., Goody, P.R., Zietzer, A., Nickenig, G., Jansen, F., 2020. MicroRNAs As Master Regulators of Atherosclerosis: From Pathogenesis to Novel Therapeutic

Options. Antioxid. Redox Signal. 33, 621–644. https://doi.org/10.1089/ars.2020.8107
Huang, Y., Mahley, R.W., 2014. Apolipoprotein E: structure and function in lipid metabolism, neurobiology, and Alzheimer's diseases. Neurobiol. Dis. 72 Pt A, 3–12. https://doi.org/10.1016/j.nbd.2014.08.025
Ishibashi, S., Brown, M.S., Goldstein, J.L., Gerard, R.D., Hammer, R.E., Herz, J., 1993. Hypercholesterolemia in low density lipoprotein receptor knockout mice and its reversal by adenovirus-mediated gene delivery. J. Clin. Invest. 92, 883–893. https://doi.org/10.1172/JCI116663
Ishibashi, S., Goldstein, J.L., Brown, M.S., Herz, J., Burns, D.K., 1994. Massive xanthomatosis and atherosclerosis in cholesterol-fed low density lipoprotein receptor-negative mice. J. Clin. Invest. 93, 1885–1893. https://doi.org/10.1172/JCI117179
Jaiswal, A.K., Yadav, J., Makhija, S., Mazumder, S., Mitra, A.K., Suryawanshi, A., Sandey, M., Mishra, A., 2022. Irg1/itaconate metabolic pathway is a crucial determinant of dendritic cells immune-priming function and contributes to resolute allergen-induced airway inflammation. Mucosal Immunol. 15, 301–313. https://doi.org/10.1038/s41385-021-00462-y
Jha, A.K., Huang, S.C.-C., Sergushichev, A., Lampropoulou, V., Ivanova, Y., Loginicheva, E., Chmielewski, K., Stewart, K.M., Ashall, J., Everts, B., Pearce, E.J., Driggers, E.M., Artyomov, M.N., 2015. Network integration of parallel metabolic and transcriptional data reveals metabolic modules that regulate macrophage polarization. Immunity 42, 419–430. https://doi.org/10.1016/j.immuni.2015.02.005
Jonasson, L., Holm, J., Skalli, O., Bondjers, G., Hansson, G.K., 1986. Regional accumulations of T cells, macrophages, and smooth muscle cells in the human atherosclerotic plaque. Arterioscler. Dallas Tex 6, 131–138. https://doi.org/10.1161/01.atv.6.2.131
Jung, S.-H., Lee, K.-T., 2022. Atherosclerosis by Virus Infection-A Short Review. Biomedicines 10, 2634. https://doi.org/10.3390/biomedicines10102634
Kannel, W.B., Dawber, T.R., Kagan, A., Revotskie, N., Stokes, J., 1961. Factors of risk in the development of coronary heart disease--six year follow-up experience. The Framingham Study. Ann. Intern. Med. 55, 33–50. https://doi.org/10.7326/0003-4819-55-1-33
Kany, S., Vollrath, J.T., Relja, B., 2019. Cytokines in Inflammatory Disease. Int. J. Mol. Sci. 20, 6008. https://doi.org/10.3390/ijms20236008
Karna, E., Szoka, L., Huynh, T.Y.L., Palka, J.A., 2020. Proline-dependent regulation of collagen metabolism. Cell. Mol. Life Sci. CMLS 77, 1911–1918. https://doi.org/10.1007/s00018-019-03363-3
Kawasaki, T., Kawai, T., 2014. Toll-like receptor signaling pathways. Front. Immunol. 5, 461. https://doi.org/10.3389/fimmu.2014.00461
Kim, Y.K., Shin, J.S., Nahm, M.H., 2016. NOD-Like Receptors in Infection, Immunity, and Diseases. Yonsei Med. J. 57, 5–14. https://doi.org/10.3349/ymj.2016.57.1.5
Kirii, H., Niwa, T., Yamada, Y., Wada, H., Saito, K., Iwakura, Y., Asano, M., Moriwaki, H., Seishima, M., 2003. Lack of interleukin-1beta decreases the severity of atherosclerosis in ApoE-deficient mice. Arterioscler. Thromb. Vasc. Biol. 23, 656–660. https://doi.org/10.1161/01.ATV.0000064374.15232.C3
Kolliniati, O., Ieronymaki, E., Vergadi, E., Tsatsanis, C., 2022. Metabolic Regulation of Macrophage Activation. J. Innate Immun. 14, 51–68. https://doi.org/10.1159/000516780
Kong, P., Cui, Z.-Y., Huang, X.-F., Zhang, D.-D., Guo, R.-J., Han, M., 2022. Inflammation and atherosclerosis: signaling pathways and therapeutic intervention. Signal Transduct. Target. Ther. 7, 131. https://doi.org/10.1038/s41392-022-00955-7
Konstantinov, I.E., Mejevoi, N., Anichkov, N.M., 2006. Nikolai N. Anichkov and his theory of atherosclerosis. Tex. Heart Inst. J. 33, 417–423.

Krebs, H.A., 1973. The discovery of the ornithine cycle of urea synthesis. Biochem. Educ. 1, 19–23. https://doi.org/10.1016/0307-4412(73)90048-4
Krebs, H.A., Johnson, W.A., 1937. The Role of Citric Acid in Intermediate Metabolism in Animal Tissues. Enzymologia 148–156. https://doi.org/10.4159/harvard.9780674366701.c143
Kumar, H., Kawai, T., Akira, S., 2009. Toll-like receptors and innate immunity. Biochem. Biophys. Res. Commun. 388, 621–625. https://doi.org/10.1016/j.bbrc.2009.08.062
Kuo, C.C., Shor, A., Campbell, L.A., Fukushi, H., Patton, D.L., Grayston, J.T., 1993. Demonstration of Chlamydia pneumoniae in atherosclerotic lesions of coronary arteries. J. Infect. Dis. 167, 841–849. https://doi.org/10.1093/infdis/167.4.841
Lampropoulou, V., Sergushichev, A., Bambouskova, M., Nair, S., Vincent, E.E., Loginicheva, E., Cervantes-Barragan, L., Ma, X., Huang, S.C.-C., Griss, T., Weinheimer, C.J., Khader, S., Randolph, G.J., Pearce, E.J., Jones, R.G., Diwan, A., Diamond, M.S., Artyomov, M.N., 2016. Itaconate Links Inhibition of Succinate Dehydrogenase with Macrophage Metabolic Remodeling and Regulation of Inflammation. Cell Metab. 24, 158–166. https://doi.org/10.1016/j.cmet.2016.06.004
Lee, J.H., Wood, J.M., Almo, S.C., Evans, G.B., Harris, L.D., Grove, T.L., 2023. Chemoenzymatic Synthesis of 3'-Deoxy-3',4'-didehydro-cytidine triphosphate (ddhCTP). ACS Bio Med Chem Au 3, 322–326. https://doi.org/10.1021/acsbiomedchemau.3c00014
Leick, M., Azcutia, V., Newton, G., Luscinskas, F.W., 2014. Leukocyte recruitment in inflammation: basic concepts and new mechanistic insights based on new models and microscopic imaging technologies. Cell Tissue Res. 355, 647–656. https://doi.org/10.1007/s00441-014-1809-9
Lemaitre, B., Nicolas, E., Michaut, L., Reichhart, J.M., Hoffmann, J.A., 1996. The dorsoventral regulatory gene cassette spätzle/Toll/cactus controls the potent antifungal response in Drosophila adults. Cell 86, 973–983. https://doi.org/10.1016/s0092-8674(00)80172-5
Levin, R., Grinstein, S., Canton, J., 2016. The life cycle of phagosomes: formation, maturation, and resolution. Immunol. Rev. 273, 156–179. https://doi.org/10.1111/imr.12439
Ley, K., Laudanna, C., Cybulsky, M.I., Nourshargh, S., 2007. Getting to the site of inflammation: the leukocyte adhesion cascade updated. Nat. Rev. Immunol. 7, 678–689. https://doi.org/10.1038/nri2156
Li, D., Wu, M., 2021. Pattern recognition receptors in health and diseases. Signal Transduct. Target. Ther. 6, 291. https://doi.org/10.1038/s41392-021-00687-0
Li, H., Cybulsky, M.I., Gimbrone, M.A., Libby, P., 1993. An atherogenic diet rapidly induces VCAM-1, a cytokine-regulatable mononuclear leukocyte adhesion molecule, in rabbit aortic endothelium. Arterioscler. Thromb. J. Vasc. Biol. 13, 197–204. https://doi.org/10.1161/01.atv.13.2.197
Liao, S.-T., Han, C., Xu, D.-Q., Fu, X.-W., Wang, J.-S., Kong, L.-Y., 2019. 4-Octyl itaconate inhibits aerobic glycolysis by targeting GAPDH to exert anti-inflammatory effects. Nat. Commun. 10, 5091. https://doi.org/10.1038/s41467-019-13078-5
Libby, P., 2012. Inflammation in atherosclerosis. Arterioscler. Thromb. Vasc. Biol. 32, 2045–2051. https://doi.org/10.1161/ATVBAHA.108.179705
Libby, P., 2002. Inflammation in atherosclerosis. Nature 420, 868–874. https://doi.org/10.1038/nature01323
Libby, P., Ridker, P.M., Maseri, A., 2002. Inflammation and atherosclerosis. Circulation 105, 1135–1143. https://doi.org/10.1161/hc0902.104353
Liuba, P., Karnani, P., Pesonen, E., Paakkari, I., Forslid, A., Johansson, L., Persson, K., Wadström, T., Laurini, R., 2000. Endothelial dysfunction after repeated Chlamydia pneumoniae infection in apolipoprotein E-knockout mice. Circulation 102, 1039–1044. https://doi.org/10.1161/01.cir.102.9.1039
Luckheeram, R.V., Zhou, R., Verma, A.D., Xia, B., 2012. $CD4^+$T cells: differentiation and functions. Clin. Dev. Immunol. 2012, 925135. https://doi.org/10.1155/2012/925135

Ma, Y., Wang, W., Zhang, J., Lu, Y., Wu, W., Yan, H., Wang, Y., 2012. Hyperlipidemia and atherosclerotic lesion development in Ldlr-deficient mice on a long-term high-fat diet. PloS One 7, e35835. https://doi.org/10.1371/journal.pone.0035835

Mahley, R.W., Rall, S.C., 2000. Apolipoprotein E: far more than a lipid transport protein. Annu. Rev. Genomics Hum. Genet. 1, 507–537. https://doi.org/10.1146/annurev.genom.1.1.507

Mansukhani, N.A., Wang, Z., Shively, V.P., Kelly, M.E., Vercammen, J.M., Kibbe, M.R., 2017. Sex Differences in the LDL Receptor Knockout Mouse Model of Atherosclerosis. Artery Res. 20, 8–11. https://doi.org/10.1016/j.artres.2017.08.002

Mao, Y., Shi, D., Li, G., Jiang, P., 2022. Citrulline depletion by ASS1 is required for proinflammatory macrophage activation and immune responses. Mol. Cell 82, 527-541.e7. https://doi.org/10.1016/j.molcel.2021.12.006

McGeachy, M.J., Cua, D.J., Gaffen, S.L., 2019. The IL-17 Family of Cytokines in Health and Disease. Immunity 50, 892–906. https://doi.org/10.1016/j.immuni.2019.03.021

McKee, C.M., Coll, R.C., 2020. NLRP3 inflammasome priming: A riddle wrapped in a mystery inside an enigma. J. Leukoc. Biol. 108, 937–952. https://doi.org/10.1002/JLB.3MR0720-513R

Mehu, M., Narasimhulu, C.A., Singla, D.K., 2022. Inflammatory Cells in Atherosclerosis. Antioxid. Basel Switz. 11, 233. https://doi.org/10.3390/antiox11020233

Meir, K.S., Leitersdorf, E., 2004. Atherosclerosis in the apolipoprotein-E-deficient mouse: a decade of progress. Arterioscler. Thromb. Vasc. Biol. 24, 1006–1014. https://doi.org/10.1161/01.ATV.0000128849.12617.f4

Méndez-Barbero, N., Gutiérrez-Muñoz, C., Blanco-Colio, L.M., 2021. Cellular Crosstalk between Endothelial and Smooth Muscle Cells in Vascular Wall Remodeling. Int. J. Mol. Sci. 22, 7284. https://doi.org/10.3390/ijms22147284

Michelucci, A., Cordes, T., Ghelfi, J., Pailot, A., Reiling, N., Goldmann, O., Binz, T., Wegner, A., Tallam, A., Rausell, A., Buttini, M., Linster, C.L., Medina, E., Balling, R., Hiller, K., 2013. Immune-responsive gene 1 protein links metabolism to immunity by catalyzing itaconic acid production. Proc. Natl. Acad. Sci. U. S. A. 110, 7820–7825. https://doi.org/10.1073/pnas.1218599110

Mills, C.D., Kincaid, K., Alt, J.M., Heilman, M.J., Hill, A.M., 2000. M-1/M-2 macrophages and the Th1/Th2 paradigm. J. Immunol. Baltim. Md 1950 164, 6166–6173. https://doi.org/10.4049/jimmunol.164.12.6166

Mills, E.L., Kelly, B., Logan, A., Costa, A.S.H., Varma, M., Bryant, C.E., Tourlomousis, P., Däbritz, J.H.M., Gottlieb, E., Latorre, I., Corr, S.C., McManus, G., Ryan, D., Jacobs, H.T., Szibor, M., Xavier, R.J., Braun, T., Frezza, C., Murphy, M.P., O'Neill, L.A., 2016. Succinate Dehydrogenase Supports Metabolic Repurposing of Mitochondria to Drive Inflammatory Macrophages. Cell 167, 457-470.e13. https://doi.org/10.1016/j.cell.2016.08.064

Mills, E.L., Ryan, D.G., Prag, H.A., Dikovskaya, D., Menon, D., Zaslona, Z., Jedrychowski, M.P., Costa, A.S.H., Higgins, M., Hams, E., Szpyt, J., Runtsch, M.C., King, M.S., McGouran, J.F., Fischer, R., Kessler, B.M., McGettrick, A.F., Hughes, M.M., Carroll, R.G., Booty, L.M., Knatko, E.V., Meakin, P.J., Ashford, M.L.J., Modis, L.K., Brunori, G., Sévin, D.C., Fallon, P.G., Caldwell, S.T., Kunji, E.R.S., Chouchani, E.T., Frezza, C., Dinkova-Kostova, A.T., Hartley, R.C., Murphy, M.P., O'Neill, L.A., 2018. Itaconate is an anti-inflammatory metabolite that activates Nrf2 via alkylation of KEAP1. Nature 556, 113–117. https://doi.org/10.1038/nature25986

Mittendorfer, B., 2005. Sexual dimorphism in human lipid metabolism. J. Nutr. 135, 681–686. https://doi.org/10.1093/jn/135.4.681

Molteni, M., Gemma, S., Rossetti, C., 2016. The Role of Toll-Like Receptor 4 in Infectious and Noninfectious Inflammation. Mediators Inflamm. 2016, 6978936. https://doi.org/10.1155/2016/6978936

Moore, K.J., Freeman, M.W., 2006. Scavenger receptors in atherosclerosis: beyond lipid uptake. Arterioscler. Thromb. Vasc. Biol. 26, 1702–1711. https://doi.org/10.1161/01.ATV.0000229218.97976.43

Moore, K.J., Sheedy, F.J., Fisher, E.A., 2013. Macrophages in atherosclerosis: a dynamic balance. Nat. Rev. Immunol. 13, 709–721. https://doi.org/10.1038/nri3520
Motta, V., Soares, F., Sun, T., Philpott, D.J., 2015. NOD-like receptors: versatile cytosolic sentinels. Physiol. Rev. 95, 149–178. https://doi.org/10.1152/physrev.00009.2014
Mullen, A.R., Wheaton, W.W., Jin, E.S., Chen, P.-H., Sullivan, L.B., Cheng, T., Yang, Y., Linehan, W.M., Chandel, N.S., DeBerardinis, R.J., 2011. Reductive carboxylation supports growth in tumour cells with defective mitochondria. Nature 481, 385–388. https://doi.org/10.1038/nature10642
Murphy, K., Weaver, C., 2017. Janeway's Immunobiology 9th Edition, Garland Science. ed.
Nakashima, Y., Plump, A.S., Raines, E.W., Breslow, J.L., Ross, R., 1994. ApoE-deficient mice develop lesions of all phases of atherosclerosis throughout the arterial tree. Arterioscler. Thromb. J. Vasc. Biol. 14, 133–140. https://doi.org/10.1161/01.atv.14.1.133
Nakashima, Y., Raines, E.W., Plump, A.S., Breslow, J.L., Ross, R., 1998. Upregulation of VCAM-1 and ICAM-1 at atherosclerosis-prone sites on the endothelium in the ApoE-deficient mouse. Arterioscler. Thromb. Vasc. Biol. 18, 842–851. https://doi.org/10.1161/01.atv.18.5.842
Nelson, D.L., Cox, M.M., Hoskins, A.A., 2021. Lehninger Principles of Biochemistry, 8th Edition. W.H. Freeman Macmillan Learning.
Ohashi, R., Mu, H., Wang, X., Yao, Q., Chen, C., 2005. Reverse cholesterol transport and cholesterol efflux in atherosclerosis. QJM Mon. J. Assoc. Physicians 98, 845–856. https://doi.org/10.1093/qjmed/hci136
Pahwa, R., Goyal, A., Jialal, I., 2023. Chronic Inflammation, in: StatPearls. StatPearls Publishing, Treasure Island (FL).
Palmieri, E.M., Gonzalez-Cotto, M., Baseler, W.A., Davies, L.C., Ghesquière, B., Maio, N., Rice, C.M., Rouault, T.A., Cassel, T., Higashi, R.M., Lane, A.N., Fan, T.W.-M., Wink, D.A., McVicar, D.W., 2020. Nitric oxide orchestrates metabolic rewiring in M1 macrophages by targeting aconitase 2 and pyruvate dehydrogenase. Nat. Commun. 11, 698. https://doi.org/10.1038/s41467-020-14433-7
Palmisano, B.T., Zhu, L., Eckel, R.H., Stafford, J.M., 2018. Sex differences in lipid and lipoprotein metabolism. Mol. Metab. 15, 45–55. https://doi.org/10.1016/j.molmet.2018.05.008
Pan, H., Guo, Zhongzhou, Lv, P., Hu, K., Wu, T., Lin, Z., Xue, Y., Zhang, Y., Guo, Zhigang, 2023. Proline/serine-rich coiled-coil protein 1 inhibits macrophage inflammation and delays atherosclerotic progression by binding to Annexin A2. Clin. Transl. Med. 13, e1220. https://doi.org/10.1002/ctm2.1220
Papadakos, S.P., Arvanitakis, K., Stergiou, I.E., Lekakis, V., Davakis, S., Christodoulou, M.-I., Germanidis, G., Theocharis, S., 2023. The Role of TLR4 in the Immunotherapy of Hepatocellular Carcinoma: Can We Teach an Old Dog New Tricks? Cancers 15, 2795. https://doi.org/10.3390/cancers15102795
Piedrahita, J.A., Zhang, S.H., Hagaman, J.R., Oliver, P.M., Maeda, N., 1992. Generation of mice carrying a mutant apolipoprotein E gene inactivated by gene targeting in embryonic stem cells. Proc. Natl. Acad. Sci. U. S. A. 89, 4471–4475. https://doi.org/10.1073/pnas.89.10.4471
Pietzke, M., Vazquez, A., 2020. Metabolite AutoPlotter - an application to process and visualise metabolite data in the web browser. Cancer Metab. 8, 15. https://doi.org/10.1186/s40170-020-00220-x
Plüddemann, A., Neyen, C., Gordon, S., 2007. Macrophage scavenger receptors and host-derived ligands. Methods San Diego Calif 43, 207–217. https://doi.org/10.1016/j.ymeth.2007.06.004
Plump, A.S., Smith, J.D., Hayek, T., Aalto-Setälä, K., Walsh, A., Verstuyft, J.G., Rubin, E.M., Breslow, J.L., 1992. Severe hypercholesterolemia and atherosclerosis in apolipoprotein E-deficient mice created by homologous recombination in ES cells. Cell 71, 343–353. https://doi.org/10.1016/0092-8674(92)90362-g

Plytycz, B., Seljelid, R., 2003. From inflammation to sickness: historical perspective. Arch. Immunol. Ther. Exp. (Warsz.) 51, 105–109.
Qin, Y., O Santos, H., Khani, V., Tan, S.C., Zhi, Y., 2020. Effects of dehydroepiandrosterone (DHEA) supplementation on the lipid profile: A systematic review and dose-response meta-analysis of randomized controlled trials. Nutr. Metab. Cardiovasc. Dis. NMCD 30, 1465–1475. https://doi.org/10.1016/j.numecd.2020.05.015
Qualls, J.E., Subramanian, C., Rafi, W., Smith, A.M., Balouzian, L., DeFreitas, A.A., Shirey, K.A., Reutterer, B., Kernbauer, E., Stockinger, S., Decker, T., Miyairi, I., Vogel, S.N., Salgame, P., Rock, C.O., Murray, P.J., 2012. Sustained generation of nitric oxide and control of mycobacterial infection requires argininosuccinate synthase 1. Cell Host Microbe 12, 313–323. https://doi.org/10.1016/j.chom.2012.07.012
Raphael, I., Nalawade, S., Eagar, T.N., Forsthuber, T.G., 2015. T cell subsets and their signature cytokines in autoimmune and inflammatory diseases. Cytokine 74, 5–17. https://doi.org/10.1016/j.cyto.2014.09.011
Rekhter, M.D., 1999. Collagen synthesis in atherosclerosis: too much and not enough. Cardiovasc. Res. 41, 376–384. https://doi.org/10.1016/s0008-6363(98)00321-6
Rennick, J.J., Johnston, A.P.R., Parton, R.G., 2021. Key principles and methods for studying the endocytosis of biological and nanoparticle therapeutics. Nat. Nanotechnol. 16, 266–276. https://doi.org/10.1038/s41565-021-00858-8
Ripoll, V.M., Meadows, N.A., Bangert, M., Lee, A.W., Kadioglu, A., Cox, R.D., 2012. Nicotinamide nucleotide transhydrogenase (NNT) acts as a novel modulator of macrophage inflammatory responses. FASEB J. Off. Publ. Fed. Am. Soc. Exp. Biol. 26, 3550–3562. https://doi.org/10.1096/fj.11-199935
Roberts, L.M., Leighton, I., Schwarz, B., Wehrly, T.D., Evans, T.J., Bosio, C.M., 2022. Itaconate indirectly influences expansion of effector T cells following vaccination with Francisella tularensis live vaccine strain. Cell. Immunol. 373, 104485. https://doi.org/10.1016/j.cellimm.2022.104485
Roche, P.A., Furuta, K., 2015. The ins and outs of MHC class II-mediated antigen processing and presentation. Nat. Rev. Immunol. 15, 203–216. https://doi.org/10.1038/nri3818
Rokitansky, K., Swaine, W.E., Moore, C.H., Sieveking, E.H. (Edward H., Day, G.E., 1855. A manual of pathological anatomy. Philadelphia, Blanchard & Lea, 1855.
Roshan, M.H.K., Tambo, A., Pace, N.P., 2016. The Role of TLR2, TLR4, and TLR9 in the Pathogenesis of Atherosclerosis. Int. J. Inflamm. 2016, 1532832. https://doi.org/10.1155/2016/1532832
Ross, R., Glomset, J., Harker, L., 1977. Response to injury and atherogenesis. Am. J. Pathol. 86, 675–684.
Saigusa, R., Winkels, H., Ley, K., 2020. T cell subsets and functions in atherosclerosis. Nat. Rev. Cardiol. https://doi.org/10.1038/s41569-020-0352-5
Schile, A.J., 2016. Jaxpheno10: Atherosclerotic plaques and lipid profiles in non-fasting B6.129P2-Apoetm1Unc/J and B6.129S7-Ldlrtm1Her/J knockout mice (2016) [WWW Document]. URL https://phenome.jax.org/projects/Jaxpheno10 (accessed 9.25.23).
Schofield, J.H., Longo, J., Sheldon, R.D., Albano, E., Hawk, M.A., Murphy, S., Duong, L., Rahmy, S., Lu, X., Jones, R.G., Schafer, Z.T., 2023. Acod1 Expression in Cancer Cells Promotes Immune Evasion through the Generation of Inhibitory Peptides. https://doi.org/10.1101/2023.09.14.557799
Schrijvers, D.M., De Meyer, G.R.Y., Herman, A.G., Martinet, W., 2007. Phagocytosis in atherosclerosis: Molecular mechanisms and implications for plaque progression and stability. Cardiovasc. Res. 73, 470–480. https://doi.org/10.1016/j.cardiores.2006.09.005
Schroder, K., Hertzog, P.J., Ravasi, T., Hume, D.A., 2004. Interferon-gamma: an overview of signals, mechanisms and functions. J. Leukoc. Biol. 75, 163–189. https://doi.org/10.1189/jlb.0603252

Scolaro, B., Brown, E.J., Krautter, F., Petitjean, M., Donahoe, C., Pena, S., Garabedian, M.L., Nikain, C.A., Laskou, M., Tufanli, O., Hannemann, C., Aouadi, M., Weinstock, A., Fisher, E.A., 2023. Short-Term Caloric Restriction in Mice Promotes Resolution of Atherosclerosis, While Weight Regain Accelerates Its Progression. https://doi.org/10.1101/2023.05.07.539777

Seim, G.L., Britt, E.C., John, S.V., Yeo, F.J., Johnson, A.R., Eisenstein, R.S., Pagliarini, D.J., Fan, J., 2019. Two-stage metabolic remodelling in macrophages in response to lipopolysaccharide and interferon-γ stimulation. Nat. Metab. 1, 731–742. https://doi.org/10.1038/s42255-019-0083-2

Shah, P.K., 2001. Link between infection and atherosclerosis: who are the culprits: viruses, bacteria, both, or neither? Circulation 103, 5–6. https://doi.org/10.1161/01.cir.103.1.5

Simões, F.C., Cahill, T.J., Kenyon, A., Gavriouchkina, D., Vieira, J.M., Sun, X., Pezzolla, D., Ravaud, C., Masmanian, E., Weinberger, M., Mayes, S., Lemieux, M.E., Barnette, D.N., Gunadasa-Rohling, M., Williams, R.M., Greaves, D.R., Trinh, L.A., Fraser, S.E., Dallas, S.L., Choudhury, R.P., Sauka-Spengler, T., Riley, P.R., 2020. Macrophages directly contribute collagen to scar formation during zebrafish heart regeneration and mouse heart repair. Nat. Commun. 11, 600. https://doi.org/10.1038/s41467-019-14263-2

Srinivasan, M., Irving, B.A., Frye, R.L., O'Brien, P., Hartman, S.J., McConnell, J.P., Nair, K.S., 2010. Effects on lipoprotein particles of long-term dehydroepiandrosterone in elderly men and women and testosterone in elderly men. J. Clin. Endocrinol. Metab. 95, 1617–1625. https://doi.org/10.1210/jc.2009-2000

Stary, H.C., 2000. Natural history and histological classification of atherosclerotic lesions: an update. Arterioscler. Thromb. Vasc. Biol. 20, 1177–1178. https://doi.org/10.1161/01.atv.20.5.1177

Stary, H.C., Chandler, A.B., Dinsmore, R.E., Fuster, V., Glagov, S., Insull, W., Rosenfeld, M.E., Schwartz, C.J., Wagner, W.D., Wissler, R.W., 1995. A definition of advanced types of atherosclerotic lesions and a histological classification of atherosclerosis. A report from the Committee on Vascular Lesions of the Council on Arteriosclerosis, American Heart Association. Circulation 92, 1355–1374. https://doi.org/10.1161/01.cir.92.5.1355

Stary, H.C., Chandler, A.B., Glagov, S., Guyton, J.R., Insull, W., Rosenfeld, M.E., Schaffer, S.A., Schwartz, C.J., Wagner, W.D., Wissler, R.W., 1994. A definition of initial, fatty streak, and intermediate lesions of atherosclerosis. A report from the Committee on Vascular Lesions of the Council on Arteriosclerosis, American Heart Association. Arterioscler. Thromb. J. Vasc. Biol. 14, 840–856. https://doi.org/10.1161/01.atv.14.5.840

Stehbens, W.E., 1992. The role of thrombosis and variants of the thrombogenic theory in the etiology and pathogenesis of atherosclerosis. Prog. Cardiovasc. Dis. 34, 325–346. https://doi.org/10.1016/0033-0620(92)90038-2

Stein, M., Keshav, S., Harris, N., Gordon, S., 1992. Interleukin 4 potently enhances murine macrophage mannose receptor activity: a marker of alternative immunologic macrophage activation. J. Exp. Med. 176, 287–292. https://doi.org/10.1084/jem.176.1.287

Steinberg, D., 2013. In celebration of the 100th anniversary of the lipid hypothesis of atherosclerosis. J. Lipid Res. 54, 2946–2949. https://doi.org/10.1194/jlr.R043414

Steinberg, D., 2009. The LDL modification hypothesis of atherogenesis: an update. J. Lipid Res. 50 Suppl, S376-381. https://doi.org/10.1194/jlr.R800087-JLR200

Steinberg, D., Parthasarathy, S., Carew, T.E., Khoo, J.C., Witztum, J.L., 1989. Beyond cholesterol. Modifications of low-density lipoprotein that increase its atherogenicity. N. Engl. J. Med. 320, 915–924. https://doi.org/10.1056/NEJM198904063201407

Steinbrecher, U.P., Parthasarathy, S., Leake, D.S., Witztum, J.L., Steinberg, D., 1984. Modification of low density lipoprotein by endothelial cells involves lipid peroxidation

and degradation of low density lipoprotein phospholipids. Proc. Natl. Acad. Sci. U. S. A. 81, 3883–3887. https://doi.org/10.1073/pnas.81.12.3883
Strelko, C.L., Lu, W., Dufort, F.J., Seyfried, T.N., Chiles, T.C., Rabinowitz, J.D., Roberts, M.F., 2011. Itaconic acid is a mammalian metabolite induced during macrophage activation. J. Am. Chem. Soc. 133, 16386–16389. https://doi.org/10.1021/ja2070889
Sun, H.-J., Wu, Z.-Y., Nie, X.-W., Bian, J.-S., 2019. Role of Endothelial Dysfunction in Cardiovascular Diseases: The Link Between Inflammation and Hydrogen Sulfide. Front. Pharmacol. 10, 1568. https://doi.org/10.3389/fphar.2019.01568
Swain, A., Bambouskova, M., Kim, H., Andhey, P.S., Duncan, D., Auclair, K., Chubukov, V., Simons, D.M., Roddy, T.P., Stewart, K.M., Artyomov, M.N., 2020. Comparative evaluation of itaconate and its derivatives reveals divergent inflammasome and type I interferon regulation in macrophages. Nat. Metab. https://doi.org/10.1038/s42255-020-0210-0
Takeshita, S., Kaji, K., Kudo, A., 2000. Identification and characterization of the new osteoclast progenitor with macrophage phenotypes being able to differentiate into mature osteoclasts. J. Bone Miner. Res. Off. J. Am. Soc. Bone Miner. Res. 15, 1477–1488. https://doi.org/10.1359/jbmr.2000.15.8.1477
Tanaka, K., Sata, M., 2013. Blockade of cytidine triphosphate synthase regulates smooth muscle cell and endothelial cell proliferation differentially. Arterioscler. Thromb. Vasc. Biol. 33, 2286–2287. https://doi.org/10.1161/ATVBAHA.113.302315
Tardif, J.-C., Kouz, S., Waters, D.D., Bertrand, O.F., Diaz, R., Maggioni, A.P., Pinto, F.J., Ibrahim, R., Gamra, H., Kiwan, G.S., Berry, C., López-Sendón, J., Ostadal, P., Koenig, W., Angoulvant, D., Grégoire, J.C., Lavoie, M.-A., Dubé, M.-P., Rhainds, D., Provencher, M., Blondeau, L., Orfanos, A., L'Allier, P.L., Guertin, M.-C., Roubille, F., 2019. Efficacy and Safety of Low-Dose Colchicine after Myocardial Infarction. N. Engl. J. Med. 381, 2497–2505. https://doi.org/10.1056/NEJMoa1912388
Tauber, A.I., 2003. Metchnikoff and the phagocytosis theory. Nat. Rev. Mol. Cell Biol. 4, 897–901. https://doi.org/10.1038/nrm1244
Teupser, D., Persky, A.D., Breslow, J.L., 2003. Induction of atherosclerosis by low-fat, semisynthetic diets in LDL receptor-deficient C57BL/6J and FVB/NJ mice: comparison of lesions of the aortic root, brachiocephalic artery, and whole aorta (en face measurement). Arterioscler. Thromb. Vasc. Biol. 23, 1907–1913. https://doi.org/10.1161/01.ATV.0000090126.34881.B1
Theofilis, P., Oikonomou, E., Vogiatzi, G., Sagris, M., Antonopoulos, A.S., Siasos, G., Iliopoulos, D.C., Perrea, D., Vavouranakis, M., Tsioufis, K., Tousoulis, D., 2023. The Role of MicroRNA-126 in Atherosclerotic Cardiovascular Diseases. Curr. Med. Chem. 30, 1902–1921. https://doi.org/10.2174/0929867329666220830100530
Thirumalai, A., Rubinow, K.B., Page, S.T., 2015. An update on testosterone, HDL and cardiovascular risk in men. Clin. Lipidol. 10, 251–258. https://doi.org/10.2217/clp.15.10
Tian, K., Ogura, S., Little, P.J., Xu, S.-W., Sawamura, T., 2019. Targeting LOX-1 in atherosclerosis and vasculopathy: current knowledge and future perspectives. Ann. N. Y. Acad. Sci. 1443, 34–53. https://doi.org/10.1111/nyas.13984
Ting, J.P.-Y., Lovering, R.C., Alnemri, E.S., Bertin, J., Boss, J.M., Davis, B.K., Flavell, R.A., Girardin, S.E., Godzik, A., Harton, J.A., Hoffman, H.M., Hugot, J.-P., Inohara, N., Mackenzie, A., Maltais, L.J., Nunez, G., Ogura, Y., Otten, L.A., Philpott, D., Reed, J.C., Reith, W., Schreiber, S., Steimle, V., Ward, P.A., 2008. The NLR gene family: a standard nomenclature. Immunity 28, 285–287. https://doi.org/10.1016/j.immuni.2008.02.005
Tousoulis, D., Oikonomou, E., Economou, E.K., Crea, F., Kaski, J.C., 2016. Inflammatory cytokines in atherosclerosis: current therapeutic approaches. Eur. Heart J. 37, 1723–1732. https://doi.org/10.1093/eurheartj/ehv759
Ullah, M.O., Sweet, M.J., Mansell, A., Kellie, S., Kobe, B., 2016. TRIF-dependent TLR signaling, its functions in host defense and inflammation, and its potential as a

therapeutic target. J. Leukoc. Biol. 100, 27–45. https://doi.org/10.1189/jlb.2RI1115-531R
Uribe-Querol, E., Rosales, C., 2020. Phagocytosis: Our Current Understanding of a Universal Biological Process. Front. Immunol. 11, 1066. https://doi.org/10.3389/fimmu.2020.01066
Vance, J.E., 2015. Phospholipid synthesis and transport in mammalian cells. Traffic Cph. Den. 16, 1–18. https://doi.org/10.1111/tra.12230
Voloshyna, I., Littlefield, M.J., Reiss, A.B., 2014. Atherosclerosis and interferon-γ: new insights and therapeutic targets. Trends Cardiovasc. Med. 24, 45–51. https://doi.org/10.1016/j.tcm.2013.06.003
Weis, W.I., Taylor, M.E., Drickamer, K., 1998. The C-type lectin superfamily in the immune system. Immunol. Rev. 163, 19–34. https://doi.org/10.1111/j.1600-065x.1998.tb01185.x
Weiss, J.M., Palmieri, E.M., Gonzalez-Cotto, M., Bettencourt, I.A., Megill, E.L., Snyder, N.W., McVicar, D.W., 2023. Itaconic acid underpins hepatocyte lipid metabolism in non-alcoholic fatty liver disease in male mice. Nat. Metab. 5, 981–995. https://doi.org/10.1038/s42255-023-00801-2
Wen, H., Gris, D., Lei, Y., Jha, S., Zhang, L., Huang, M.T.-H., Brickey, W.J., Ting, J.P.-Y., 2011. Fatty acid-induced NLRP3-ASC inflammasome activation interferes with insulin signaling. Nat. Immunol. 12, 408–415. https://doi.org/10.1038/ni.2022
Williams, C.M., 2004. Lipid metabolism in women. Proc. Nutr. Soc. 63, 153–160. https://doi.org/10.1079/PNS2003314
Wilson, B.A., Schisler, J.C., Willis, M.S., 2010. Sir Hans Adolf Krebs: Architect of Metabolic Cycles. Lab. Med. 41, 377–380. https://doi.org/10.1309/LMZ5ZLAC85GFMGHU
Yamagishi, Y., Someya, A., Nagaoka, I., 2020. Citrulline cooperatively exerts an anti-inflammatory effect on synovial cells with glucosamine and N-acetylglucosamine. Biomed. Rep. 13, 37–42. https://doi.org/10.3892/br.2020.1304
Yang, M., Qi, X., Li, N., Kaifi, J.T., Chen, S., Wheeler, A.A., Kimchi, E.T., Ericsson, A.C., Rector, R.S., Staveley-O'Carroll, K.F., Li, G., 2023. Western diet contributes to the pathogenesis of non-alcoholic steatohepatitis in male mice via remodeling gut microbiota and increasing production of 2-oleoylglycerol. Nat. Commun. 14, 228. https://doi.org/10.1038/s41467-023-35861-1
Yang, Y., Wang, H., Kouadir, M., Song, H., Shi, F., 2019. Recent advances in the mechanisms of NLRP3 inflammasome activation and its inhibitors. Cell Death Dis. 10, 128. https://doi.org/10.1038/s41419-019-1413-8
Yang, Z., Ming, X.-F., 2014. Functions of arginase isoforms in macrophage inflammatory responses: impact on cardiovascular diseases and metabolic disorders. Front. Immunol. 5, 533. https://doi.org/10.3389/fimmu.2014.00533
Yoshida, H., Kisugi, R., 2010. Mechanisms of LDL oxidation. Clin. Chim. Acta Int. J. Clin. Chem. 411, 1875–1882. https://doi.org/10.1016/j.cca.2010.08.038
Yu, L., Zhang, Yujie, Liu, C., Wu, X., Wang, S., Sui, W., Zhang, Yun, Zhang, C., Zhang, M., 2023. Heterogeneity of macrophages in atherosclerosis revealed by single-cell RNA sequencing. FASEB J. Off. Publ. Fed. Am. Soc. Exp. Biol. 37, e22810. https://doi.org/10.1096/fj.202201932RR
Zhao, H., Teng, D., Yang, L., Xu, X., Chen, J., Jiang, T., Feng, A.Y., Zhang, Y., Frederick, D.T., Gu, L., Cai, L., Asara, J.M., Pasca di Magliano, M., Boland, G.M., Flaherty, K.T., Swanson, K.D., Liu, D., Rabinowitz, J.D., Zheng, B., 2022. Myeloid-derived itaconate suppresses cytotoxic CD8+ T cells and promotes tumour growth. Nat. Metab. 4, 1660–1673. https://doi.org/10.1038/s42255-022-00676-9
Zhou, E., Li, Z., Nakashima, H., Liu, C., Ying, Z., Foks, A.C., Berbée, J.F.P., van Dijk, K.W., Rensen, P.C.N., Wang, Y., 2021. Hepatic Scavenger Receptor Class B Type 1 Knockdown Reduces Atherosclerosis and Enhances the Antiatherosclerotic Effect of Brown Fat Activation in APOE*3-Leiden.CETP Mice. Arterioscler. Thromb. Vasc. Biol. 41, 1474–1486. https://doi.org/10.1161/ATVBAHA.121.315882

9. SUPPLEMENTARY FIGURES

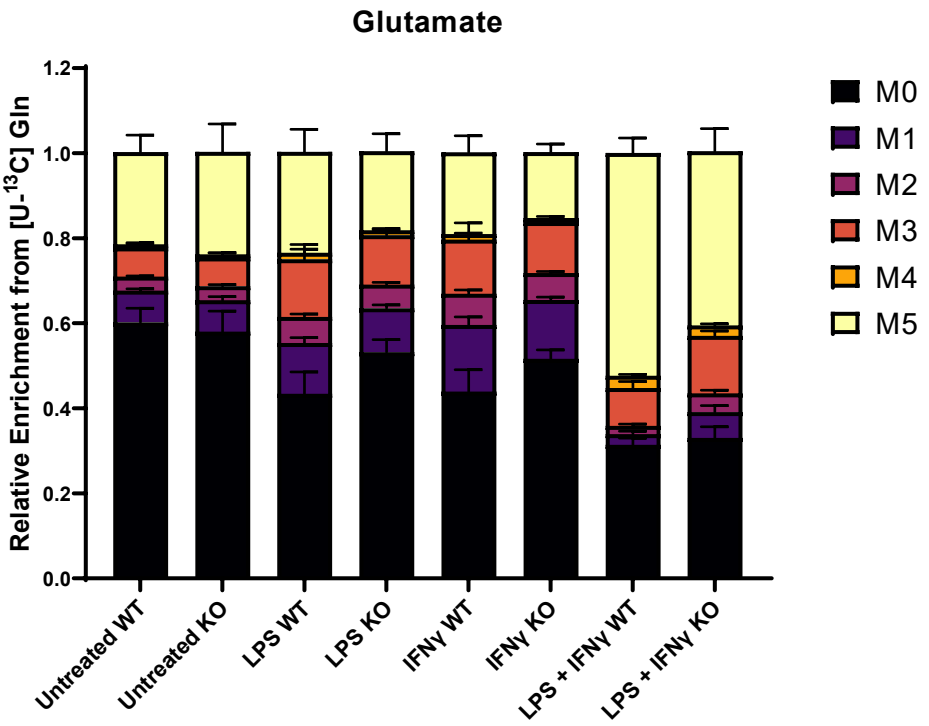

Supplementary Figure 1: Total relative enrichment of Glutamate from 13C Gln is unchanged in LPS-IFNγ stimulated BMDMs.

Relative enrichment of Glutamate from ^{13}C glutamine in LPS, IFNγ and double stimulated BMDMs of WT and KO mice. Each bar represents the mean of 2 independent experiments. The error bar represents the standard deviation. WT=11, KO=11.

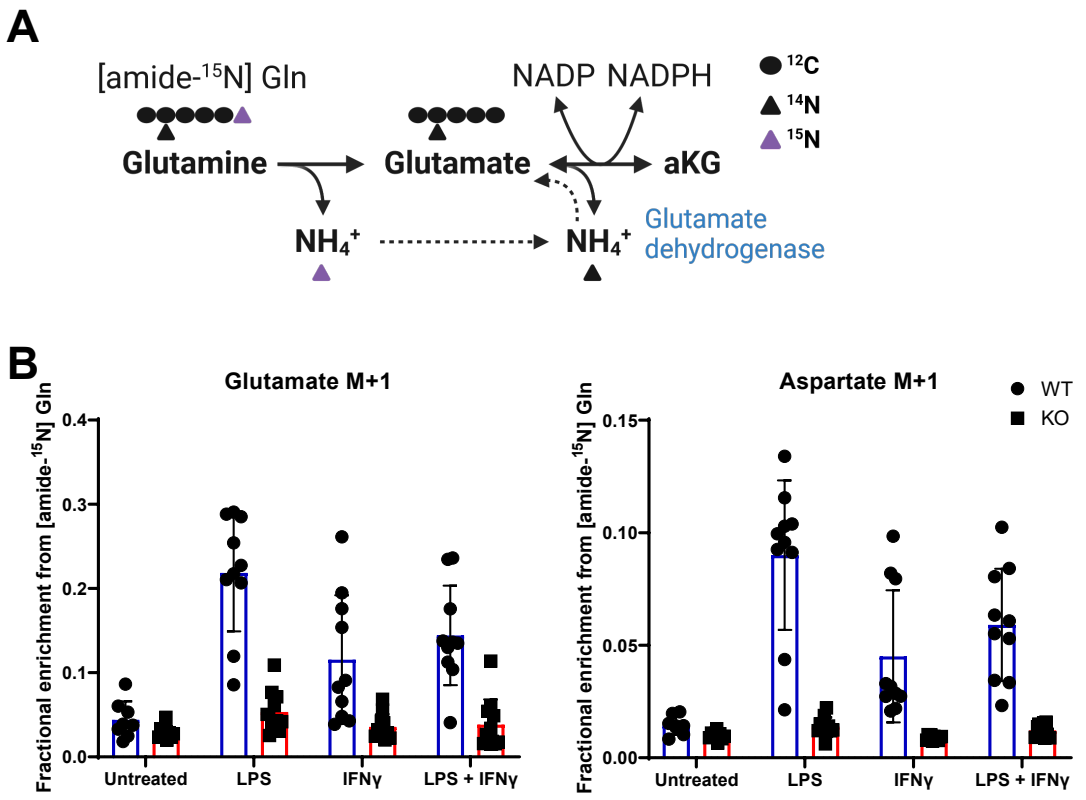

Supplementary Figure 2: Glutamate dehydrogenase catalyses the aKG to glutamate reaction in WT BMDMs.

A, Schematic representation of glutamate M+1 enrichment from amide-^{15}N glutamine. When converted into glutamate, glutamine releases the amide group resulting in glutamate and free ammonium. Glutamate dehydrogenase catalyses the aKG to glutamate reaction using an ammonium ion which can be labelled resulting in an alpha-^{15}N labelled glutamate molecule. **B,** Fractional enrichment of glutamate M+1 and aspartate M+1 from amide-^{15}N glutamine in LPS, IFNγ and double stimulated BMDMs of WT (blue) and KO (red) mice. WT=10, KO=11 from two independent experiments.

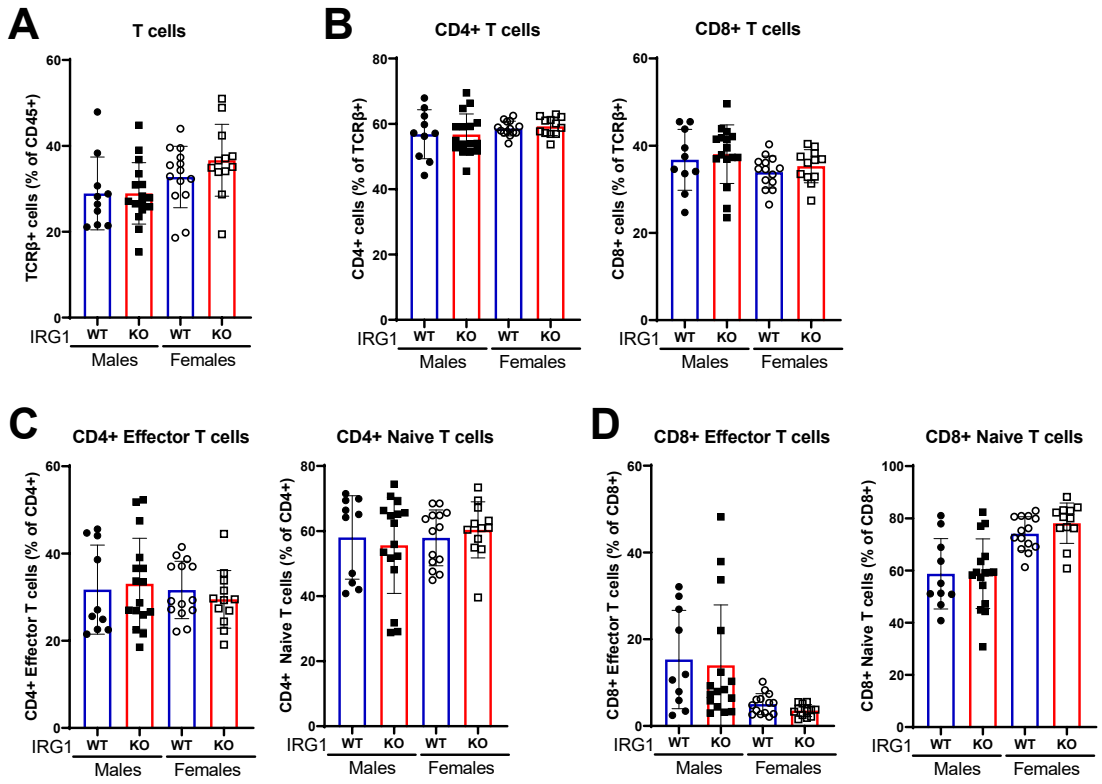

Supplementary Figure 3: IRG1 deficiency does not affect T cell populations in the spleen of LDLr KO mice.

A, Flow cytometry analysis of the frequency of splenic T cells of LDLr KO of male and female IRG1 WT (blue) and KO (red) mice fed for 12 weeks a HFD. **B,** Flow cytometry analysis of the frequency of CD4+ and CD8+ T cells within the total T cells population in the spleen of male and female IRG1 WT (blue) and KO (red) mice. **C,** Flow cytometry analysis of the frequency of CD4+ effector and naive T cells within the total T CD4+ cell population in the spleen of male and female IRG1 WT (blue) and KO (red) mice. **D,** Flow cytometry analysis of the frequency of CD8+ effector and naive T cells within the total T CD8+ cell population in the spleen of male and female IRG1 WT (blue) and KO (red) mice. **A-D**, Males WT n=10 KO n=15; Females WT n=13 KO n=12.

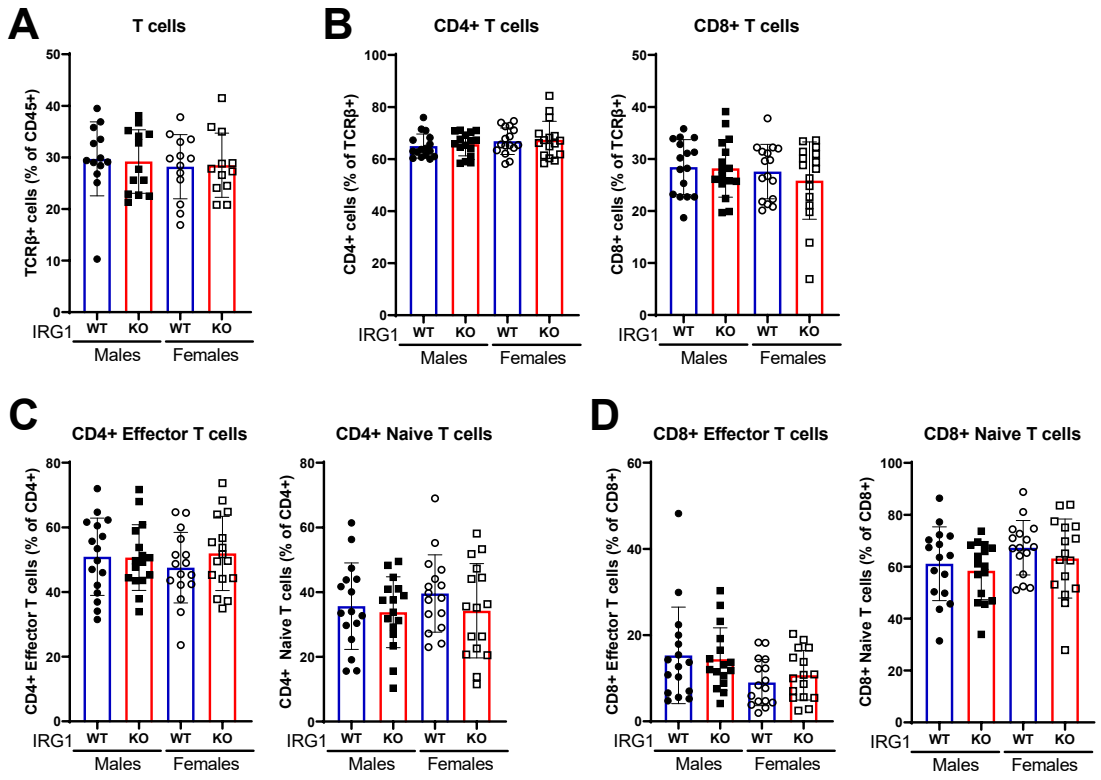

Supplementary Figure 4: IRG1 deficiency does not affect T cell populations in the spleen of ApoE KO mice.

A Flow cytometry analysis of the frequency of splenic T cells ApoE KO male and female IRG1 WT (blue) and KO (red) mice fed for 12 weeks a HFD. **B,** Flow cytometry analysis of the frequency of CD4+ and CD8+ T cells within the total T cells population in the spleen of male and female IRG1 WT (blue) and KO (red) mice. **C,** Flow cytometry analysis of the frequency of CD4+ effector and naive T cells within the total T CD4+ cell population in the spleen of male and female IRG1 WT (blue) and KO (red) mice. **D,** Flow cytometry analysis of the frequency of CD8+ effector and naive T cells within the total T CD8+ cell population in the spleen of male and female IRG1 WT (blue) and KO (red) mice. **A-D**, Males WT n=16 KO n=16; Females WT n=15 KO n=16.